UNIVERSIDADE FEDERAL DO RIO GRANDE DO SUL
INSTITUTO DE INFORMÁTICA
PROGRAMA DE PÓS-GRADUAÇÃO EM MICROELETRÔNICA

PEDRO FILIPE LEITE CORREIA DE TOLEDO

Digital-Based Analog Processing in Nanoscale CMOS ICs for IoT Applications

Thesis presented in partial fulfillment
of the requirements for the degree of
Doctor of Microeletronics

Advisor: Prof. Dr. Hamilton Duarte Klimach
Coadvisor: Prof. Dr. Paolo Stefano Crovetti

Porto Alegre
September 2022

CIP — CATALOGING-IN-PUBLICATION

Leite Correia de Toledo, Pedro Filipe

Digital-Based Analog Processing in Nanoscale CMOS ICs for IoT Applications / Pedro Filipe Leite Correia de Toledo. – Porto Alegre: PGMICRO da UFRGS, 2022.

124 f.: il.

Thesis (Ph.D.) – Universidade Federal do Rio Grande do Sul. Programa de Pós-Graduação em Microeletrônica, Porto Alegre, BR–RS, 2022. Advisor: Hamilton Duarte Klimach; Coadvisor: Paolo Stefano Crovetti.

1. CMOS. 2. VLSI. 3. Ultra Low Power. 4. Ultra Low Voltage. 5. Internet of Things. 6. IoT. 7. Digital-Based OTA. 8. Digital OTA. 9. DigOTA. 10. Operational Transconductance Amplifier. I. Klimach, Hamilton Duarte. II. Crovetti, Paolo Stefano. III. Título.

“I am not here to take part,
I am here to take over.”
— CONOR MCGREGOR

ACKNOWLEDGEMENTS

I would like especially to acknowledge my wife, **Claudia Camerini Correa da Silva de Toledo** for all the motivation, support, and patience during my whole Ph.D. studies. She mainly had to take care of our kids alone during pandemic times while I was measuring the chips related to this thesis. During these three years of my Ph.D., I lost my loving father-in-law, who I considered a father. I want to dedicate this thesis to his memory. Rest in peace, Dear Sr. Prof. **Claudio Osma Crochi da Silva**. Hugs and kisses to my sons, **Pietro** and **Filippo**, who contributed to keeping this work in hard mode.

I would like to thank my parents, **Bernardino Marques Toledo** and **Sineide Leite da Silva**, and my beautiful sisters **Thais Toledo** e **Adriana Toledo**, for all the financial support given to my Ph.D.'s studies and life in Turin.

Thanks to my advisors, Prof. **Paolo Crovetti** and Prof. **Hamilton Klimach** for the excellent discussions that helped me to mature and learn so much in the field of microelectronics. In detail, I would like to especially thank Prof. **Paolo Crovetti** who has believed, received, and supported me while I was in Turin, giving personal pieces of advice, besides the technical ones. The same remarks apply to Prof. **Sergio Bampi**, Dr. **Orazio Aiello** and Prof **Massimo Alioto**. My friends from lab in Italy, **Roberto Rubino**, **Chen** and **Osama Bin Tariq**. Special remarks to **Maksudjon Usmonov** for his valuable support during the measurements. My friends of old NSCAD group, Prof. Eric Fabris, Everton Ghignatti, Renê Timbo, Diogo Santana, German Fierro, Helga Dornelas, Alonso Schmidt, Jhon Caicedo, and David Cordova. My old friends of lab 110 Analog/RF group, Arthur Liraneto, Filipe Baumgratz, Renato Campana , Sandro Binsfeld, Oscar Mattia, Márlon Lorenzetti, Rafael Schultz, Luís Rodovalho, Bruno Canal, Moacir Monteiro, Arthur Oliveira, Roger Zamparette, Gabriel Guimarães, Fernando Carrion, Marcelo Pedrini, Thales Ribeiro and Yi Chen Wu for the discussions in the lab and meetings.

Thanks to all administrative people, who have been working hard to keep all the infrastructure available to me, from both institutes: Graduate Program in Microelectronics from the Federal University of Rio Grande do Sul - Brazil and Department of Electronics and Telecommunications from Politecnico di Torino - Italy. MOSIS for the MOSIS Educational Program (MEP) allowed fabricating one of the circuits presented here.

ABSTRACT

The Internet-of-Things (IoT) concept has been opening up a variety of applications, such as urban and environmental monitoring, smart health, surveillance, and home automation. Most of these IoT applications require more and more power/area efficient Complementary Metal–Oxide–Semiconductor (CMOS) systems and faster prototypes (lower time-to-market), demanding special modifications in the current IoT design system bottleneck: the analog/RF interfaces.

Specially after the 2000s, it is evident that there have been significant improvements in CMOS digital circuits when compared to analog building blocks. Digital circuits have been taking advantage of CMOS technology scaling in terms of speed, power consumption, and cost, while the techniques running behind the analog signal processing are still lagging. To decrease this historical gap, there has been an increasing trend in finding alternative IC design strategies to implement typical analog functions exploiting Digital-in-Concept Design Methodologies (DCDM). This idea of re-thinking analog functions in digital terms has shown that Analog ICs blocks can also avail of the feature-size shrinking and energy efficiency of new technologies.

This thesis deals with the development of DCDM, demonstrating its compatibility for Ultra-Low-Voltage (ULV) and Power (ULP) IoT applications. This work proves this statement through the proposing of new digital-based analog blocks, such as an Operational Transconductance Amplifiers (OTAs) and an ac-coupled Bio-signal Amplifier (BioAmp). As an initial contribution, for the first time, a silicon demonstration of an embryonic Digital-Based OTA (DB-OTA) published in 2013 is exhibited. The fabricated DB-OTA test chip occupies a compact area of 1,426 μm^2, operating at supply voltages (V_{DD}) down to 300 mV, consuming only 590 pW while driving a capacitive load of 80pF. With a Total Harmonic Distortion (THD) lower than 5% for a 100mV input signal swing, its measured small-signal figure of merit ($\mathrm{FOM_S}$) and large-signal figure of merit ($\mathrm{FOM_L}$) are 2,101 V^{-1} and 1,070, respectively. To the best of this thesis author's knowledge, this measured power is the lowest reported to date in OTA literature, and its figures of merit are the best in sub-500mV OTAs reported to date.

As the second step, mainly due to the robustness limitation of previous DB-OTA, a novel calibration-free digital-based topology is proposed, named here as Digital OTA (DIGOTA). A 180-nm DIGOTA test chip is also developed exhibiting an area below the 1000 μm^2 wall, 2.4nW power under 150pF load, and a minimum V_{DD} of 0.25 V. The proposed

DIGOTA is more digital-like compared with DB-OTA since no pseudo-resistor is needed. As the last contribution, the previously proposed DIGOTA is then used as a building block to demonstrate the operation principle of power-efficient ULV and ultra-low area (ULA) fully-differential, digital-based Operational Transconductance Amplifier (OTA), suitable for microscale biosensing applications (BioDIGOTA) such as extreme low area *Body Dust*. Measured results in 180nm CMOS confirm that the proposed BioDIGOTA can work with a supply voltage down to 400 mV, consuming only 95 nW. The BioDIGOTA layout occupies only 0.022 mm^2 of total silicon area, lowering the area by 3.22X times compared to the current state of the art while keeping reasonable system performance, such as 7.6 Noise Efficiency Factor (NEF) with 1.25 μV_{RMS} input-referred noise over a 10 Hz bandwidth, 1.8% of THD, 62 dB of the common-mode rejection ratio (CMRR) and 55 dB of power supply rejection ratio (PSRR).

After reviewing the current DCDM trend and all proposed silicon demonstrations, the thesis concludes that, despite the current analog design strategies involved during the analog block development has been indispensable to unfold several cutting edge applications over the last decades, the DCDM design strategy presented here seems to be very attractive for new technologies and continuing advance analog interface performance, especially for IoT applications. These circuits could take advantage of better awareness of the discrete nature of information and the steadily increasing timing resolution of more advanced CMOS nodes.

Keywords: CMOS. VLSI. Ultra Low Power. Ultra Low Voltage. Internet of Things. IoT. Digital-Based OTA. Digital OTA. DigOTA. Operational Transconductance Amplifier.

LIST OF ABBREVIATIONS AND ACRONYMS

IoT	Internet-of-Things
CMOS	Complementary Metal–Oxide–Semiconductor
VLSI	Very Large Scale Integration
RF	Radio Frequency
DCDM	Digital in-Concept Design Methodologies
ULV	Ultra-Low-Voltage
ULP	Ultra-Low-Power
OTAs	Operational Transconductance Amplifiers
BioAmp	Bio-signal Amplifier
DB-OTA	Digital-Based OTA
THD	Total Harmonic Distortion
FOM_S	Small-Signal Figure Of Merit
FOM_L	Large-signal Figure Of Merit
DIGOTA	Digital OTA
ULA	Ultra-Low-Area
NEF	Noise Efficiency Factor
CMRR	Common-Mode Rejection Ratio
PSRR	Power Supply Rejection Ratio
ICs	Integrated Circuits
FTP	File Transfer Protocol
ITU	International Telecommunication Union
IEEE	Institute of Electrical and Electronics Engineers
MCU	microprocessors
SOCs	System on Chip

FPGA	Field-Programmable Gate Array
SOA	Service-Oriented Architecture
TCP/IP	Transmission Control Protocol/Internet Protocol
NFC	Near Field Communication
IrDA	Infrared Data Association
UWB/IR	Ultra-Wideband
DASH7	Alliance Protocol
RPL	Routing Protocol for Low-Power and Lossy Networks
BTLE	Bluetooth
6LowPAN	IPv6 over Low-Power Wireless Personal Area Networks
EDA	Electronic Design Automation
PDK	Process Design Kit
PCB	Printed Circuit Board
ADC	Analog to Digital Converter
ENOB	Effective Number of Bits
SPIs	Serial Peripheral Interfaces
I2Cs	Inter-Integrated Circuits
USBs	Universal Serial Buses
UARTs	Universal Asynchronous Receiver-Transmitters
ISM	Industrial Scientific Medical Band
TSMC	Taiwan Semiconductor Manufacturing Company
IMF	International Monetary Fund
GDP	Gross Domestic Product
TFB	thin-film battery
DVS	Dynamic Voltage Scaling
DLS	Dynamic Leakage-Suppression

SDLC	Scalable Dynamic Leakage-Suppression
CMFB	Common Mode Feedback
CMFF	Common Mode Feed Forward
RSCE	Reverse-Short-Channel Effect
ALS	Automate Analog Layout Synthesis
CAS	Circuit and System
PLLs	Phase-Locked Loops
SARs	Successive Approximation Registers
VCO	Voltage Controlled Oscillator
DACs	Digital to Analog converters
LDOs	Low-Dropout Regulators
FO4	Fan-Out-of-4
CMIR	Common-Mode Input Range
CM	Common-Mode
DM	Differential-Mode
PM	phase margin
MEP	Minimum Energy Point
SDC	Static Digital Calibration
DDC	Dynamic Digital Calibration
DPWM	Digital Pulse Width Modulation
DDPM	Dyadic Digital Pulse Modulation
FFT	Fast Fourier Transform
MC	Montecarlo
GBW	Gain Bandwidth Product
UCCM	Unified Charge-Control Model
DIBL	Drain Induced Barrier Lowering

CS	Common-Source
ECG	Electrocardiogram
FD	Fully Differential
MiM	Metal-insulator-Metal
PSD	Power Spectral Density
CT	Composite Transistors
STA	Static Time Analysis

LIST OF FIGURES

LIST OF TABLES

CONTENTS

1 INTRODUCTION

The Internet of the Things (IoT) concept aims to turn everyday life objects into smart things by exploiting underlying technologies like ubiquitous and pervasive computing, embedded devices, communication technologies, sensor networks, internet protocols, and applications. The IoT enables physical objects to see, hear, feel, measure, think, and perform tasks by "talking" together, sharing information, and coordinating decisions. The emerging idea of IoT is rapidly finding its momentum throughout our modern life, aiming to increase our comfort and improve our quality of life.

The IoT architecture embracing all abstraction levels needs to be carefully conceived to make this concept reasonably viable. Challenges should be pointed out and addressed, including facts related to the cheapest technology that makes it possible: Complementary Metal Oxide Semiconductor (CMOS) technology. Devices made in CMOS are deployed on the edges of the IoT network gathering information from the physical world and sharing back to the cloud for more ambitious analytic capabilities.

Such edge devices, i.e., integrated circuits (ICs), comprise analog, mixed-signal, radio-frequency (RF), and digital processing capability (for instance, to get precise information from the sensors), and the definition of their architectures, technologies, and design methodologies play a fundamental role in the final performance of the whole system. Such aspects are intrinsically related to the last ICs area and power consumption, which in turn can be several times the IoT chain bottleneck. In other words, often, the edge device performance dictates the final decision to evaluate whether that application is viable or not.

In this introduction, the section 1.1 exposes the IoT concept principles as well as its applications, also showing their current market perspectives. In section 1.2, IoT network architectures are briefly reviewed, focusing on the CMOS edge devices description. Challenges found in such devices during their design are described in section 1.3, outlining the main current analog and digital techniques for power reduction. Based on several examples, the Digital-in-Concept Design Methodology (DCDM) trend is then introduced as an alternative design approach for the next generation of low power analog circuits within IoT nodes in section 1.4. The thesis organization is outlined in section 1.5, stressing how the following chapters are organized and the main thesis contributions.

1.1 IoT Concept and Applications

In 1999, Kevin Ashton, co-founder of the Auto-ID Laboratory at MIT, gave birth to the term Internet of Things (ZHANG et al., 2020); however, the general concept idea has been around for much longer. Back in the early 80s, at Carnegie Mellon University, a group of students designed a system to get their campus Coca-Cola vending machine to report on its contents. They could make the machines let them know whether newly loaded drinks were cold or not. Later, in 1990, John Romkey connected a toaster to the internet for the first time using File Transfer Protocol (FTP) (ROMKEY, 2017).

In the following years, worldwide organizations and research institutes started to become excited about the Internet of Things, and several definitions and visions were proposed and spread. The International Telecommunication Union (ITU) delineates IoT as a universal information infrastructure for the society, permitting advanced and sophisticated services by interconnecting objects based on existing and evolving communication technologies (UNION, 2012). Both the UK Government Office of Science and the European Commission share a similar outlook of the IoT: *a world in which everyday objects are connected to a network so that valuable data can be shared* (ADVISER, 2014; SIOW; TIROPANIS; HALL, 2018). Among all definitions found in the current literature, common characteristics of each of these visions can be narrowed into four well-clear principles:

- Global scale principle: the IoT exists at a global scale (LEE; HANCOCK; HU, 2014).
- Physical world interaction principle: it consists of uniquely identifiable things with sensing or actuating capabilities linked to the physical world (ATZORI; IERA; MORABITO, 2010).
- Interconnection principle: things are interconnected by existing or future technologies so that data can be shared (KORTUEM et al., 2010; YICK; MUKHERJEE; GHOSAL, 2008).
- Servicing principle: analytics derived from gathered data have potential for societal impact through advanced services (SIOW; TIROPANIS; HALL, 2018).

From the most cited paper about IoT in the Institute of Electrical and Electronics Engineers (IEEE) database (AL-FUQAHA et al., 2015), Fig.1.1 illustrates the global and comprehensive IoT concept in which every single domain-specific application is in-

Figure 1.1: *Vertical markets*: smart things with their supposed functions constitute domain specific applications. *Horizontal markets*: application domain independent services with ubiquitous computing and analytical services (AL-FUQAHA et al., 2015).

terfacing with domain-independent services, whereas in each domain sensors and actuators (IoT nodes or edge devices) broadcast relevant information directly with each other (AL-FUQAHA et al., 2015). Even though Fig. 1.1 summarizes reasonably well the IoT general concept through two abstraction levels/domains; this picture is far away from an authentic representation of the entire IoT network architecture, its challenges, and its real applicability potential. In the following section 1.2, the current state-of-the-art of the IoT architectures is shown, giving special attention to the challenges found on the hardware implementation of the edge devices.

The list of applications is extensive in enterprise settings, numbering more than two hundreds known applications, as reported by McKinsey (FREDRIK et al., 2019), from healthcare to monitoring chemical processes (MUKHERJEE; PAL; MISRA, 2012; CHEN et al., 2016; HOSSAIN; MUHAMMAD, 2016; BANOS et al., 2016; MAK; FAN,

2006; DANNER et al., 2016; JARA; GENOUD; BOCCHI, 2015; PADEN et al., 2016; HE; YAN; XU, 2014; PIOVESAN et al., 2016; CHIANESE et al., 2017; RAZIP et al., 2014; GIMENEZ et al., 2012; PLOENNIGS; SCHUMANN; LÉCUÉ, 2014; KOMNINOS; PHILIPPOU; PITSILLIDES, 2014; GUO; ZHANG; WANG, 2011; MUKHERJEE; CHATTERJEE, 2014; GHOSH; PATIL; VUPPALA, 2013; YAN et al., 2013; JIN et al., 2014; SCHNIZLER et al., 2014; MUKHERJEE et al., 2013; VARGHEESE; DAHIR, 2014; NECHIFOR et al., 2014; ROBAK; FRANCZYK; ROBAK, 2013; VERDOUW; BEULENS; van der Vorst, 2013; KAMILARIS et al., 2016; CHIANG; LU; CASTILLO, 2017). Regardless of its nature, all the above-cited applications needs in general to pursue six goals: *identification*, *sensing*, *communication*, *computation*, *services* and *semantics* (SIOW; TIROPANIS; HALL, 2018). *Identification* is mandatory for the IoT to name and match services based on the demand. The IoT *sensing* means gathering data from related objects within the network and sending it back to the cloud. The IoT *communication* circuits connect heterogeneous objects together to deliver specific smart services. Processing units (e.g., microprocessors (MCU), SOCs, FPGAs) and software applications represent the *computational* IoT ability. As reported in (SIOW; TIROPANIS; HALL, 2018; FREDRIK et al., 2019), IoT *services* can be categorized into identity-related services, information aggregation services, collaborative-aware services, and ubiquitous services. In IoT, the definition of *Semantics* attributes to the qualification of distilling knowledge by distinctive sources to afford the required services (SIOW; TIROPANIS; HALL, 2018).

The vast list of applications and their potential services bring an appropriate amount of expectations and, the latter, investments. In 2013, McKinsey had highlighted a 300% growth in connected IoT devices in the last five years and a potential economic growth rate from 2 to 6 trillion annually by 2025. McKinsey had also shown in (JAMES; MICHAEL; JACQUES, 2013) its prediction of market share by 2025, as depicted in Fig.1.2a. In 2019, McKinsey updated these numbers, keeping the same optimism and presenting more interesting parameters (FREDRIK et al., 2019). At that year, the annual economic benefits related to the IoT were expected to reach 3.9 trillion to 11.1 trillion by 2025 (2X times compared to 2013). Moreover, the businesses number that use IoT technologies had increased from 13 % in 2014 to about 25% in 2019, the number of IoT-connected edge nodes around the world was predicted to escalate to 43 billion by 2023, and investments were projected to grow at 13.6% per year through 2022 (JAMES; MICHAEL; JACQUES, 2013; FREDRIK et al., 2019). Fig.1.2b also emphasizes (red square) that there is still room for economic growth in the device layer (edge devices or IoT nodes, which are the

Figure 1.2: a) McKinsey shows in 2013 its prediction of market share by 2025 (JAMES; MICHAEL; JACQUES, 2013) b) Significant opportunities along the IoT technology layers, highlighting a healthy market growth for edge devices (FREDRIK et al., 2019).

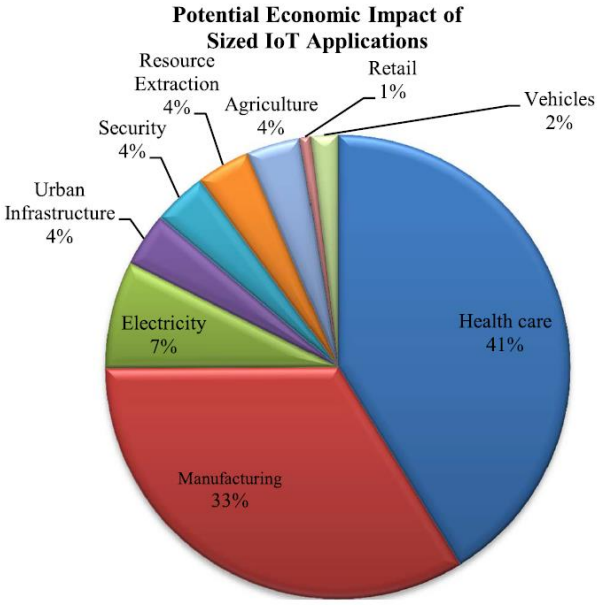

a) 2013

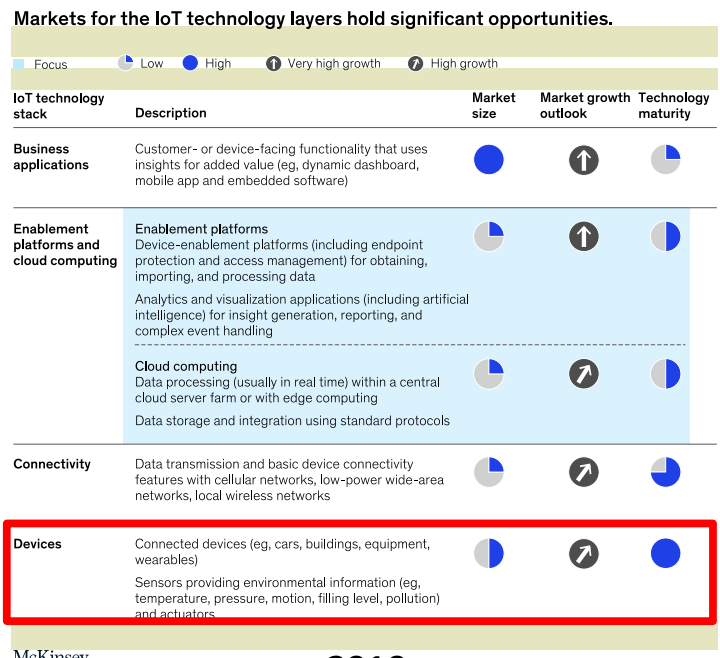

2019

b)

Figure 1.3: The IoT architecture. (a) Three-layer. (b) Middle-ware based. (c) service-oriented architecture (SOA) based. (d) Five-layer (AL-FUQAHA et al., 2015).

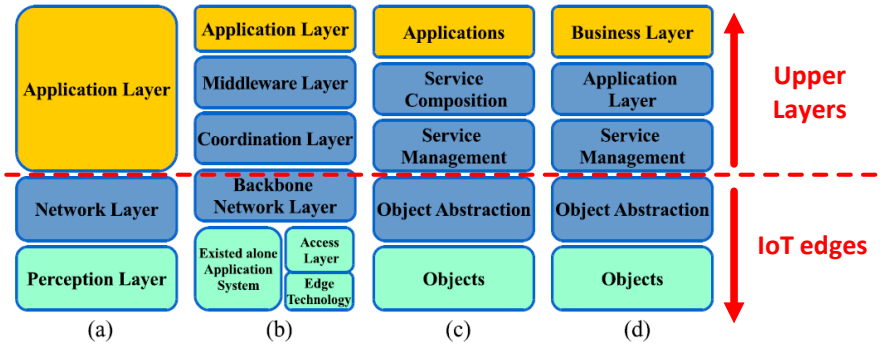

focus of this thesis) within the IoT technological stack. Also, in (FREDRIK et al., 2019), it is quoted that "Smart devices—the foundational layer of the IoT technology stack and the most mature product category—are dominated by large manufacturers and specialist suppliers and enjoy healthy market growth."

Although relatively imprecise, all these speculations point to the potentially significant and fast-paced growth of the IoT, especially applications related to industries and services.

1.2 IoT Network Architecture and Edge Nodes

The IoT architecture must be able to interconnect billions (Giga) or trillions (Tera) of heterogeneous objects through the Internet, demanding a flexible layered architecture (AL-FUQAHA et al., 2015). Fig. 1.3 shows the most relevant IoT technological stacks found so far in the literature (AL-FUQAHA et al., 2015). The basic model is the three-layer architecture consisting of the application, network, and perception layers. Some other models have been proposed adding more abstraction such as middle-ware-based, service-oriented architecture (SOA) based, and five-layers (WU et al., 2010).

Once the five layers have a similar network shape as in current internet protocol (i.e., the Transmission Control Protocol/Internet Protocol- TCP/IP), Al-Fuqaha et al. affirm that the research and standardization point to this direction (AL-FUQAHA et al., 2015). Each layer can be described as follows:

- **Business Layer:** The business layer manages the overall IoT system activities and services. Its responsibilities are to build a business model, graphs, flowcharts, etc., based on the received data from the Application layer. In this layer, it is where is

supposed to be implemented most of the analytics (SIOW; TIROPANIS; HALL, 2018). In addition, monitoring and management of the underlying four layers are achieved at this layer. Once it is very close to the final client, this is the layer with the significant market impact.

- **Application layer:** The application layer provides the services required by the customers (NGU et al., 2017). For instance, the application layer can provide precious information such as data from the sensors to the client who asks for. This layer importance is that it can offer high-relevant smart services to fulfil the customers' needs (NGU et al., 2017).
- **Service Management:** This specific layer matches services to its requester based on addresses and names (NGU et al., 2017). This layer enables IoT applications to work heterogeneously with the data regardless of the hardware platform found below in the stack. In addition, it processes received data, deciding and delivering the needed services over the network protocols (NGU et al., 2017).
- **Object Abstraction:** This layer transfers data produced by the Objects layer to the Service Management layer through secure channels (PALATTELLA et al., 2013). The information can be shared through various technologies such as NFC, ZigBee, IrDA, UWB/IR, ANT, DASH7, Z-Wave, RPL, BTLE, 6LowPAN, 802.15.4, SAN, etc (DECUIR, 2014).
- In the first layer **(perception layer)**, **the smart objects or edge devices**, serves as an IoT external-physical sensors which aim to gather and post-process the relevant information by demand (AL-FUQAHA et al., 2015). Edge devices comprise sensors and/or actuators to perform different functionalities(AL-FUQAHA et al., 2015). Standardized plug-and-play mechanisms still be a challenge in this layer due to their intrinsic heterogeneous characteristics. The perception layer digitizes and transfers data to the Object Abstraction layer through secure channels.

In this entire ecosystem, there is a set of challenges at which one is worthy of being mentioned: availability and reliability. The IoT availability must be considered in the hardware and software levels to provide services for customers anywhere and anytime. Hardware availability refers to the existence of devices that are always compatible with the IoT functionalities and protocols. The challenges related to the hardware system, which generates and collects data (IoT nodes or devices placed on the edges), are deeply investigated here, leading us to conclude the need to design ultra-low-power/area CMOS

Figure 1.4: Modern edge device with embedded intelligence before connecting to the cloud. Analytics can be applied to pre-process the raw data coming from the sensors before sending it upwards for deeper data mining analysis (BEAVERS, 2018).

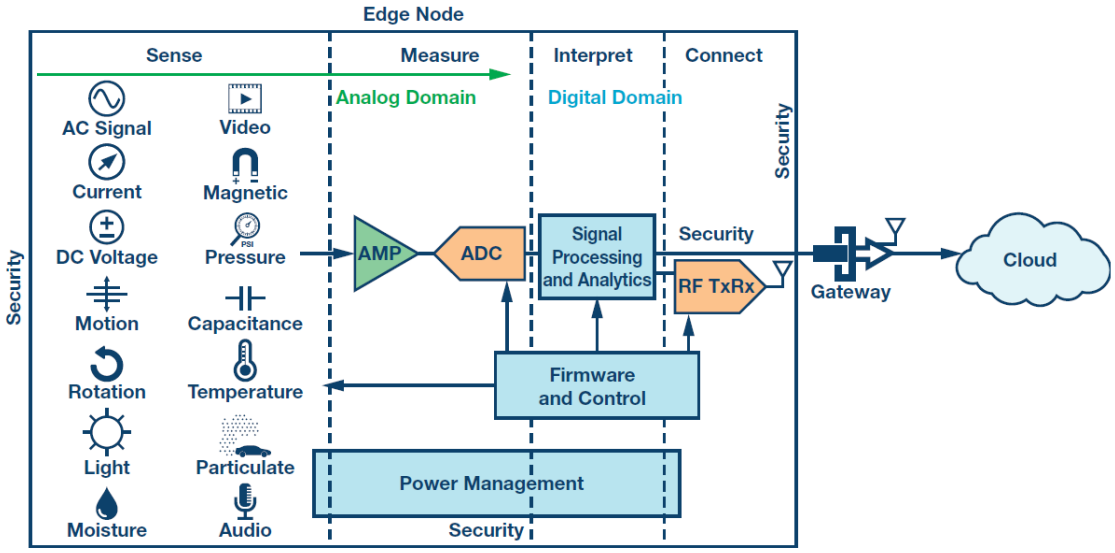

systems. These systems also include analog/RF IoT interfaces.

Fig.1.4 shows an ordinary block diagram for an edge device, which affords some capacity to measure and interpret the raw data before connecting to a gateway, and subsequently, to the cloud (BEAVERS, 2018; ALIOTO, 2017). In this case, the data is processed with some analytics before it is sent for deeper data mining. Albeit the block diagram presented here can be further reduced by eliminating the signal processing and analytic subblocks, i.e., leaving these tasks to the cloud to reduce the total node power/area, the current trend is to increase the computing resources on the edges to minimize the big data issue (CHANG et al., 2014; MORGAN, 2016). A wide spectrum of prepossessing strategies have been studied and proposed in the IoT context such as principle component analysis (PCA) (KORAT; ALIMOHAMMAD, 2019), pattern reduction, dimensionality reduction, feature selection (MARCHIONI et al., 2020), compressed sensing (MANGIA et al., 2020), and distributed computing methods (EL-SAYED et al., 2017).

In the IoT architecture context, embedding more and more computing ability on edges is called Fog Computing (a.k.a. cloudlets or edge computing). Fog resources can perform data aggregation to send partially processed data instead of raw data to the cloud data centers for further processing. Fog resources can be positioned either in intelligent objects or before the cloud data centers; thus, providing a better delay-performance trade-off (AL-FUQAHA et al., 2015) (See Fig. 1.5 for better illustration).

Nowadays, hardware availability to gather and process the environment informa-

Figure 1.5: The role of the cloud and fog resources in the delivery of IoT services (AL-FUQAHA et al., 2015).

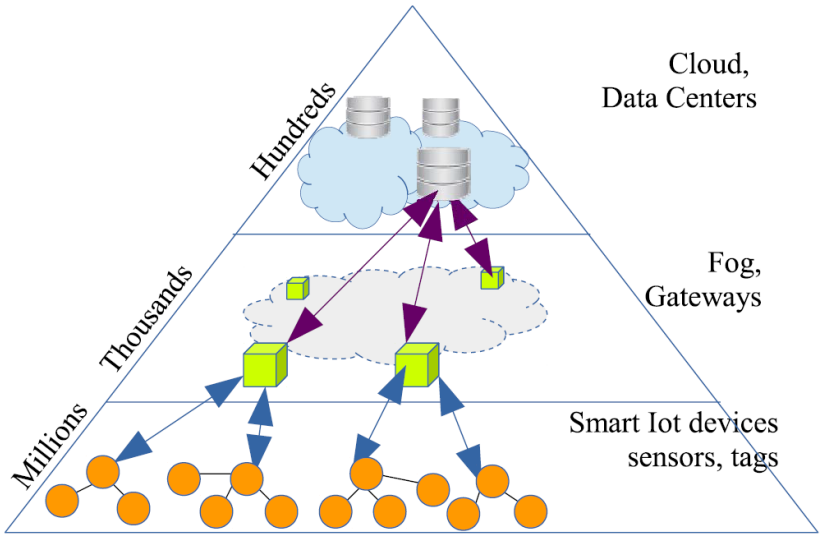

tion is strictly related to the cheapest technology used to develop the IoT nodes, i.e., CMOS technology. Integrated Circuits (IC) techniques connect CMOS devices using electronic design automation (EDA) tools. Such tools follow design flows. The Fig. 1.6 shows a simplified view of the two main IC design flows used to develop the hardware of IoT nodes: digital and analog design flow (MAROLT; SCHEIBLE; JERKE, 2013).

Digital design flow automatically creates the final circuit layout based on a given design specification and design constraints. Depending on a fixed amount of layout components available from a design library as standard cells (logical gates), a high level of automation in digital design is achieved by heuristic algorithms that usually perform the different layout tasks like placement and routing. This automation is also possible due to the discrete nature of digital signals (MAROLT, 2019), reducing the total design time, layout design effort, and time to market.

On the other hand, in the analog/RF domain, design productivity is considerably smaller than for digital circuits, especially in advanced CMOS technologies. As shown in the Fig. 1.6, full custom design flow is adopted to implement analog and RF blocks, simulating their schematic views numerically and doing placements and routing manually to reduce layout-parasitic side effects. This flow is assumed because analog interfaces handle continuous-time, continuous amplitude signals from diverse physical sources (from sensors, for instance), mutual perturbation, and parasitic effects. Such requirements demand to comprehensively harness the entire spectrum and variety of all available degrees of freedom from the process design kit (PDK) components (transistors, capacitors, resis-

Figure 1.6: Simplified IC Digial and Analog Design Flow (MAROLT; SCHEIBLE; JERKE, 2013).

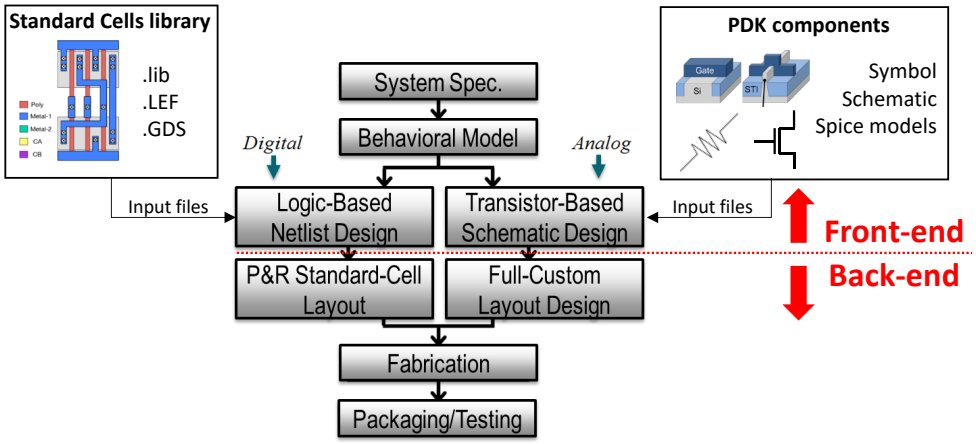

tors, diodes, etc.).

In the next section 1.3, the IC design challenges related to developing IoT nodes are revised based on available devices in the current electronic market, showing the need for new design techniques to reduce analog block power and area. Based on this demand, in the section 1.4, Digital-in-Concept Design Methodologies (DCDM) are introduced and reviewed, defining the fundamental concept for the subsequent thesis chapters.

1.3 IoT Challenges in IC design

1.3.1 General Challenges Based on the IoT Nodes Available on the Market

The integrated circuits IoT nodes, depicted in Fig. 1.4, aim to have sensing and processing capabilities, to be communicatively accessible, unobtrusive (reduced form-factor), cost-effective, untethered (self-powered), and long-lived (to avoid maintenance costs) (ALIOTO, 2021). In 2018, (ALIOTO; SHAHGHASEMI, 2018) released a proper survey regarding the current state-of-the-art of commercial IoT devices, comprising Motes (PCBs), MCUs, and sensor hubs. This survey of commercial IoT devices was done world-wide, using platforms such as Digi-Key to collect the data.

Sensing and processing capabilities in IoT nodes are required to process sensed data locally to a certain extent. Fig. 1.7 shows a histogram of commercial IoT devices embedding each type of sensor (ALIOTO; SHAHGHASEMI, 2018). Temperature sensors are the most widely diffused ones mainly due to their intrinsic compatibility with the

Figure 1.7: A histogram of commercial IoT devices embedding each type of sensor (ALIOTO; SHAHGHASEMI, 2018). This survey of commercial IoT devices was done on a worldwide scale, using platforms such as Digi-Key to collect the data.

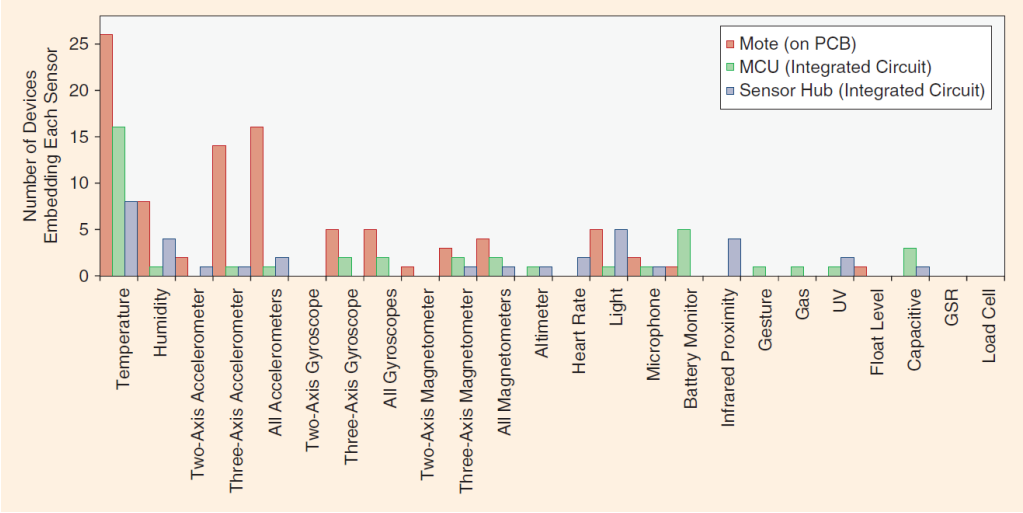

semiconductor itself. However, a drawback is clearly seen in these devices that concerns the interface resolution. Each sensor resolution needs to be tweaked to the maximum resolution across several applications domain to maximize its flexibility, i.e., to cover the largest possible market, it is common to find ADC overdesign adding a relevant energy waste. On average, an Effective Number of Bits (ENOB) of 6.2 bits is the resolution found in this survey within this broad sensor type spectrum.

Some computing power is expected to be available in the IoT nodes to partially process the raw data and deliver more enriched information up to the next layer (CAPRA et al., 2019; CAPRA et al., 2020). In (ALIOTO; SHAHGHASEMI, 2018), all types of IoT nodes are based on microcontrollers. Typically, the microcontroller is an ARM Cortex M0-M4, MSP430, 8051, Atmega, XSCALE, and QUARK. Most of the integrated MCU has 50 MHz of maximum clock frequency while containing 288kB of RAM capacity as a mean value, as justified by their on-chip implementation (see Fig. 1.8). For no-volatile memory, the on-chip flash memory capacity in MCUs is typically around to 64 kilobytes (ALIOTO; SHAHGHASEMI, 2018).

The IoT nodes need to transmit raw, preconditioned, compressed, or distilled data (e.g., extracted features). It can be done either in a wireline or wireless mode. Serial peripheral interfaces (SPIs)/inter-integrated circuits (I2Cs) for intra-sensors communication and universal serial buses (USBs)/universal asynchronous receiver-transmitters (UARTs) for setting information sharing inside of cables are the most common wireline interfaces. For wireless communication, most MCUs operate at 2.4 GHz. At the same time, motes

Figure 1.8: A histogram of maximum microcontroller clock frequency and of RAM memory capacity in commercial IoT nodes (ALIOTO; SHAHGHASEMI, 2018).

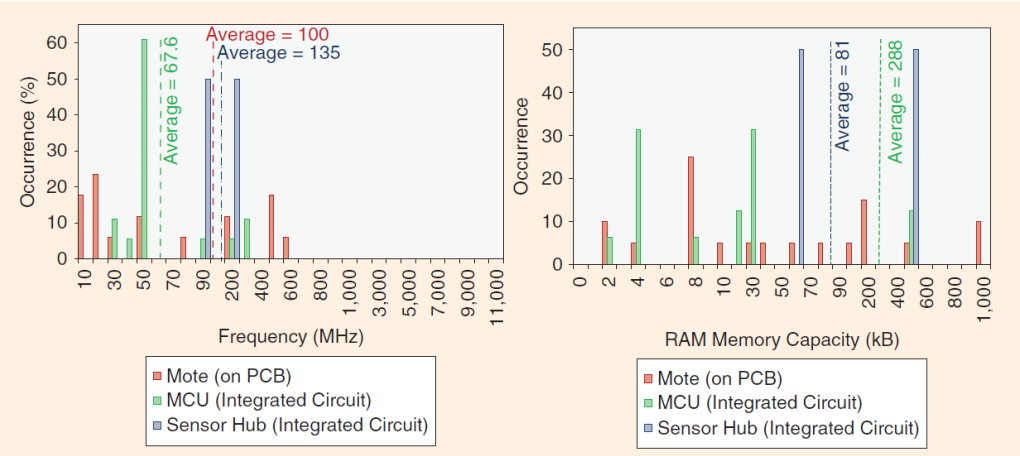

are more diversified in terms of carrier frequency, being 60% working at ISM-band. In contrast, the remaining ones operate at different available bands (i.e., from 315 to 1,900 MHz). Wireless interfaces are well known for a significant fraction of the IoT device power consumption, with best-in-class commercial radios consuming an energy per bit on the order of a few tens of nanojoules per bit (ALIOTO; SHAHGHASEMI, 2018). However, there are numerous academic prototypes with the energy-efficiency around one nJ/bit. The bad news is that the energy/bit is expected to rest relatively constant in the decade ahead (1.34x/year for sub-GHz and 1.42x/year for GHz frequency carrier (ALIOTO; DE; MARONGIU, 2018)). Even worse, during transmission, the energy per bit cannot be further reduced through improvements in modulation techniques and spectral efficiency for the already existing schemes with reasonably low complexity (e.g., on-off keying). They are only 10 times (or 10 dB) surpassing the minimum theoretical limit (ALIOTO, 2017; OTIS; RABAEY, 2007).

The IoT node size is another vital specification once it could enable or jeopardize the application. Following Bell's law, personal computers have been historically shrinking by 10–100× per decade; hence, the IoT is also expected to harness this size shrinking. Fig. 1.9 shows the form-factor of commercial off-the-shelf IoT devices found in the market until 2018. A sub-10mm-scale MCU (with an average size equal to 5.5 mm^2) is encountered, while the centimeter scale is found for motes mounted in PCB, which have more functionalities than the MCUs alone.

Supposing that the goal is to have one trillion devices connected in the following years (global scale principle from section 1.1), taking from Fig. 1.9 the 62 mm^2 as the size of each IoT, this will lead to a total area equal to 0.0000416% of total land earth area,

Figure 1.9: The commercial devices size and cost for distributed sensing (ALIOTO; SHAHGHASEMI, 2018).

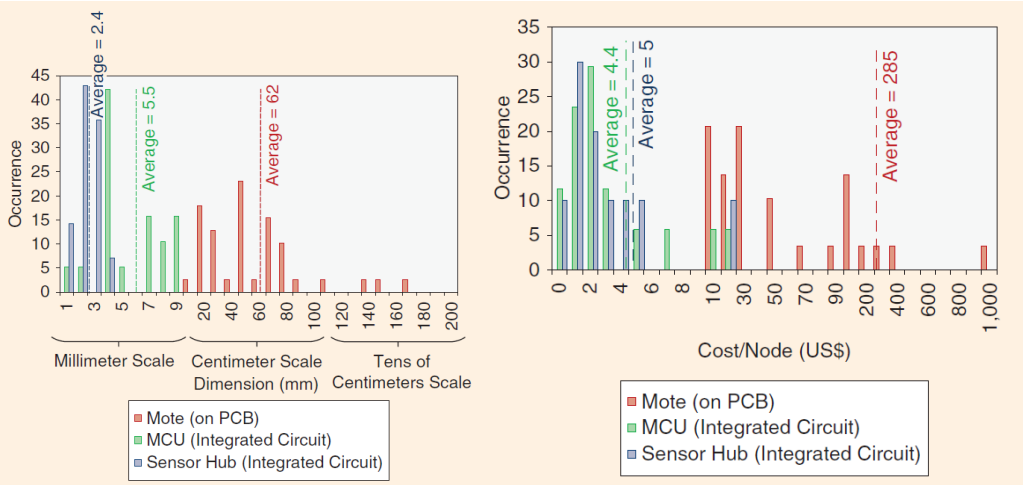

making one trillion a reasonable number. From a manufacturing perspective, as described in (AITKEN, 2017), if it is assumed 2 mm^2 per IoT sensor device (a little lower than sensor hub from Fig. 1.9), or 35,000 packed ICs per 300mm wafer, a trillion devices would need 28 million wafers. That is ≈3X the annual capacity of the industry's largest foundry (Taiwan Semiconductor Manufacturing Company or TSMC until the date of this thesis); but just one third of 2017's total annual worldwide production. So in this context, it is still achievable (AITKEN, 2017).

Also, in Fig. 1.9, the cost per device type is plotted. For the motes, the average cost/node is about 285 dollars. Such high cost is mainly due to the lack of economy of scale in PCB-based motes (PCB manufacturing and assembly costs, for instance). According to the International Monetary Fund (IMF), in 2020, the United States Gross Domestic Product (GDP) was 20.93 trillion, 14x less than 1 trillion times 285 dollars. It gives us insight into the amount of money involved to deploy one trillion devices and shows that the value of $285/mote is unfeasible. Therefore, a significant reduction in cost/unit is essential.

Even though this scenario is more favorable for integrated MCUs (1/4 of USA GDP), it seems that maintenance cost per device would be of the same order of magnitude if each device needed at least one repair per year (for instance, to change the battery). In (ALIOTO, 2021), a maintenance estimation is done, and tens of dollars for each battery replacement is predicted, corresponding to an unbearable ≈$4 trillion (or higher) per annum globally. In this perspective, the IoT node power consumption becomes an essential parameter.

Figure 1.10: A histogram of standby current and the estimated lifetime of commercial IoT nodes at 1% duty cycle. (ALIOTO; SHAHGHASEMI, 2018).

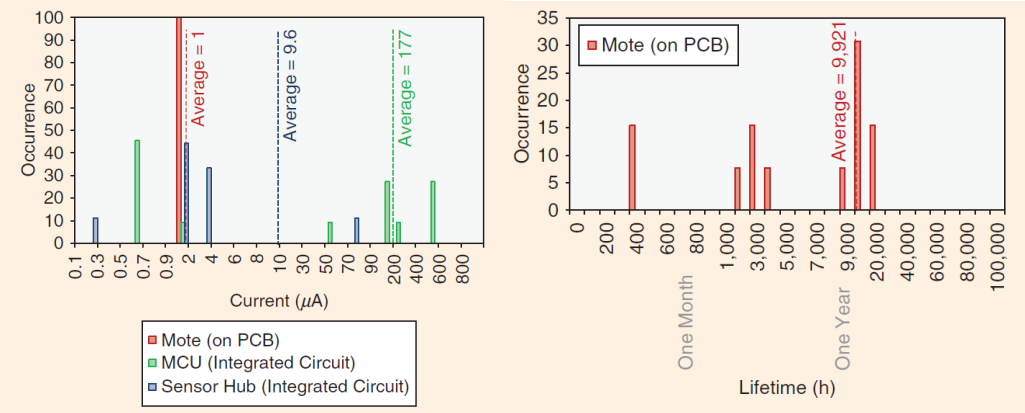

For low area IoT nodes (one of the primary goals of this thesis), lower power consumption leads to better miniaturization for a given lifetime target, as the battery mainly sets the system size. It also leads to significantly lower costs once battery cost becomes a significant fraction of the whole system. Eq. (1.1) shows how the lifetime of an IoT node is calculated (ALIOTO, 2021).

$$T_{lifetime} = \frac{E_{BAT}(0)}{P_{stdby} \cdot (1 - DC) + \overline{P_{system}} \cdot DC + P_{self-discharge}} \tag{1.1}$$

where $T_{lifetime}$ is the total lifetime, $E_{BAT}(0)$ is the battery capacity, P_{stdby} is the IoT node standby power, $\overline{P_{system}}$ is the IoT node active power, $P_{self-discharge}$ is the battery self-discharge and $DC = \frac{T_{on}}{T_{on}+T_{stdby}}$ is duty cycle ratio which defines how much time the system is between active (T_{on}) and standby (T_{stdby}) mode. Eq. (1.1) is true for time-driven duty-cycled systems, where the IoT node activation can be duty-cycled ($DC = \frac{T_{on}}{T_{on}+T_{stdby}}$) by introducing the standby mode (or sleep mode) with short and periodic wake-up ($T_{wkup} = T_{stdby} + T_{on}$). Lower DC ($T_{stdby} >> T_{on}$) means more power is saved to the detriment of an increased probability of missing events of interest and higher event detection latency (ALIOTO, 2021).

In (ALIOTO; SHAHGHASEMI, 2018), commercial IoT devices' lifetime (motes in this case) has been estimated using two AA batteries as power supply to earn more insight into the dynamic powering of IoT systems. Each AA battery has 2600 mAh of capacity and 5 μA of self-discharge current. Assuming 1% duty cycle (DC) and 1 μA of standby current under $V_{DD} = 3.6V$, Fig. 1.10 shows an average lifetime of one year. Using Eq. (1.1), the average active power ($\overline{P_{system}}$) can be also estimated, which is around

Figure 1.11: System lifetime versus system power $\overline{P_{system}}$ for different batteries. (ALIOTO, 2021; SEPULVEDA; SPEULMANNS; VEREECKEN, 2018). $DC = \frac{T_{on}}{T_{on}+T_{stdby}}$ is the duty cycle ratio which defines how much time the system is between active (T_{on}) and standby (T_{stdby}) mode.

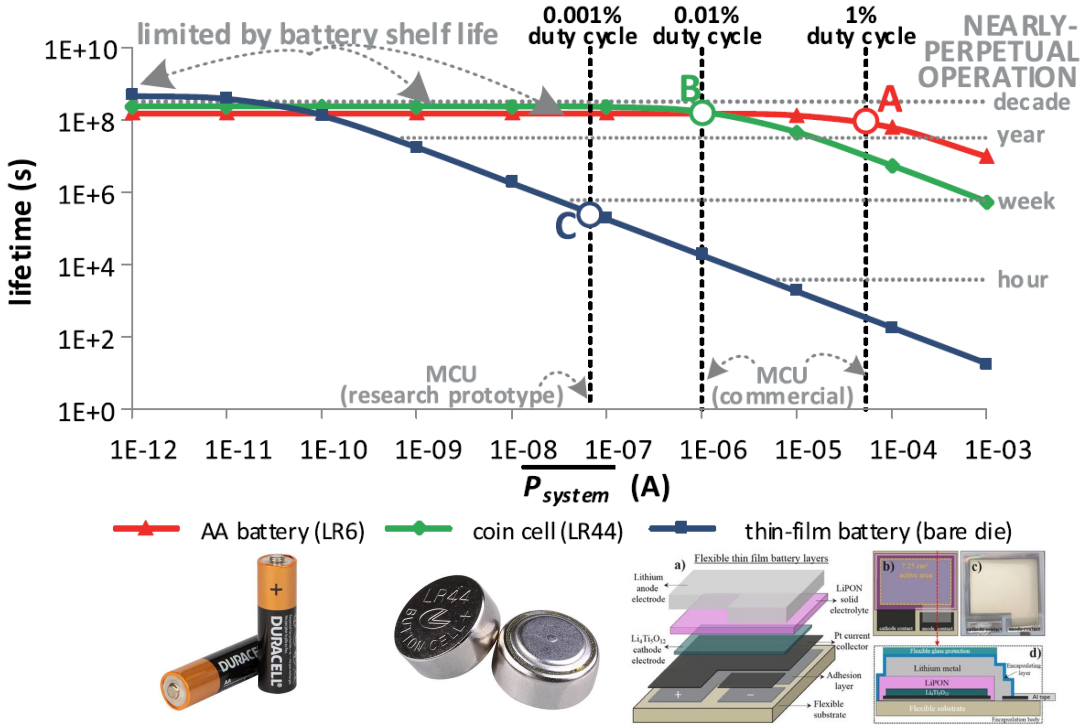

186.5 mW. For the current IoT nodes available on the market, at least two/three orders of magnitude improvements in energy efficiency are required to meet the IoT device's ultimate goal of a decade-long life (no maintenance cost regarding battery issues).

Basically, IoT nodes must be more energy-autonomous, given their massive number of installed devices. Operation in the microwatt and sub-microwatt range is typically required for a decade-long lifetime under the given device size constraint (ALIOTO, 2021). Fig. 1.11 shows the IoT node lifetime versus the total system power $\overline{P_{system}}$ for different batteries (AA battery, coin cell, and thin-film battery (TFB)). Regardless the battery nature, the lifetime upper bound is approximately one decade, limited by the battery shelf life calculated using Eq. (1.1) for $P_{stdby} = \overline{P_{system}} = 0$. From this picture, it can be realized that only a few days of autonomy are achieved for TFB and using commercial MCU with $DC = 0.001\%$. For research MCU prototypes, the autonomy can reach up to one week for a more aggressive DC, even though just a hundred nW is consumed. As shown in the picture, one solution would be to change the battery type for the coin cell, increasing the whole system form-factor and cost once bare-die (i.e., unpackaged) solid-state batteries are as inexpensive as standard silicon dice (deep sub-$).

Figure 1.12: Required harvester size for a given power target for several types of harvesters (ALIOTO, 2021).

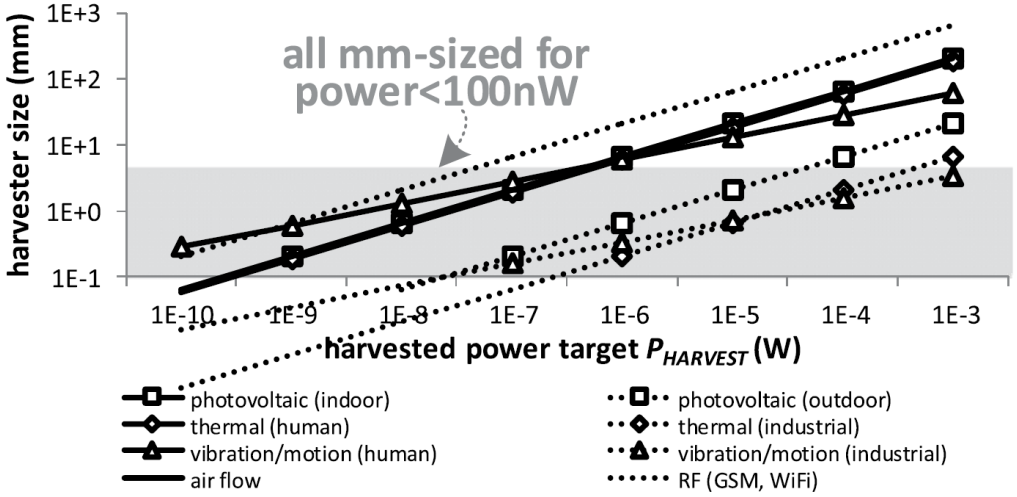

Another alternative is to harvest the surrounding available energy sources. Energy harvesters allow the usage of rechargeable batteries with relaxed single-charge capacity and hence small form factor and low cost while still preserving the battery life (Hybrid solution). Fig. 1.12 depicts the necessary harvester size for a given power target for several types. Based on that, an mm-scale harvester is enough to power 100 nW regardless of its nature, making the system either battery-light or battery-free (direct harvesting).

In fact, regardless of the energy source type (battery or harvester), low-power IoT systems are indispensable. In the following subsections, digital and analog circuit techniques for power reduction are revisited.

1.3.2 Digital Circuit Techniques For Power Reduction

In the previous subsection, at least one order of magnitude gap between the current status of commercial IoT devices and their ultimate targets has been identified in most aspects (e.g., lifetime). Such limitations are all tightly associated with the inadequate power efficiency of existing devices. In other words, the size-lifetime-cost of IoT nodes will eventually be dominated by the energy source (e.g., battery), and improvement of their power efficiency will be necessary for making the battery more minuscule (less expensive) and their energy harvester in sub-mm-scale while extending the lifetime.

Due to these reasons, to keep the IoT dream alive using CMOS technologies, integrated circuits and distributed sensing systems must be essentially battery-light or

battery-less with the lowest power/area possible while trading off the processing workload w.r.t. the entire IoT network stack (fog computing, see Fig. 1.5).

In digital circuits, scalable energy–quality operation is a valuable tool for low-power design. It dynamically manages the tradeoff between energy and data processing quality, minimizing the former to achieve just-enough quality (Aiello; Crovetti; Alioto, 2019). The application itself dynamically sets the quality target (PAIM et al., 2021; SEIDEL et al., 2021). IoT nodes can considerably benefit from energy–quality scaling, considering that their processing deals with physical signals, which are noisy and hence can be processed with a quality that is commensurated with the level of noise and the acceptable accuracy required by the task at hand.

Dynamic Voltage Scaling (DVS) (DIGHE et al., 2011; WANG et al., 2016; LIN et al., 2015) and body biasing (JUSTO; CAVALHEIRO; MOLL, 2017; LANUZZA; TACO; ALBANO, 2014) are powerful techniques for low-power digital design in static CMOS logic family. Still, typically energy reduction by up to 2 orders of magnitude at ULV is obtained with a speed penalty by 2–5 orders of magnitude. An aggressive pipeline to further reduce the energy per operation is also a good option (JAIN; LIN; ALIOTO, 2018).

In schematic level, a dedicated standard cells library (stdcells) is also a good design approach to reduce further the absolute power, and energy (TIMARCHI; ALIOTO, 2016). For instance, higher threshold selection is a more relevant circuit knob compared to the transistor sizing itself. Logic gates with fan-in greater than 2-3 (i.e., no more than two stacked transistors) as well as topologies based on current contention must be avoided. During the transistor sizing, the PMOS/NMOS imbalance is a crucial design parameter that strongly influences the robustness of the stdcells (ALIOTO, 2012).

Not only changing the circuit design approach for CMOS static family makes the difference for digital circuit power reduction, but the development of new logic families has also been demonstrated significantly efficient. Fifteen years ago, David Bol proposed a new family of ultra-low-power low-frequency logical gates (BOL et al., 2007), now known as Dynamic Leakage-Suppression (DLS) Logic (LIM et al., 2015). This kind of logic permits putting the transistor in the super-cutoff region after the transition is done, though suppressing the leakage current and limiting the short circuit current during the state transition. Such operation leads to shallow power consumption levels enabling new horizons for battery-light and direct-harvesting IoT applications. Its drawback comes from the limited speed and low voltage swing compared to static CMOS. Fig.1.13a shows

Figure 1.13: a) DLS inverter cell, schematic and layout (LIM et al., 2015) b) CMOS and DLS comparison for a MCU implementation (TRUESDELL et al., 2019) c) Dual-Mode Standard Cells (LIN; JAIN; ALIOTO, 2020) or Scalable Dynamic Leakage-Suppression (SDLS) logic style (TRUESDELL et al., 2019) d) Gate count in Kgates versus minimum power consumption in state of the art MCU (ALIOTO, 2021).

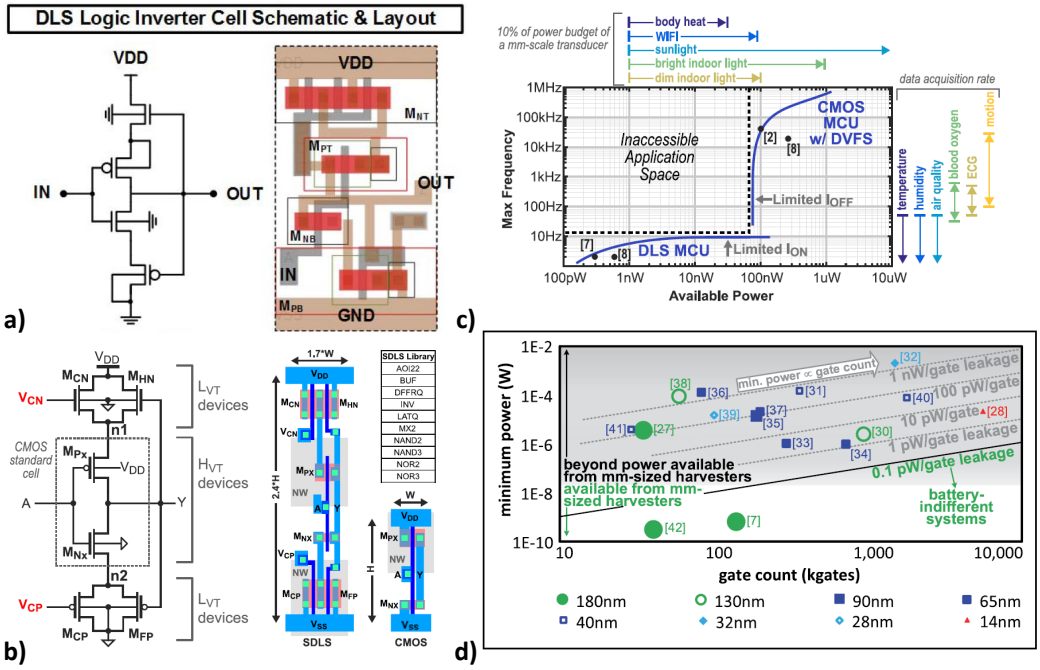

a DLS inverter cell in schematic and layout. In Fig.1.13c (TRUESDELL et al., 2019), a comparison between CMOS and DLS logical style is seen in terms of power and maximum frequency operation for an MCU implementation. It shows sub-100nW power consumption is possible using DLS logical style.

A variant of DLS called as Dual-Mode Standard Cells (LIN; JAIN; ALIOTO, 2020) or as Scalable Dynamic Leakage-Suppression (SDLC) logic (TRUESDELL et al., 2019), shown in Fig. 1.13c, has also been proposed. SDLC allows an ultra-wide power-performance trade-off considerably beyond the classical static CMOS voltage scaling and adaptation to the sensed power/energy availability from the harvester and battery, as demonstrated in (LIN; JAIN; ALIOTO, 2020). Finally, in (ALIOTO, 2021) and also in Fig. 1.13d, it is shown that DLS is the unique logical style so far able to operate an MCU consuming sub-10nW power consumption.

1.3.3 Analog Circuit Techniques For Power Reduction

Generally speaking, the design of low-power and low-voltage analog circuits is the talent for finding the suitable trade-off between conflicting constraints or specifications,

Figure 1.14: a) analog design octagon b) $g_m/I_D \cdot f_T$ versus the inversion coefficient IC, λ_c is the parameter corresponding to the fraction of the channel in which the carrier drift velocity reaches the saturated velocity over a portion of the channel geometrical length (RAZAVI, 2002; ENZ; CHICCO; PEZZOTTA, 2017a) c) Performance difference between analog and digital blocks over time (MURMANN, 2006; Murmann, 2006) d) Area reduction over the years of the bitcell SRAM, OTA and Bandgap reference (Aiello; Crovetti; Alioto, 2019).

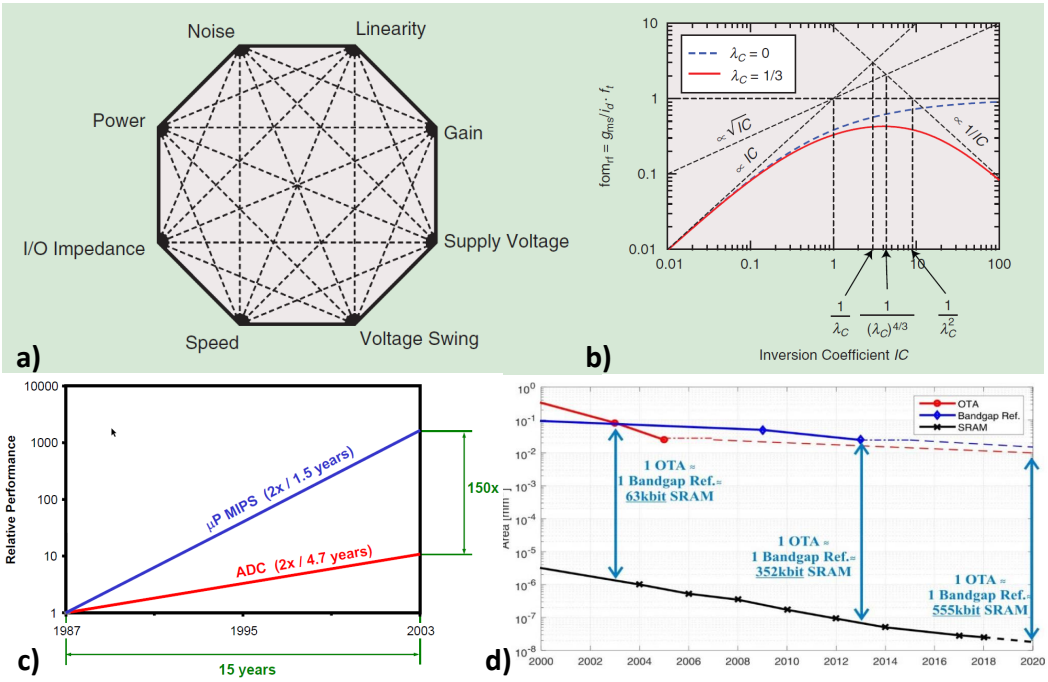

as illustrated by the famous analog design octagon (RAZAVI, 2002; ENZ; CHICCO; PEZZOTTA, 2017a), in Fig.1.14a. Power, noise, linearity, gain, supply voltage, voltage swing, speed, and input/output impedance are some parameters typically found during the analog IC design (see Fig.1.14b).

Usually, in the literature about analog design strategies for low power goals, the transistor bias point is the leading circuit knob investigated. In (ENZ; CHICCO; PEZZOTTA, 2017b), the transistor inversion level (bias point) is deeply related to essential Figures of Merits (FoM), like transconductance efficiency (g_m/I_D), transit frequency (f_T), and the product $g_m/I_D \cdot f_T$. The latter achieves a maximum in moderate inversion (between strong and weak inversion operation), providing a good tradeoff among gain, noise, and current consumption. In addition, analog designers based on the fundamentals of MOSFET principles for all performance use the MOSFET operating plane (see Fig. 1.15a), which illustrates the tradeoffs in performance for the selected inversion coefficient and channel length (BINKLEY, 2007). A complete version including temperature behavior of MOSFET transistor is also proposed in (TOLEDO et al., 2015; CORDOVA;

Figure 1.15: (a) The MOSFET operating plane illustrating tradeoffs in performance for the selected inversion coefficient and channel length. Copyright John Wiley and Sons Limited (BINKLEY, 2007). (b) MOSFET operating plane translated to Unified Charge-Control Model (UCCM) (SCHNEIDER; GALUP-MONTORO, 2010; TSIVIDIS; MCANDREW, 2010) model presented before including temperature behavior of MOSFET transistor presented in (CORDOVA; TOLEDO; FABRIS, 2014; TOLEDO et al., 2015).

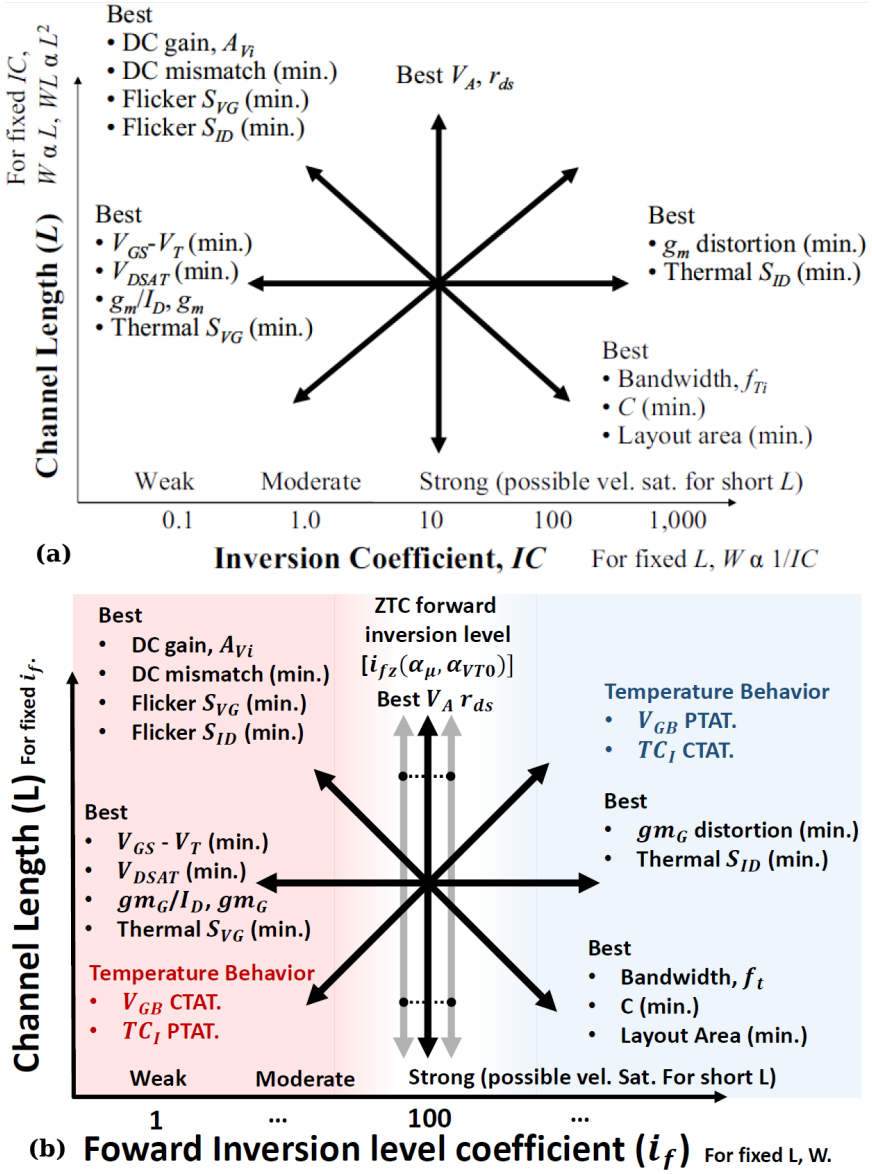

TOLEDO; FABRIS, 2014), as shown in Fig. 1.15b.

Looking in this MOSFET operating plane, if it is necessary to reduce the power, more area is required (e.g., increasing the transistor length). The reduction of power consumed by the transistor is also intrinsically related to the minimum noise level produced by itself, leading to a trade-off between power, area, and noise. This trade-off, most of the time, can not only be evaluated for a standalone transistor but how is its impact on the entire circuit performance, conducting us back to the general picture presented in

Fig.1.14a. In summary, reducing power in an analog block is a topology-dependent issue and involves multi-performance trade-offs. This condition states a complex problem to be generalized, unlike seen in the digital circuit at which, roughly speaking, three constraints have to be traded-off: timing, power, and area.

The analog block power can also be reduced, making it work in very-low voltage supplies (V_{DD}). For low voltage analog designs (GALUP-MONTORO; SCHNEIDER; MACHADO, 2012; MELEK; SCHNEIDER; GALUP-MONTORO, 2018), some design tips are highlighted in (KINGET, 2007), such as to use reverse-short-channel effect (RSCE) and forward body-bias techniques at the device level. At the block level, eliminating transistor stacks and taking advantage of local CMFB, CMFF, and negative transconductance generators is usually necessary to make the circuit work properly. Finally, at the functional level, revising signaling/architecture and new tuning/biasing strategies is extensively adopted to improve the whole block performance.

Even though all the techniques mentioned above make the difference in whole analog system performance, a DC bias current is always needed, setting a lower bound to the minimum power consumption. Fig. 1.14c shows the performance difference between analog (ADC) and digital (μP) blocks over time. In this illustration, a 150X difference can be found (MURMANN, 2006; Murmann, 2006); one of the reasons for this gap is the biasing circuits within the analog blocks, which do not scale well for new technological nodes. Furthermore, as shown in Fig. 1.14d, analog blocks do not scale well for what concerns silicon area (Aiello; Crovetti; Alioto, 2019). As has happened to the TTL family in the 70s, where the implementation of the CMOS logical family eliminated its static power consumption, it is time to either get rid of the quiescent point of analog blocks or make it more dynamic to improve the analog power consumption, taking advantage of the CMOS scaling. In section 1.4, the analog interfaces signaling and architectures are revisited, showing the new analog/RF IC design trend over the last years and its compatibility to low power/area performance.

From the IC design flow perspective, even though full custom design flow (used during the implementation of an analog block) tends to reach better circuit performance, it requires a long design time, heavy manual layout, labor-intensive and error-prone tasks. Because of that, there have been several prior efforts to automate analog layout synthesis (ALS) (EICK et al., 2011; FERREIRA et al., 2016; LIN et al., 2016; GRAEB, 2012; LIU et al., 2020; CHEN et al., 2021; DHAR et al., 2021; CROSSLEY et al., 2013). ALS automation can decrease significantly the design effort as can be seen in last publications

(CHEN et al., 2021; DHAR et al., 2021); but it is still incipient when compared to the current digital flow. Even worse, ALS has as benchmark traditional analog schematics, which do not improve for new CMOS nodes. On the other hand, digital flow is more automatic, portable, mature, and improves the time-to-market, achieving a reasonable block performance. For new technological nodes, where the layout design team has two times the designers compared to the schematic group, turning the analog/RD block more digital-like can be more attractive in design effort and performance.

Based on that, the following section presents the idea of Digital-in-Concept Design Methodologies (DCDM) for analog/RF blocks and its current state-of-the-art.

1.4 Digital-in-Concept Design Methodologies (DCDM)

The IoT requirements are challenging to be met for analog interfaces, which do not take advantage of CMOS geometrical scaling (Kinget, 2015; Xu et al., 2017; Aiello; Crovetti; Alioto, 2019b) and face specific design challenges due to the poor analog features of nanoscale transistors (as the feature size is shrunk from 0.5 to 0.022 μm node, the MOS intrinsic gain downfalls from 180 to 6 V/V (XU, 2019), while the transistor f_{T} increases by 25X, from $16\,\mathrm{GHz}$ to $400\,\mathrm{GHz}$) (Xu et al., 2017) and to the reduced signal swing at sub-1V power supply voltage. Such drawbacks entirely offset the potential benefits of CMOS scaling in terms of reduced parasitics and negatively impact the area, performance, energy efficiency, and especially the design effort of analog cells in advanced technology nodes. Given that, there have been almost no net power advantage (Kinget, 2015), and no area reduction in analog cells like Operational Transconductance Amplifiers (OTAs) or bandgap references when moving from older to more recent technologies (Aiello; Crovetti; Alioto, 2019b). In addition, analog ICs are characterized by poor reconfigurability and portability across technology nodes compared to digital ICs and require significant time and effort in design, transistor-level optimization, simulation, full-custom layout, physical verification, and prototyping (Xu et al., 2017; Crovetti et al., 2019).

Because of these limitations, there has been intense research interest in implementing traditionally analog blocks by digital-friendly and digital intensive replacements in the last years. This trend can also be observed in the number of CAS Transactions papers on related topics reported in Fig.1.16, which more than doubled in the last decade. This is defined here as **Digital-in-Concept Design Methodologies (DCDM)** trend (TOLEDO

Figure 1.16: Digital intensive analog/RF building block published in TCASI transactions over the last 10 years (TOLEDO et al., 2021).

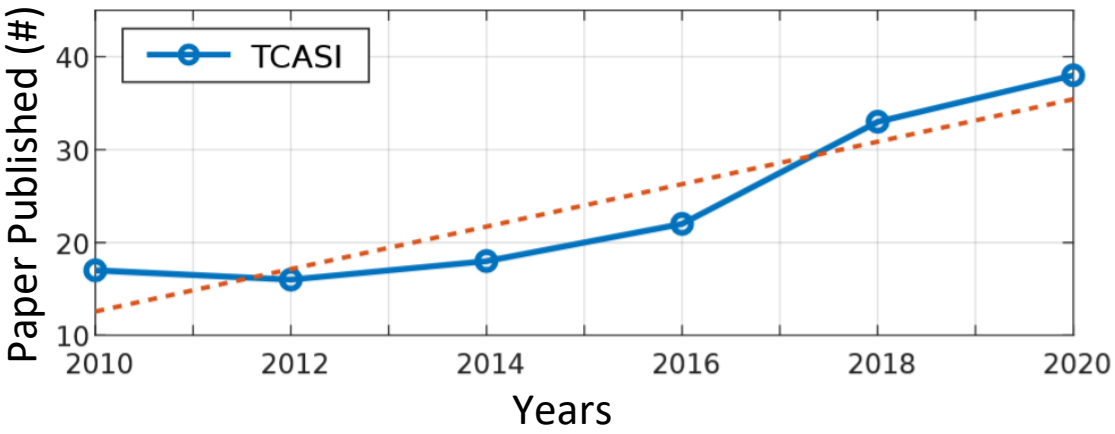

et al., 2021).

DCDM suggests that analog/RF circuits can take advantage of better awareness of the discrete nature of information (TOLEDO et al., 2021) and that digital circuits can perform their functions. Following this tendency, fully digital phase-locked loops (PLLs) (Staszewski et al., 2004; Park; Wentzloff, 2011b; Deng et al., 2015), synthesizable A/D converters (ADCs) based on successive approximation registers (SARs) (Seo et al., 2018; Aiello; Crovetti; Alioto, 2020; Park; Hwang; Jeong, 2019) and on domino-logic (Weaver et al., 2011), stochastic flash ADCs (Weaver; Hershberg; Moon, 2014; Fahmy et al., 2015) and VCO-Based ADCs (Waters; Moon, 2015; Straayer; Perrott, 2008; Taylor; Galton, 2010; Nguyen; Schembari; Staszewski, 2018; Gielen; Hernandez; Rombouts, 2020a; Gielen; Hernandez; Rombouts, 2020b; Unnikrishnan; Vesterbacka, 2014; Jayaraj et al., 2020) have been proposed, extensively investigated and are increasingly employed in applications. Highly digital D/A converters (DACs) (Crovetti, 2017; Ansari; Wentzloff, 2014; Crovetti; Rubino; Musolino, 2020; Aiello; Crovetti; Alioto, 2019a; Aiello; Crovetti; Alioto, 2019), voltage comparators (Aiello; Crovetti; Alioto, 2018; Zou; Nakatake, 2020; Li et al., 2020), oscillators (Aiello et al., 2019), low-dropout regulators (LDOs) (Yasuyuki Okuma et al., 2010; Bang et al., 2020; Cai; Zhan; Lu, 2019; Tang et al., 2018; Lu et al., 2020; Qian et al., 2020), buck converters(Kim et al., 2015; Krishna Chekuri et al., 2020), filters (Drost; Talegaonkar; Hanumolu, 2012; Liu et al., 2018), voltage references, (Crovetti, 2015; Cai, et al., 2017; Eberlein; Pretl; Georgiev, 2019), temperature sensors (Tejasvi; Makinwa; Hanumolu, 2016) and OTAs (Toledo et al., 2020; Toledo et al., 2019; Toledo; Aiello; Crovetti, 2019; Crovetti, 2013; Kalani; Kinget, 2020; Kalani et al., 2017; PALUMBO; SCOTTI, 2021; CENTURELLI et al., 2022) have also

been proposed. This trend can be noticed not only at block-level, but also at system-level, considering that mostly-digital RF transmitters (Park; Wentzloff, 2011a; Crovetti, 2020; Buckel et al., 2018; Un et al., 2020; Gebreyohannes et al., 2018), receivers (Opteynde, 2010; Kuo et al., 2017; Staszewski et al., 2004), and biomedical front-ends (Huang et al., 2018; Crovetti, 2012; Gielen; Hernandez; Rombouts, 2020a; Gielen; Hernandez; Rombouts, 2020b), have also been introduced. Indeed, it is reasonable to claim that a "digital revolution" in analog blocks is now happening, and it can be clearly observed in two common threads.

The first thread is the effort in moving information processing from the amplitude to the time domain (Gielen; Hernandez; Rombouts, 2020a; Gielen; Hernandez; Rombouts, 2020b; Yuan; Parekh, 2020; Rahiminejad et al., 2020; Kim et al., 2019; Richelli; Colalongo; Kovács-Vajna, 2020), which has an intrinsic advantage in nanoscale CMOS. In more advanced CMOS nodes, timing resolution, as opposed to amplitude resolution, is steadily increasing due to the minor delays of digital gates (the fan-out-of-4 (FO4) delay of an inverter has decreased by from 140ps (0.5μm) to 6ps (22nm node), i.e., by 23X (Xu et al., 2017)).

The second thread encompasses the research activities developed in the last years to extend digital automated design techniques to analog and RF systems. Although promising semi-automatic analog design techniques like procedure-based layout generation and optimization-based layout synthesis have been proposed in the last years (CHEN et al., 2020; CHEN et al., 2021; DHAR et al., 2021), the synthesis-friendly analog circuits that use the existing digital flow tools for designing indicate to be the most attractive ones.

These two threads are closely related to each other - since analog circuits based on time-domain information processing are inherently more suitable to automated synthesis, and the functional/logical decomposition and abstraction required for automatic design naturally lead to time-domain, algorithmic processing. Both converge towards the implementation of the functions of analog circuits by *true digital circuits*, in which information is internally processed in the form of two-level digital signals (i.e., *without* using digital gates as analog amplifying stages, as in (Nauta, 1992)). As illustrated in Fig. 1.17a, this new circuit design approach, possibly preceded or not by a minimal, non-critical, passive network that can grasp relevant information from any finite-amplitude, band-limited input signals (voltages and/or currents), can generate the desired band-limited output voltages/currents at a pre-fixed degree of accuracy. Note that, even though passives are needed in some cases, depending on the applications, such elements can be implemented by stan-

Figure 1.17: a) Block diagram of digital-based analog block (TOLEDO et al., 2021) b) Power vs Area for for ADCs (Crovetti, 2017), DACs (Aiello; Crovetti; Alioto, 2019a), OTAs (Toledo et al., 2020), voltage reference (Crovetti, 2015) and oscillators (Aiello et al., 2019).

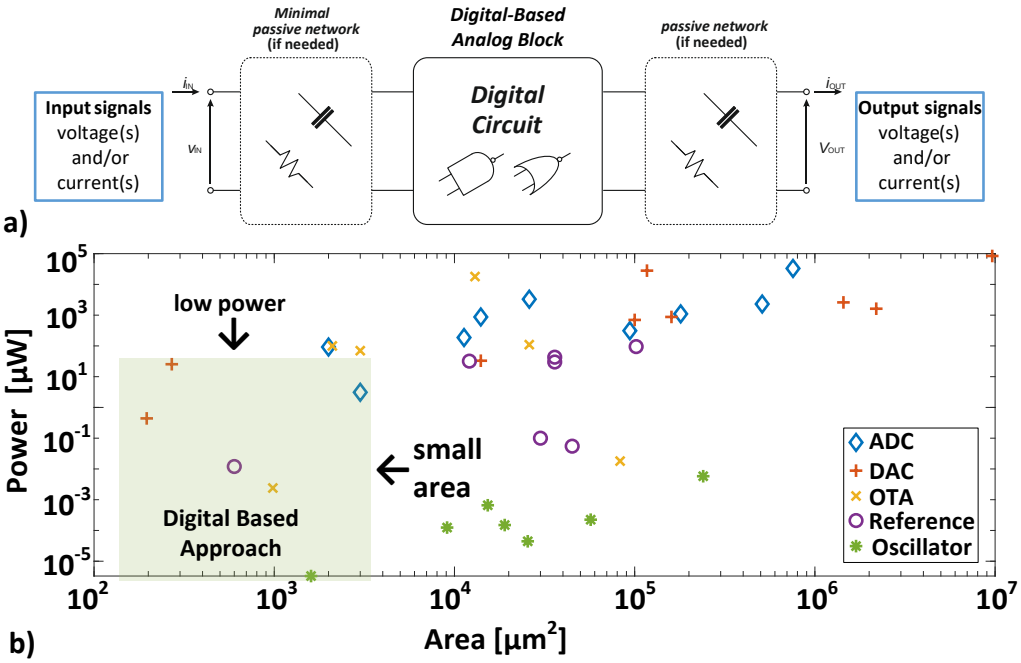

dard cells like using pseudo-resistors (as used in chapter 2).

In (TOLEDO et al., 2021), Fig.1.17b plots power versus area for ADCs, DACs, OTAs, voltage reference and oscillators (Crovetti, 2017; Aiello; Crovetti; Alioto, 2019a; Toledo et al., 2020; Crovetti, 2015; Aiello et al., 2019). Such figure indicates that implementation of the recent analog blocks by DCDM or digital-based approach leads to low power and small area integrated circuits, matching with the IoT nodes needs as mentioned previously in the section 1.3. This thesis investigates this fact, proving that conceivably this is the right path for IoT analog interfaces.

1.5 Thesis Organization

While most of the previously cited solutions address the challenges of analog interfaces by more "digital friendly" analog cells based on traditional design concepts (MURMANN, 2006), the opportunity to implement analog functions with true digital circuits, which fully take advantage of CMOS scaling and of the benefits of a digital design flow, will be explicitly covered in this thesis, demonstrating itself as promising analog design alternative for IoT nodes. Concomitantly, this thesis aims at advancing on

low power/area analog design strategies targeting the current IoT bottleneck on the edge devices: power consumption. **Digital-in-Concept Design Methodologies (DCDM)** are herein contextualized and used to design two digital-based OTAs and one digital-based biosignal amplifier. During the whole DCDM investigation, this thesis produced interesting contributions, which are listed below:

- an ultra-low-voltage/power fully-integrated Digital-Based Operational Transconductance Amplifier (DB-OTA) is demonstrated on silicon in 180 nm CMOS for the first time. Before that, it had been demonstrated using off-the-shelf components. To the best of this thesis author's knowledge, the power achieved by this demonstration is the lowest reported to date in an OTA, reaching the figures of merit that are the best in sub-500 mV OTAs registered so far;
- then, as a second contribution, a new passive-less fully-digital operational transconductance amplifier (DIGOTA) for energy- and area-constrained systems is proposed and silicon-proven. What differentiates the new DIGOTA from the previous one is that the latter has passive-less self-oscillating common-mode compensation, making the circuit less noisy and more compatible with the digital flow;
- using the second OTA version, i.e., the DIGOTA, a power-efficient ultra-low voltage and ultra-low area fully-differential, digital-based Operational Transconductance Amplifier (OTA), suitable for microscale biosensing applications (BioDIGOTA), is proposed and silicon-proven.

The rest of the thesis is organized as follows. The next chapter (i.e., chapter 2) presents a Digital-Based OTA implementation for ultra-low-power/voltage/area applications, followed by a passive-less version with better robustness, area, and signal-to-noise performance in chapter 3. In the chapter 4, the operation principle and the silicon characterization of a power-efficient ultra-low voltage and ultra-low area fully-differential, digital-based Operational Transconductance Amplifier (OTA), suitable for microscale biosensing applications (BioDIGOTA), is discussed. The last chapter draws the conclusion and possible future works to further improve the circuit's performance.

2 DIGITAL-BASED OTA

This chapter shows a silicon demonstration of an embryonic Digital-Based OTA (DB-OTA) published in 2013 (Crovetti, 2013), targeting Ultra Low Power (ULP) and Ultra Low Power (ULP) performance. In the section 2.1, a brief review of the current state-of-the-art for ULP and ULV OTAs is presented, categorizing the OTA topologies in classes and comparing their performance. In the section 2.2, the DB-OTA circuit analysis and design are detailed, followed by its layout description, simulation and measurement results in the sections 2.3, 2.4, and 2.5, respectively.

2.1 Previous art of ULV/ULP OTA Design

In general, ULV OTAs can be classified as gate-driven, bulk-driven, inverter-based, VCO-based, and digital-based topologies.

In (YOON; CHOI; ROH, 2015)(DESSOUKY; KAISER, 2001) gate-driven MOS transistors working in subthreshold regime are exploited (Fig. 2.1a). The minimum power supply and Common-Mode Input Range (CMIR) are limited by $V_{DD} = 3V_{sat} \approx 300mV$ and $V_{CM} = V_{DD} - 2V_{sat} - V_{TH}$, respectively, being V_{sat} the minimum drain-source voltage required to operate a MOS device in saturation and V_{TH} is the threshold voltage. Typically the V_{sat} is deemed to be around $3 \sim 4 \cdot KT/q$ in subthreshold regime (GALUP-MONTORO; SCHNEIDER; MACHADO, 2012).

On the other hand, in (Ferreira; Sonkusale, 2014) (see Fig. 2.1b), bulk-driven input devices are exploited to mitigate the CMIR limitation at the cost of reduced efficiency due to the lower values of the bulk transconductance g_{mb} compared to the gate one g_{mg}. There are many others bulk-driven OTAs proposed in the literature (KHATEB et al., 2021; KULEJ; KHATEB, 2020a; KULEJ; KHATEB, 2020b; KHATEB; KULEJ, 2019), especially after (Chatterjee; Tsividis; Kinget, 2005) has been published. Inverter-based amplifiers (Lv et al., 2019; MICHEL; STEYAERT, 2012; RODOVALHO; AIELLO; RODRIGUES, 2020; PALUMBO; SCOTTI, 2021) (Fig. 2.1c,d) have been proposed to achieve a large equivalent transconductance ($g_{m_{TOTAL}} = g_{m_{PMOS}} + g_{m_{NMOS}}$) under low V_{DD} and voltage headroom. However, they suffer of limited intrinsic gain and common-mode rejection.

Recently, an alternative approach that aims to implement analog functions by digital means (as illustrated in Fig. 2.1a,b) has been proposed for OTA design (PARK; PER-

Figure 2.1: a) Gate-driven (YOON; CHOI; ROH, 2015; DESSOUKY; KAISER, 2001), b) Bulk-driven (Ferreira; Sonkusale, 2014) c,d) Inverter-based (Lv et al., 2019; MICHEL; STEYAERT, 2012).

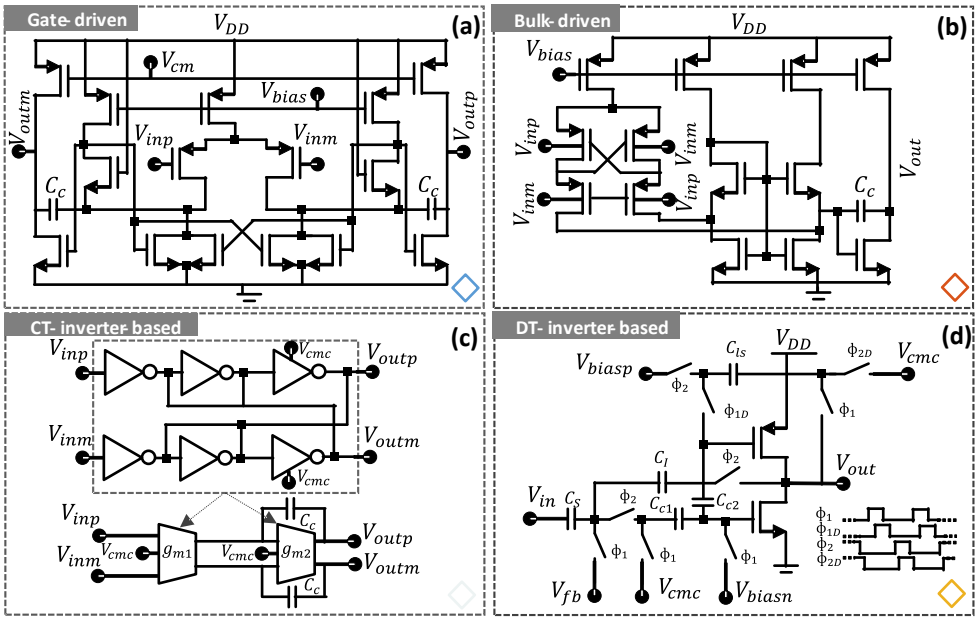

ROTT, 2010; Crovetti, 2013; Kalani et al., 2017; Toledo et al., 2019; CENTURELLI et al., 2022). Both OTAs in Fig. 2.1a,b, VCO-based OTA (PARK; PERROTT, 2010) and a digital-based (Crovetti, 2013) OTA, exploit time-domain information processing and prove to be very good candidates for efficient ULV operation. Figs. 2.3 a, b and c compare V_{DD} versus FOM_S (as defined in Eq. (2.1)), C_L versus power and area versus power between all schematics depicted in Fig. 2.1 and 2.2. Such figure shows that the digital-based OTA consumes less area and power compared among the OTAs considered in the comparison. The following section 2.2 presents the circuit analysis and design of a Digital-Based OTA (DB-OTA) and its silicon measurements.

$$FOM_S = 100\frac{GBWC_L}{I_{DD}} \tag{2.1}$$

2.2 Circuit Analysis and Design

2.2.1 Qualitative Circuit Analysis

In (Crovetti, 2013), the possibility to translate into digital the operation of a MOS differential pair has been explored. To do this emulation, understanding how the common-

Figure 2.2: a) VCO-based (Kalani et al., 2017; Kalani; Kinget, 2020) b) Digital-based (Toledo et al., 2019) topologies.

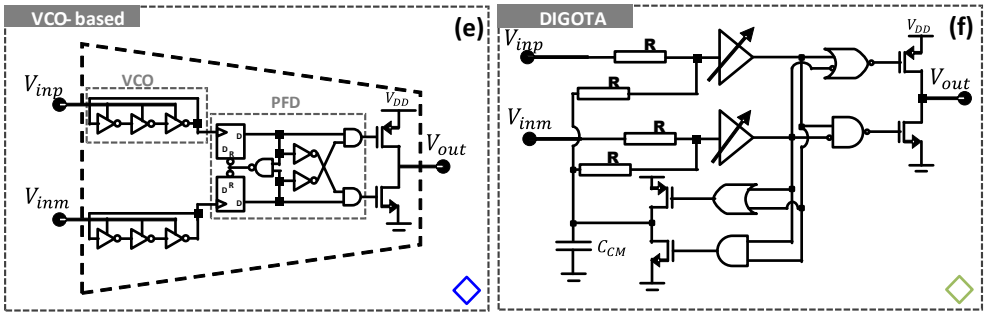

mode signal is tracked and attenuated in traditional architecture like the MOS differential pair (Gray; Meyer, 1982), as shown in Fig. 2.4, is very helpful.

In a standard NMOS differential pair, the Common-Mode (CM) signal is tracked by the voltage V_{S} of the common-source node S, and is subtracted from the external inputs in the gate-source voltages of the input devices, so that the control voltages of the input devices are CM-voltage independent and their drain currents are proportional to the differential mode input v_{d} (Toledo et al., 2015). In other words, V_{S} node continuously-time follows the $V_{CM} = \frac{V_{IN+}+V_{IN-}}{2}$, while remains static when $v_d = V_{IN+} - V_{IN-} \neq 0$.

In (Crovetti, 2013), it was demonstrated that a similar behavior can be obtained from two digital buffers after adding a CM signal tracker and summing network (i.e., to mimic similar V_S behavior of a traditional differential pair).

To sense the analog input signal, a Differential-Mode (DM) Amplifer (see Fig. 2.5) is used. The DM is formed by two digital buffers and the level of the input voltages w.r.t. the buffers voltage tripping points (V_{T}) is analyzed through their four possible logical outputs: $(OUT_+, OUT_-) = (0,0), (1,1), (1,0), (0,1)$.

As detailed in Fig. 2.5, whenever $(OUT_+, OUT_-) = (0,1), (1,0)$, it follows that $v_{\mathrm{d}} > 0$ or $v_{\mathrm{d}} < 0$ respectively, and the logic values of the buffers reflects the sign of th DM signal. From the table within Fig. 2.5, it can be seen that this happens when $|v_{\mathrm{d}}/2| > |v_{\mathrm{CM}} - V_{\mathrm{T}}|$. This is the moment that it can be claimed that the CM signal is negligible and the output can be driven according to the DM signal. To do that, the output stage is added as shown in Fig. 2.6. The latter is activated and V_{out} is increased/decreased depending on v_{d}, i.e., according to the codes $(OUT_+, OUT_-) = (0,1), (1,0)$. Otherwise, when $(OUT_+, OUT_-) = (0,0), (1,1)$, the output node is configured to be in high-impedance

Figure 2.3: ULV OTA state-of-art comparison plots: V_{DD} (mV) versus $FOM_S = 100\frac{GBWC_L}{I_{DD}}$ (V^{-1}), C_L (pF) versus Power (nW) and Area (mm^2) versus Power (nW). (a) Gate-driven, (b) Bulk-driven, (c)(d) Inverter-based from the Fig. 2.1, (e) VCO-based and (f) Digital-based from the Fig. 2.2.

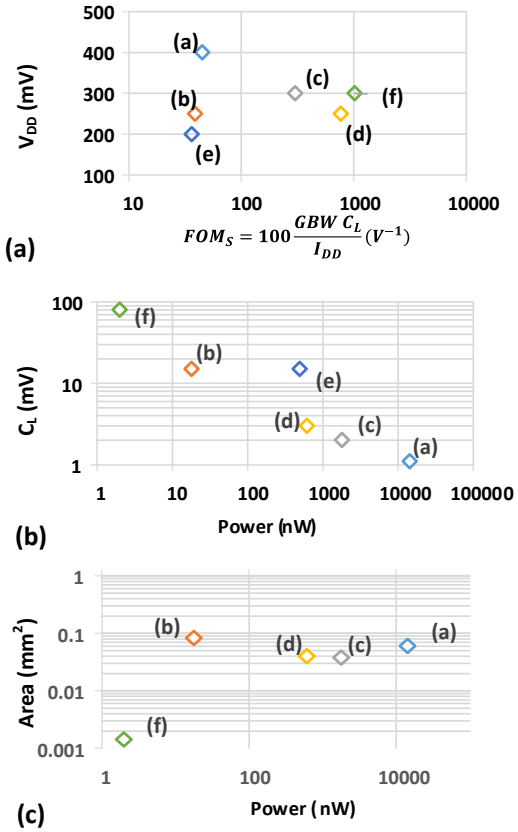

configuration. The Boolean expressions (2.2) and (2.3) show the logic to implement that.

$$\mathrm{P_{OUT}} = \overline{\mathrm{OUT_+}\overline{\mathrm{OUT_-}}} = \overline{\mathrm{OUT_+}} + \mathrm{OUT_-} \tag{2.2}$$

$$\mathrm{N_{OUT}} = \mathrm{OUT_-}\overline{\mathrm{OUT_+}} = \overline{\overline{\mathrm{OUT_-}} + \mathrm{OUT_+}} \tag{2.3}$$

Look that from buffer input to the gate voltages of three-state buffer it is needed to wait a delay of t_D to updade V_out.

For $(OUT_+, OUT_-) = (0,0), (1,1)$, i.e., $|v_\mathrm{d}/2| < |v_\mathrm{CM} - V_\mathrm{T}|$, an auxiliary circuit is needed to track and subtract the common mode from the buffer inputs. Using (OUT_+, OUT_-) as common mode sensing, a CM Extractor is deployed on the loop along with a summing network to correct the input CM signal, as shown in Fig. 2.7. In this

Figure 2.4: Traditional gate-driven NMOS differential pair.

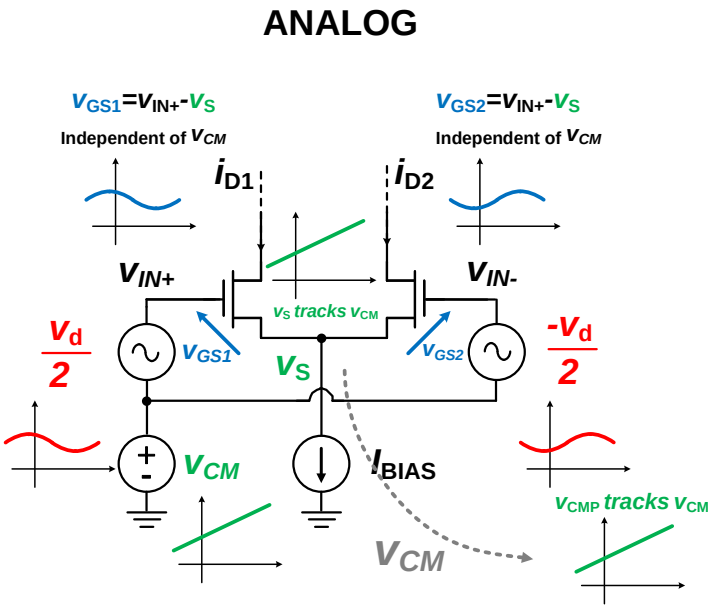

Figure 2.5: Differential Mode Amplifier.

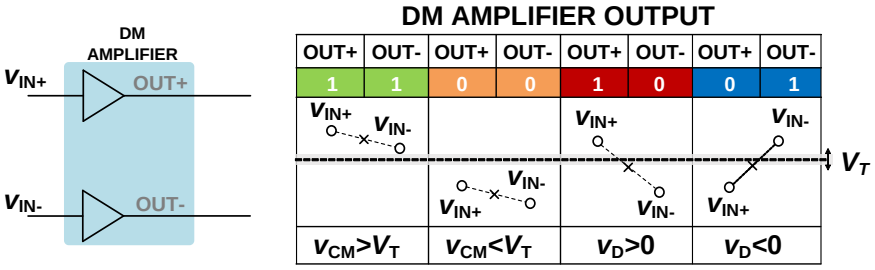

case, the logic implemented to do that is given by

$$\mathrm{P_{CMP}} = \mathrm{OUT_+} + \mathrm{OUT_-} \tag{2.4}$$

$$\mathrm{N_{CMP}} = \mathrm{OUT_+OUT_-} \tag{2.5}$$

The CM Extractor includes its own logic, from Eqs. (2.4) and (2.5), a three state buffer, and a common mode capacitor C_{CM}. Concerning the summing network, a voltage divider made by resistors is adopted. Similar delay of t_{D} is needed to update V_{CMP} from buffer inputs.

Fig.2.8 depicts the first version of DB-OTA proposed by Crovetti in 2013 (Crovetti, 2013). In summary, DB-OTA has four parts: summing network, DM Amplifier, CM Extractor and Output stage. The DM signal flows from summing network, passing through the DM Amplifier, until the output stage, while CM signal flows from summing network,

Figure 2.6: Differential Mode Amplifier and Output stage.

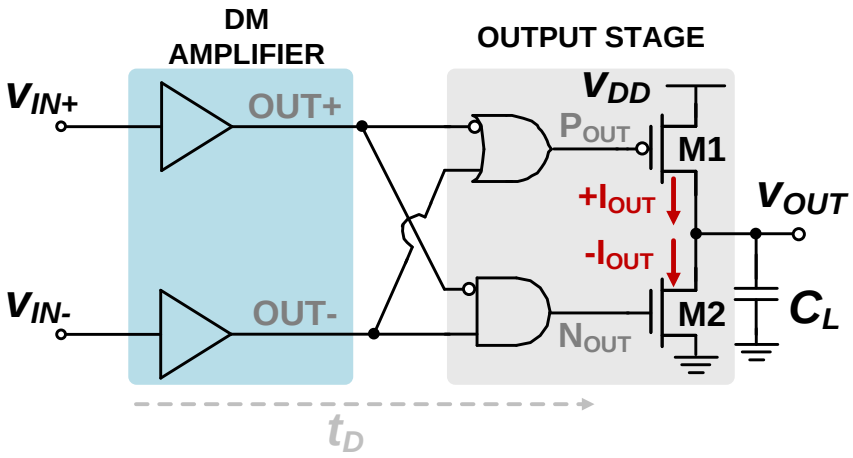

Figure 2.7: Differential Mode Amplifier and Common Mode Extractor.

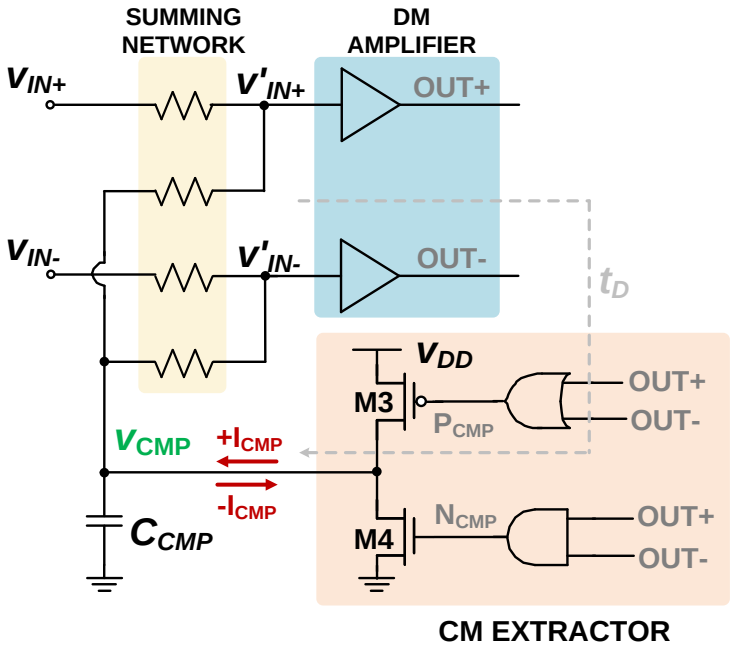

passing through the DM Amplifier, until the CM Extractor.

2.2.2 Quantitative Circuit Analysis

To analyze the DB-OTA operation and its performance, it is crucial to look into its internal waveforms. For equal resistance values within summing network and using the

Figure 2.8: Digital-Based Operational Trasnconductance Amplifier.

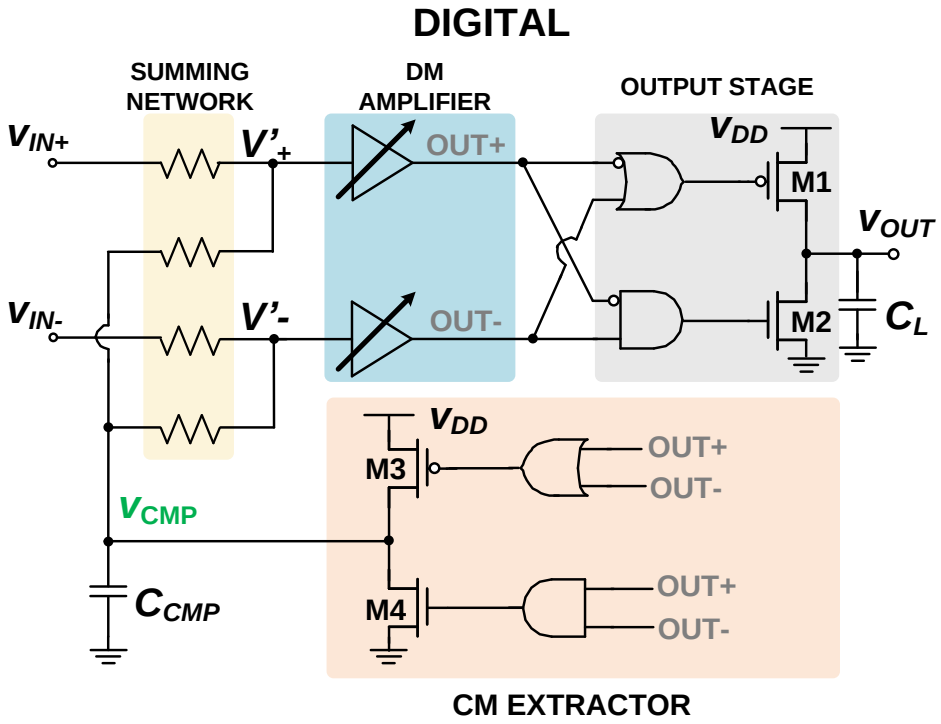

superposition theorem of linear circuits, the voltage seen at each buffer input is given by

$$V'_{IN+}(t) = \frac{R}{R+R}(v_{CMP}(t) + V_{IN+}(t)) = \frac{v_{CMP}(t) + V_{IN+}(t)}{2} \tag{2.6}$$

$$V'_{IN-}(t) = \frac{R}{R+R}(v_{CMP}(t) + V_{IN-}(t)) = \frac{v_{CMP}(t) + V_{IN-}(t)}{2} \tag{2.7}$$

where R is the each resistance within the summing network, $v_{CMP}(t)$ is voltage node that is used to track CM mode input signal (similar role done by V_S) and, $V'_{IN+(-)}(t)$ are the voltages at buffers input. $v_{CMP}(t)$ can be estimated assuming that the three-state buffer in the *CM extractor* pushes and pulls charge by ideal current sources, giving

$$\frac{dv_{CMP}(t)}{dt} = \pm\frac{I_{CMP}}{C_{CMP}} \quad \therefore \quad v_{CMP}(t) = \pm\frac{I_{CMP}}{C_{CMP}}t \tag{2.8}$$

Substituting (2.8) in (2.6) and (2.7), then

$$V'_{IN+(-)}(t) = \frac{1}{2}\left(\pm\frac{I_{CMP}}{C_{CMP}}t + V_{IN+(-)}(t)\right) \tag{2.9}$$

Figure 2.9: a) DB-OTA state transition graph under only CM mode signal stimulus ($v_d = 0$) b) time-domain DB-OTA waveforms

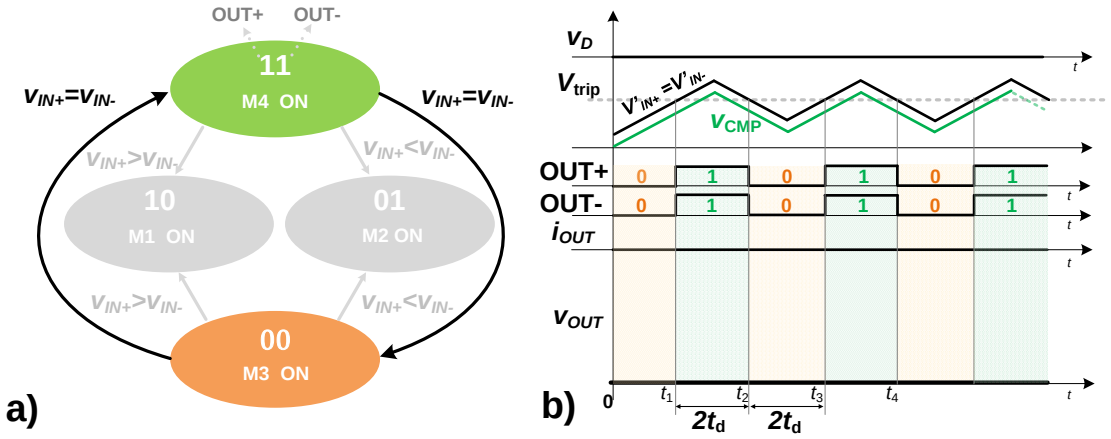

If a fixed DC CM signal is applied, i.e., $V_{IN+}(t) = V_{IN-}(t)$, then, due to the feedback logic inside of *CM extractor*, $V'_{IN+(-)}(t)$ oscillates around the buffer trip points V_T with a period

$$T_0 = \frac{1}{f_0} = 4t_{\mathrm{D}} \tag{2.10}$$

where f_0 is the internal natural oscillation frequency of the DB-OTA.

Fig. 2.9a shows the DB-OTA state transition graph under a pure CM signal stimulus, i.e., $v_d = 0$. Note that the circuit does not have a static bias point; Instead, it tracks the CM signal, oscillating around the V_T of the buffer. In contrast, when the circuit is differential input stimulated, it means that $|v_{\mathrm{d}}/2| < |v_{\mathrm{CM}} - V_{\mathrm{T}}|$ holds. This mechanism can be thought of as a kind of dynamic bias point. This eliminates the need of a constant bias current, hence lowering the total power consumption. Fig. 2.9b draws the waveforms of the main node voltages within the DB-OTA, when modeled by a first order approach.

When $v_d(t) = V_{IN+}(t) - V_{IN-}(t) \neq 0$, two more states appear in DB-OTA state transition graph as shown in Fig. 2.10a. From Eq. (2.9), for $V'_{IN+(-)}(t) = V_T$ which makes $V'_{IN+}(t) - V'_{IN-}(t) = 0$, the $\Delta t(t)$ due to v_d can be estimated by

$$0 = \frac{I_{CMP}}{C_{CMP}}\Delta t(t) - v_d(t) \quad \therefore \quad \Delta t(t) = \frac{C_{CMP}}{I_{CMP}}v_d(t) \tag{2.11}$$

Applying the Laplace transform in Eq. (2.11), then

$$\Delta T(s) = \frac{C_{CMP}}{I_{CMP}} \cdot V_d(s) \tag{2.12}$$

Since zero crossings occur every half period, the voltage-to-time conversion takes

Figure 2.10: a) Complete DB-OTA state transition graph b) time-domain DB-OTA waveforms

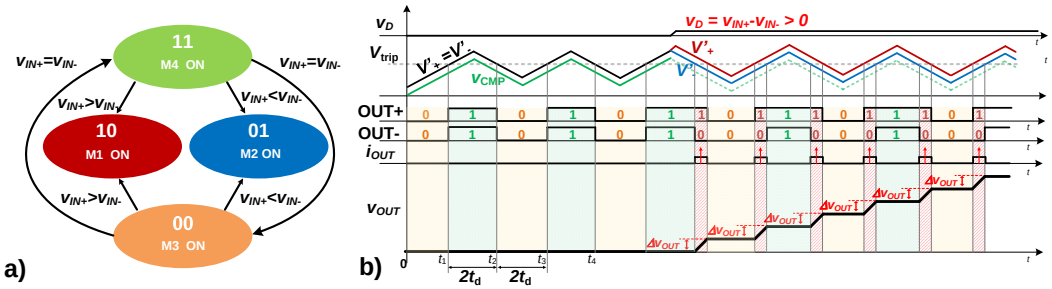

place every $T_0/2$ and leads to the generation of a signed time difference $\Delta t(t)$ given by Eq. (2.11), and its width is proportional to v_d evaluated at $kT_0/2$. Hence, the internal DB-OTA loop acts as a self-oscillating threshold sampler (HERNANDEZ; PREFASI, 2008) with a natural sampling frequency of $2f_0$. Based on that, the three-state buffer of the *output stage* receives such pulses $\Delta t(t)$ every pushing/pulling current in its output node. Assuming that time pulses $\Delta t(t)$ take place exactly every $T_0/2$, the output stage current $i_{OUT}(t)$ driving C_L can be written as

$$i_{OUT}(t) = \sum_{k=0}^{+\infty} I_{OUT}\Delta t(t)\delta\left(t - \frac{k}{2f_0}\right) = \sum_{k=0}^{+\infty} I_{OUT}\Delta t(t)\delta\left(t - k2t_D\right) \tag{2.13}$$

The Laplace of the Eq. (2.13) for frequencies much lower than f_0 gives

$$I_{OUT}(s) = \frac{I_{OUT}}{2t_D}\Delta T(s) = \frac{I_{OUT}}{2t_D}\frac{C_{CMP}}{2I_{CMP}}V_d(s) \tag{2.14}$$

Since

$$V_{OUT}(s) = \frac{r_{OUT}}{sr_{OUT}C_L + 1}I_{OUT}(s) \tag{2.15}$$

the DB-OTA transfer function can be estimated as

$$A_D(s) = \frac{V_{OUT}(s)}{V_d(s)} = \frac{1}{2}\cdot\frac{I_{OUT}}{2t_D}\frac{C_{CMP}}{I_{CMP}}\frac{r_{OUT}}{(sr_{OUT}C_L + 1)} \tag{2.16}$$

From Eq. (2.16), the low frequency DC gain in dB of the DB-OTA as well as its unit gain bandwidth (GBW) can be calculated as shown by Eq. (2.17) and Eq. (2.18),

respectively.

$$A_{d,dB} = 20\log_{10}\left(\frac{1}{2}\cdot\frac{I_{OUT}r_{OUT}}{2t_D}\frac{C_{CMP}}{I_{CMP}}\right) = -6\text{dB} + 20\log_{10}\left(\frac{I_{OUT}r_{OUT}}{2t_D}\frac{C_{CMP}}{I_{CMP}}\right) \tag{2.17}$$

and

$$f_{GBW} = \frac{f_0}{2\cdot\pi}\cdot\frac{I_{OUT}}{I_{CMP}}\frac{C_{CMP}}{C_L} \tag{2.18}$$

once its dominant pole is given by

$$s_p = -\frac{1}{r_{OUT}C_{\text{L}}} \tag{2.19}$$

The DB-OTA power consumption is the sum of the power consumption of the active power P_{gates} of the logic gates involved in the self-oscillating loop (i.e., ***DM Amplifier*** and ***CM Extractor***), the contribution P_{out} of the output stage, and the overall leakage power P_{lkg}

$$P_{DB-OTA} = P_{gates} + P_{out} + P_{lkg} \approx P_{gates} + P_{out} \tag{2.20}$$

In Eq. (2.20), P_{gates} is given by the dynamic power of the internal logic gates with overall switched capacitance C_{int} operating at frequency $2/T_0$, which can be expressed as

$$P_{gates} = \frac{2}{T_0}C_{int}V_{DD}^2 \tag{2.21}$$

and P_{out} is the power needed to (dis)charge the load capacitance C_L, which can be expressed as

$$P_{out} = f_S C_L V_{OUT}^2 \tag{2.22}$$

where a sinewave output with peak-to-peak amplitude V_{OUT} at frequency f_S is assumed.

From the above quantitative analysis, some points are worthy to be highlighted. Eq. (2.16) shows that the DB-OTA behaves as a first-order system with negative real pole at $1/(2\pi r_{OUT}C_L)$ consuming a total power of

$$P_{DB-OTA} \approx (2C_{int} + \alpha C_L)f_0 V_{DD}^2 \tag{2.23}$$

under rail-to-rail input signal, where $\alpha = \frac{f_S}{f_0}$. In the case that $f_S = f_{GBW}$ from Eq. (2.18)

and consequently

$$\alpha = \frac{I_{OUT} C_{CMP}}{2\pi I_{CMP} C_L} \tag{2.24}$$

then

$$P_{DB-OTA,GBW} \approx C_{DB-OTA,GBW} f_0 V_{DD}^2 \tag{2.25}$$

where $C_{DB-OTA,GBW} = 2C_{int} + \frac{I_{OUT}}{2\pi I_{CMP}} C_{CMP}$. $C_{DB-OTA,GBW}$ is here defined as DB-OTA equivalent capacitance. For the presented DB-OTA, $C_{DB-OTA,GBW} f_0 V_{DD}^2$ power consumption demonstrates that V_{DD} can be used as a design knob to reduce the power consumption as typically adopted in DVS low power digital circuit (WANG et al., 2016). In the next section 2.2.3, low V_{DD} is chosen to reduce the total power consumption targeting low power IoT applications.

Another point is that, based on Eq. (2.16), DB-OTA should have a phase margin (PM) of 90^o in unit gain configuration. However, as it will be shown in section 2.4, simulations results demonstrate PM between 57 and 76 depending on C_L, indicating a relevant non-dominant pole for low values of C_L. The non-dominant pole effect on the PM can be interpreted by the relevant parasitic output capacitance seen from the DM amplifier's total equivalent input capacitor and high values of resistance from the pseudo-resistor working in weak inversion. Furthermore, for low frequencies, DB-OTA has an intrinsic gain loss of -6 dB as shown in (2.17), due to the voltage divider of the summing network as seen in (2.6) and (2.7). Indeed, the summing network of the DB-OTA is the root of the above limitations, and it will be replaced by a different input stage in the chapter 3, providing a new digital-based OTA.

2.2.3 Circuit Design

The proposed ULV DB-OTA has been designed in 180nm following digital design criteria. CMOS static logic is adopted for most the gates in Fig.2.8. Moreover, as usual in ULP digital design, the power supply voltage is set to the Minimum Energy Point (MEP) (Pinckney; Blaauw; Sylvester, 2015), which turns out to be about $V_{\mathrm{DD}} = 300\mathrm{mV}$ for the target technology and switching activity (f_0).

The strength of the output stage is set by considering the maximum capacitive load (80pF in the proposed design) and slew rate requirements, taking into account also that a

Figure 2.11: a) inverter-based pseudo-resistor b) Static digital calibration (SDC) and dynamic digital calibration (DDC).

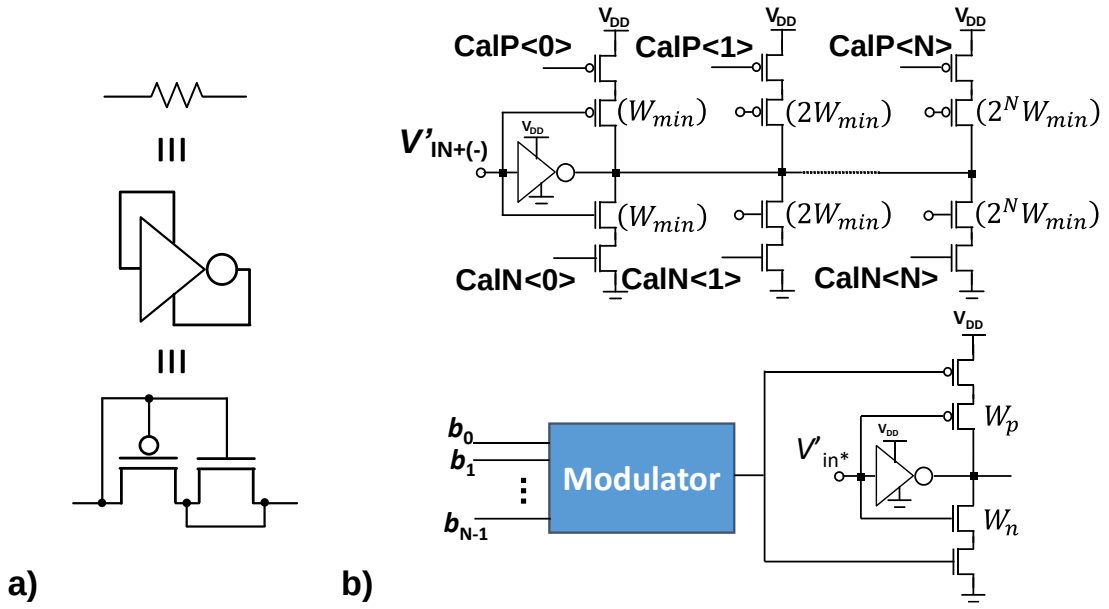

minimum capacitive load (10pF in the proposed design) is needed in the DB-OTA for low-distortion analog signal reconstruction. The strength of the other gates is consequently designed as cascaded drivers to guarantee digital signal integrity. Minimum-size devices have been used in the CM extractor stage, and the capacitance C_{CMP} has been set to reduce Total Harmonic Distortion (THD), supported by the analysis of the simulation results.

Two parts of the circuit deserve a special care due to their analog function, i.e. the summing network and the first inverters of the DM amplifier.

The summing network has been implemented using inverter-based pseudo-resistors as voltage dividers. Large area ($\approx 270\mu m^2$) has been adopted in PMOS devices in Fig. 2.11a, to achieve a good matching leveraging Pelgrom's law (GALUP-MONTORO et al., 2005b).

For what concerns the DM amplifier in Fig. 2.8, mismatch in the buffers V_{T} decides the DB-OTA input offset voltage and it has been mitigated by the calibration network as the ones shown in Fig. 2.11b. Eq. (2.26) shows the voltage offset of DB-OTA.

$$V_{\mathrm{OFF}} \approx \Delta V_{\mathrm{T}} \tag{2.26}$$

where

$$\Delta V_{\mathrm{T}} = V_{\mathrm{T1}} - V_{\mathrm{T2}} \tag{2.27}$$

is the difference of the trip points V_{T1} and V_{T2} of the first inverters of each buffer, both

expressed in terms of technology and geometrical parameters in subthreshold regime as (BRAGA et al., 2019):

$$V_{\mathrm{T}} = \frac{\frac{\kappa T}{q}\log\left(\frac{I_{\mathrm{D0_P}}\left(\frac{W}{L}\right)_{\mathrm{P}}}{I_{\mathrm{D0_N}}\left(\frac{W}{L}\right)_{\mathrm{N}}}\right) + \frac{V_{\mathrm{DD}}}{n_{\mathrm{P}}}}{\frac{1}{n_{\mathrm{P}}} + \frac{1}{n_{\mathrm{N}}}}, \tag{2.28}$$

$I_{\mathrm{D0_{N(P)}}}$ is the zero-v_{GS} drain current of nMOS (pMOS) in weak inversion and it is process parameter dependent, $n_{N(P)}$ is the subthreshold slope factor of the nMOS (pMOS) device. All the other symbols have their usual meaning (BRAGA et al., 2019).

For minimum size devices, the offset predicted by (2.26) can be easily large enough to saturate the DB-OTA, thus fully impairing the DB-OTA operation, and needs to be compensated. For this purpose, the dependence of the trip points of a CMOS inverter on the aspect ratios of the pull-up and pull-down devices, given by Eq. (2.28), can be used for calibration.

In this implementation, two methods have been adopted in the DB-OTA calibration: Static Digital Calibration (SDC) and Dynamic Digital Calibration (DDC).

The SDC (see Fig. 2.11b top) procedure has been applied in (Toledo et al., 2019), which has made the calibration possible tuning the effective aspect ratio of either the pull-up or the pull-down branch by enabling/disabling binary weighted $2^i W_{min}$ transistors in parallel to first inverter of the DM amplifier, based on a 8-bit calibration code $b_{i,n}$ with $i = 0...N-1$. This calibration procedure, however, is not compatible with a pure digital flow and requires extra area and analog design effort.

Given these limitations, all-Digital DDC techniques based on Digital Pulse Width Modulation (DPWM) and Dyadic Digital Pulse Modulation (DDPM) have been explored in (TOLEDO; AIELLO; CROVETTI, 2019) and (Toledo et al., 2020), respectively.A DDC network, which consists of only one enabled-inverter driven by the input signals ($V_{in-(+)}$) and also connected in parallel to the first stage of each branch in the DM amplifier, is depicted in Fig. 2.11b bottom. A modulator applying a particular modulation technique is then connected to the DDC network to modulate the input signal adjusting the DM amplifier V_T.

The calibration network operation is described next. The pull-up (pull-down) network of the calibration inverter can be connected to the supply (to ground) through a pMOS (nMOS) power gating switch. When the pMOS (nMOS) gating switch is on, the pMOS (nMOS) of the calibration inverter, with width W_n (W_p) is enabled and connected in parallel to the nMOS (pMOS) device in the first stage of the DM amplifier, thus effec-

Figure 2.12: a) DB-OTA layout. Total area of 1,426 μm^2 b) Micrograph of the 180-nm test-chip.

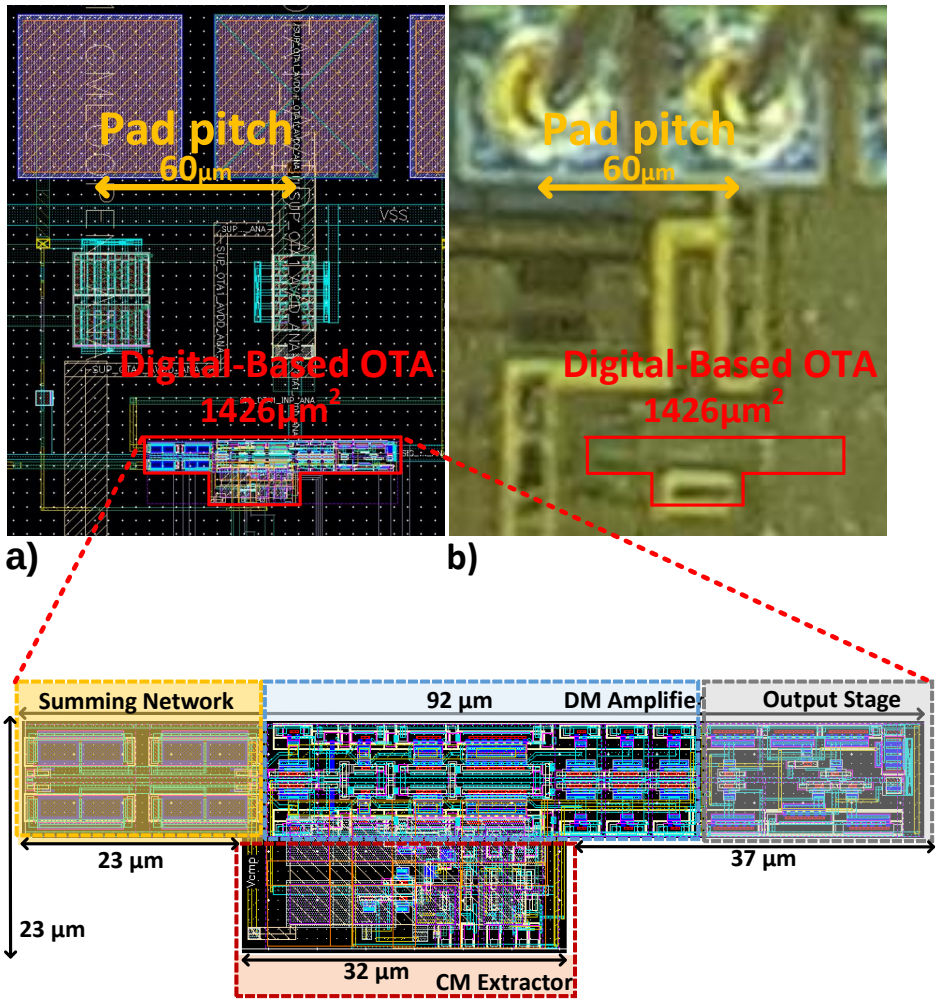

tively increasing its width and significantly reducing (increasing) its trip point according to Eq. (2.28).

When the gating switches are periodically operated with a certain frequency larger than the DB-OTA GBW, it is observed that periodically enabling the gating switches has the same net effect on the trip points of the DM amplifier gates as increasing the width of the DM amplifier devices by a fraction DW_n (DW_p) of the calibration inverter width W_n (W_p), being $D = \frac{T_{\text{EN}}}{T}$ the effective enabling duty cycle, where T_{EN} is the overall time the calibration inverter is enabled over the period T. This approach is adopted for dynamic offset calibration of the OTA, considering both DPWM and DDPM streams as gating signals for the calibration inverter. Results for all calibration strategies will be shown in section 2.4.

Figure 2.13: DB-OTA Area Breakdown not containing the DDC; only SDC.

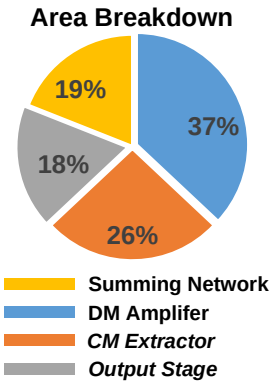

2.3 Layout

The DB-OTA has been laid out in 180nm CMOS to match the delays of the non-inverting and inverting signal paths. Logic gates from the standard cell library have been placed, reducing the layout design effort. The layout of the circuit, including the calibration network, occupies just 1,426 $\mu\mathrm{m}^2$, and it is shown in Fig. 2.12a. Its area breakdown is depicted in Fig. 2.13. 37% of the area is occupied by the DM Amplifier which contains the SDC network.

The ULV DB-OTA operation and performance have been evaluated by post-layout simulations (Toledo et al., 2019; Toledo et al., 2020) and tested by measurements (TOLEDO et al., 2021). Fig 2.12b shows a microphotograph of the 180nm test-chip. In the sections 2.4 and 2.5, all simulations and measurements results are plotted and compared with ULV OTAs presented in recent literature, respectively.

2.4 Simulations Results

The ULV DB-OTA input and output waveforms with a sine wave input at 30 Hz frequency, 50mV peak amplitude and $C_\mathrm{L} = 80\,\mathrm{pF}$ are reported in Fig. 2.14b for $V_\mathrm{DD} = 300\mathrm{mV}$ and in voltage follower configuration. In this configuration, a THD less than 2% and 2 nW power consumption are achieved. Also in this picture, a zoom in the output voltage waveform reveals the step-wise changes in v_out; the intrinsic digital characteristic of the DB-OTA (see Fig. 2.10b). The ULV DB-OTA frequency response, calculated through Fast Fourier Transform (FFT) analysis of transient simulations, as done in (Toledo et al., 2019), is reported in Figure 2.14d for $C_\mathrm{L} = 10, 45, 80$ pF. Note that no quiescent

Figure 2.14: [SIMULATION]a) DB-OTA layout and Area breakdown containing DDC b) V_{in} and V_{out} at 30 Hz frequency, 50 mV peak amplitude and $C_{\text{out}} = 80\,\text{pF}$ c) Power breakdown d) ULV DB-OTA frequency response (Toledo et al., 2020).

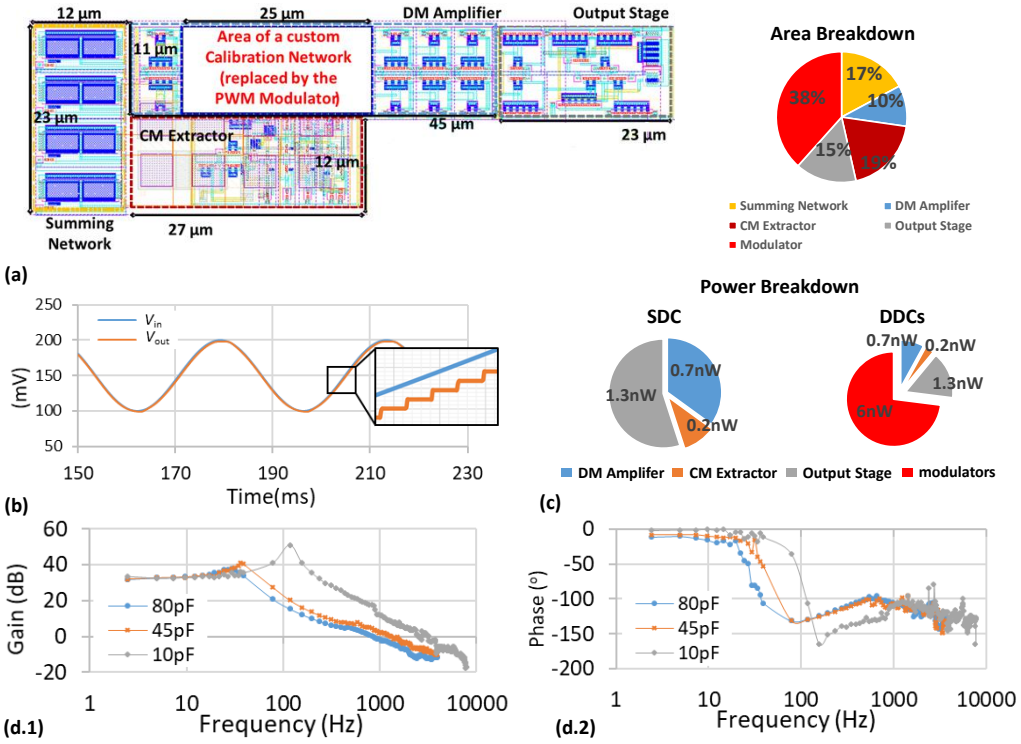

bias is available, impairing any AC analysis. According to that, DB-OTA shows 35dB DC gain and 0.85, 1.3 and $2.48\,\text{kHz}$ Gain Bandwidth Product (GBW) with phase margins $76°, 68.5°$ and $57°$, respectively.

In the same voltage follower configuration, the DB-OTA without calibration has been verified under process variations for $V_{\text{amp}} = 50\,\text{mV}$, $C_{\text{L}} = 80\,\text{pF}$ and $f_{\text{in}} = 30\,\text{Hz}$ by Montecarlo (MC) simulations on 100 samples. Figure 2.15a shows the V_{in} and V_{out} of a bad sample from this analysis. Mainly due to the mismatch of the DM amplifier first inverter as highlighted before, the output signal of this sample is pushed towards V_{DD} distorting the signal and increasing the offset voltage.

To have a fully insight about this issue, a thumbnail plot between THD (%) and Voltage offset for 100 samples, in which each point is a sample of the MC, is depicted in Figure 2.15b. Pearson's coefficient is applied for the same uncalibrated samples, resulting in 40% of correlation between THD and offset; i.e., if the offset is attenuated, the THD is also improved. The SDC and DDC are used though to tweak the offset of the DB-OTA as shown Figure 2.15c; in this case, the DPWM modulator was chosen.

Both for SDC and DDC, each sample has been recovered by adequately choosing a 3-bit calibration code (to be applied as an input decoder enabling the calibration network

Figure 2.15: [SIMULATION] a) V_{in} and V_{out} of a bad sample from the MC analysis with 30 Hz frequency, 50 mV peak amplitude and $C_{\text{out}} = 80\,\text{pF}$ b) Thumbnail plot between THD (%) and input offset voltage (mV)—each point is a sampe of the MC simulation c) Changing the BD-OTA offset through DDC using the DPWM modulator d) Trade-off between power and signal integrity (THD) versus T (Toledo et al., 2020).

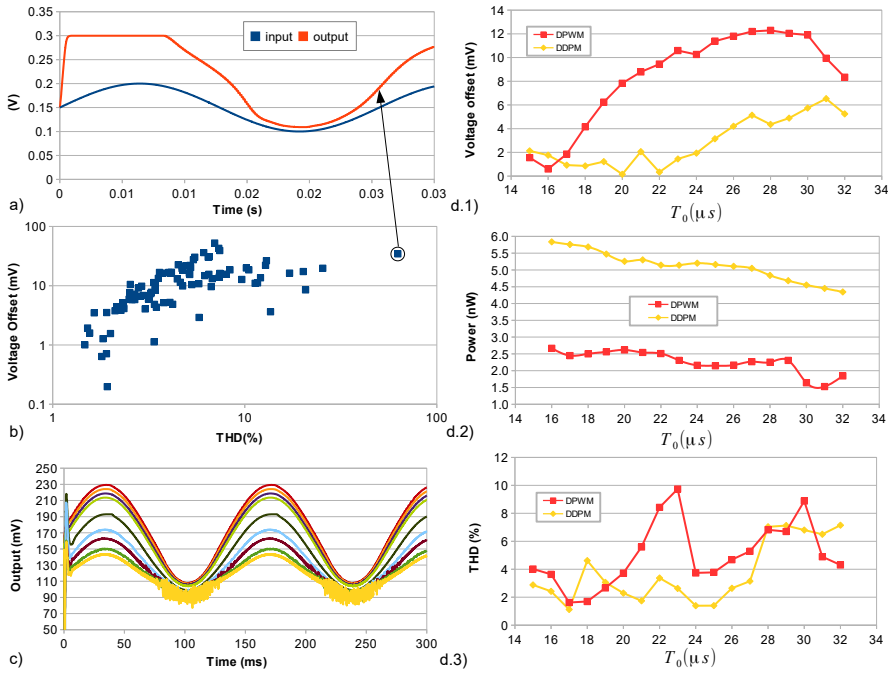

in SDC and as the DPWM/DDPM modulators input words for DDC) so that to minimize the simulated input offset voltage. Calibration signals applied just to the non-inverting input branch have been considered to reduce power and area overhead.

In Fig. 2.15d, the calibrated DB-OTA input offset voltage, power (DB-OTA alone), and THD are plotted for one representative sample versus the period T of DDPM and DPWM calibration patterns applied to the enabling transistors in Fig. 2.11b, revealing that improved offset and THD (both slightly better for DDPM compared to DPWM) can be achieved at lower T at the cost of increased power consumption, which is more relevant for DDPM. An extra power overhead of around 6nW and silicon area of 25 μm $\times$ 25 μm should also be taken into account for DPWM, and DDPM modulators (TOLEDO; AIELLO; CROVETTI, 2019).

Trading off power and accuracy, a different period $T = 24$ μs for DPWM and 32 μs for DDPM have been considered as an optimal choice for the two DDC strategies.

To make a fair comparison over different samples, SDC and DDCs have been considered to trim a population of 100 samples keeping the same seed for random number generation in the MC simulations used in Figure 2.15b. Optimal 3-bit calibration words leading to minimum input offset voltage have been first identified for each sample for

Figure 2.16: [SIMULATION] a) Voltage offset b) THD c) Power d) GBW e) and $FOM_S = 100\frac{GBWC_{Load}}{I_{\mathrm{DD}}}$ histograms (Toledo et al., 2020) .

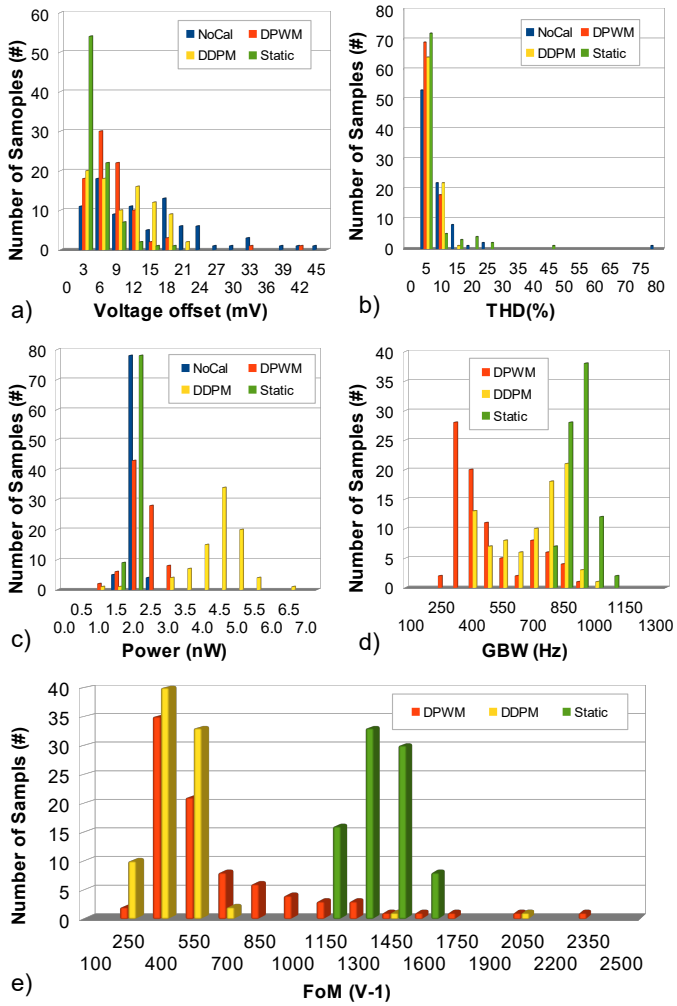

SDC, and both the DPWM and the DDPM DDC techniques. Then, such optimal calibration words have been applied in simulations to compare the performance statistics of the calibrated samples.

The histogram of the DB-OTA input offset voltage is reported in Figure 2.16a before and after calibration. Without calibration (blue bars), the mean (μ) and standard deviation (σ) are 12.26 mV and 9.29 mV, respectively. Using the SDC (green bars), $\mu = 3.15$ mV and $\sigma = 2.9$ mV have been achieved. While, for the DPWM (red bars) and DDPM (yellow bars), (μ, σ) are (6.86,5.8) mV and (8.19,5.34) mV, respectively. Figures 2.16b–e show the histograms for the THD, Power, GBW and FOM_S.

Table 2.1 lists the mean and the standard deviation (μ, σ) for each performance before and after the static and dynamic calibrations. The DDC shows an average offset reduction of $\times$1.79 for DPWM and $\times$1.5 for DDPM modulation, increasing the THD yield by $\times$1.3 and $\times$1.2, respectively, for 5% THD as threshold.

Table 2.1: Monte Carlo simulation results: statistics parameters.

Peformance	No calibration	Static	DPWM	DDPM
Offset Voltage (mV)	$\mu = 12.26, \sigma = 9.29$	$\mu = 3.15, \sigma = 2.9$	$\mu = 6.86, \sigma = 5.8$	$\mu = 8.19, \sigma = 5.34$
THD (%)	$\mu = 6.17, \sigma = 8.65$	$\mu = 4.6, \sigma = 6.18$	$\mu = 3.61, \sigma = 1.82$	$\mu = 4.16, \sigma = 2.04$
Power (nW)	$\mu = 1.73, \sigma = 0.15$	$\mu = 1.65, \sigma = 0.13$	$\mu = 1.95, \sigma = 0.41$	$\mu = 4.12, \sigma = 0.78$
GBW (nW)	-	$\mu = 865.9, \sigma = 63.3$	$\mu = 434.4, \sigma = 174.28$	$\mu = 643.99, \sigma = 166.65$
FoM (V^{-1})	-	$\mu = 1269.5, \sigma = 127.7$	$\mu = 592.11, \sigma = 385.17$	$\mu = 402.13, \sigma = 227.21$

DDCs are more compatible with a pure digital flow, and they can be easily implemented into the digital part of IoT systems such as the general one in Figure 1.4. However, the power and area overhead intrinsically linked to the dynamical calibration does not bring better results than the SDC (i.e., lower spread over MC analysis). Consequently, in the following section 2.5 regarding measurements, just SDC is reported.

2.5 Measurements Results

The DB-OTA's measured input and output waveforms are reported in Fig. 2.17a for sample #3, which exhibits the most pronounced non-linearity and hence the highest THD. In this figure, the measurements are taken at a supply voltage of V_{DD}=300mV under a 3-Hz input sine wave with 50-mV amplitude and a significant capacitive load of C_L=80pF. The measurements in Fig. 2.17 reveal that a THD of 1.26% and power consumption of 591 pW are achieved under the above conditions. For the same die, the input offset voltage was measured to be 1.1 mV and the root mean square (r.m.s.) input noise integrated over the 500 Hz input bandwidth is 2.9 mV.

DB-OTA is the first OTA operating in a sub-nW power regime to the best of this thesis author's knowledge. Fig. 2.18a shows the power breakdown among the DB-OTA sub-blocks, in which the most significant contribution is associated with the output stage (55%) followed by the DM amplifier (35%). In contrast, the CM extractor is expected to consume less due to the small size of transistors and capacitor.

The slew rate was evaluated from the response to a square wave input, as shown in in Fig. 2.17b. In particular, for the same input amplitude and load considered above, a positive slew rate (SR_+) of 0.278 V/ms and a negative (SR_-) of 0.25 V/ms were measured.

Fig. 2.19a compares the measured THD to the simulation results in section 2.4. The measured common-mode input range of DB-OTA was found to be lower than 100 mV in the measured samples. The mismatch mainly induces the increased distortion at higher input amplitudes in the input inverters due to their operation in the sub-threshold

Figure 2.17: [MEASUREMENTS] a) V_{IN} and V_{OUT} sine waves for C_L=80pF, input amplitude V_{amp}=50mV and frequency f_{in}=3Hz, b) transient response for a square wave input, C_L=80pF, V_{amp}=50mV and f_{in}= 50Hz. The settling time measured at the rising (falling) edge is 1.15 (0.9) ms.

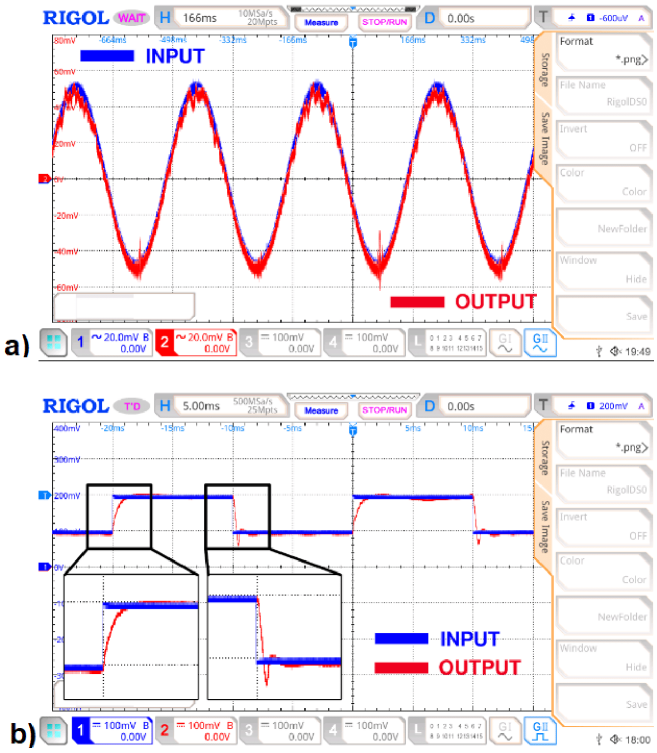

region. Such dominant mismatch contribution ultimately gives rise to a reduction in the input swing even after calibration.

The DB-GOTA was tested in the closed-loop voltage follower configuration with 50-mV amplitude sine wave input at different frequencies f. The differential voltage gain frequency response was measured in magnitude and phase by taking the ratio of the Fast Fourier Transform (FFT) at each f of the output, and the differential input voltage. The DB-OTA frequency response of the measured samples is reported in Figs. 2.19b,c, and exhibits a 29dB DC gain in the considered sample #3, whereas all other samples have larger DC gain up to 31 dB. Also, a Gain Bandwidth Product GBW of 518 Hz was measured, along with a phase margin of 57.3^o (51.4^o-57.3^o over the three dice). The highest measured GBW of 518 Hz across dice is 200 Hz and is below the minimum value presented in previous subsection based on Monte Carlo simulations over 100 runs, which showed a μ_{GBW} =865Hz and σ_{GBW}=63 Hz. The self-oscillation frequency was measured to be 10 kHz (f_0).

The power consumption for a 3-Hz sine wave input with 50-mV amplitude under C_L=80pF was found to be 590 pW, and always lower than 1 nW across all samples (from

Figure 2.18: [MEASUREMENTS] a) Power and b) Area breakdown

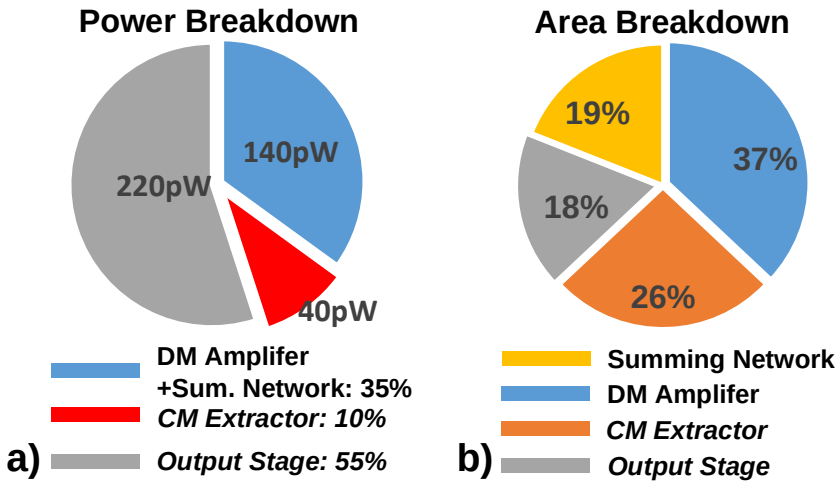

Table 2.2: PERFORMANCE COMPARISON WITH THE STATE OF THE ART **(BEST PERFORMANCE IN BOLD)**

Performance	**DB-OTA+**		[1]+	[2]+	[3]+	[4]+	[5]* MC-OTA	[5]* FFC-OTA	**DIGOTA+**
	Min	Max							
Architecture	**Digital**		Bulk-driven	Bulk-driven	Bulk-driven	Bulk-driven	Inverter-based	Inverter-based	**Digital**
technology	180		130	65	180	350	130	130	180
V_{DD} [V]	0.3		**0.25**	**0.25**	0.5	0.6	0.3	0.3	0.3
C_{LOAD}[pF]	80		15	15	20	15	2	2	**150**
area [μm^2]	1,426		83,000	2,000	26,000	60,000	-	-	**982**
DC Gain [dB]	31	29	60	**70**	52	69	46.2	49.8	30
GBW [kHz]	0.229	0.518	1.88	9.5	1,200	11.4	2,450	**9,100**	0.25
Slew Rate [V/ms]	0.097	0.264	0.7	0.2	2,890	14.6	2,400	**3,800**	0.085
THD [%]	1.26++	2.82++	**0.2**	-	1	0.08	-	-	2
Phase Margin [°]	51.4	57.3	52.5	89.5	-	65	57	76	90
Power [nW]	**0.407++**	0.591++	18	26	110,000	550	1,800	1,800	2.4
FOMS [V^{-1}]	1352	**2,101**	29	137	0.11	0.18	81	303	468
FOML [-]	573	**1,071**	14.6	3	22.27	23.9	80	140	159

[1] (Ferreira; Sonkusale, 2014)+, [2] (WOO; YANG, 2020)+, [3] (Chatterjee; Tsividis; Kinget, 2005)+, [4] (FERREIRA; PIMENTA; MORENO, 2007)+, [5](Lv et al., 2019)
+Experimental, *Simulation

407 pW to 697 pW).

The usual small-signal figure of merit in Eq. (2.29) was adopted to evaluate the power efficiency at small inputs:

$$FOM_S = 100\frac{GBW \cdot C_L}{I_{DD}} \tag{2.29}$$

where $I_{DD} = power/V_{DD}$, evaluates to 2,101 V^{-1} (from 1,352 to 2,101 V^{-1} across the three dice). Analogously, the usual large-signal figure of merit in Eq. (2.30) was evaluated to quantify the power efficiency at large inputs:

$$FOM_L = 100\frac{SR \cdot C_L}{I_{DD}} \tag{2.30}$$

where SR is the average between SR_+ and SR_-. The figures of merit in Eq. (2.30) evaluates to 1,071 (from 468 to 1071 across the three dice). Both figures of merit reveal a highly-efficient operation of the DB-OTA circuit, as discussed before.

Figure 2.19: [MEASUREMENTS] a) THD (%) versus peak Vamp for 3Hz frequency b,c) ULV DIGOTA frequency response

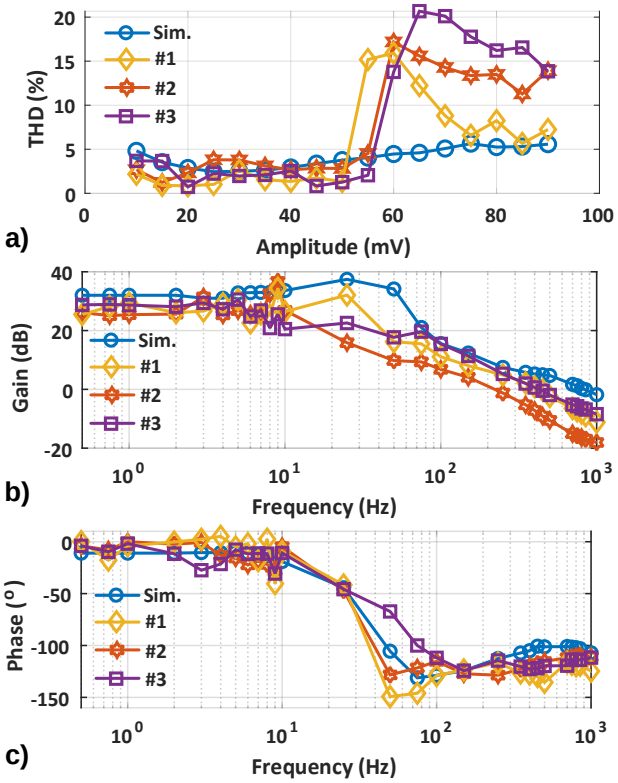

Figure 2.20: [MEASUREMENTS and SIMULATION] . State-of-art of ultra-low voltage OTAs. #1,#2 and #3 are the three die samples measured in this work. The remaining points within the cloud are results from the Monte Carlo simulation from (Toledo et al., 2019).

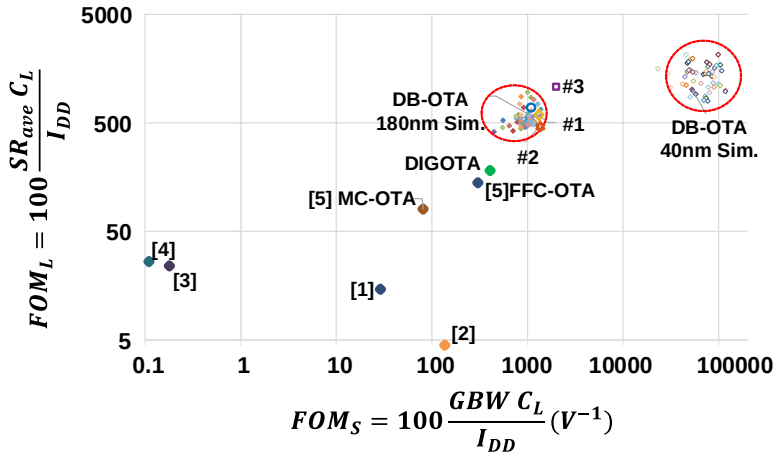

Compared to prior OTAs proposed in the recent literature in Table 2.2, the DB-OTA drives the second largest output capacitance $C_L = 80\text{pF}$ at the lowest power consumption. In detail, the DB-OTA power is 4X lower than DIGOTA (see the next subsection), in spite of the area penalty of the calibration network and the pseudo-resistors, and a more pronounced distortion. Interestingly, the proposed DB-OTA is the most power-efficient OTA reported to date, and in particular has a 4.5X improved FOM_S metric compared to the DIGOTA. The comparison in terms of both FOM_S and FOM_L is also illustrated in Fig. 2.20, which shows the power efficiency improvement enabled by DB-OTA over prior art. As done in (Toledo et al., 2019), the results of preliminary transistor-level simulations performed on the circuit ported to 40nm CMOS are also shown in Fig. 2.20, demonstrating the potential benefits brought by technology scaling, based on the digital nature of DB-OTA compared to traditional analog OTAs.

3 DIGOTA

This chapter presents a passive-less fully-digital operational transconductance amplifier (DIGOTA) for energy- and area-constrained systems. What differentiates the new DIGOTA from previously presented DB-OTA (chapter 2) is that the former has passive-less self-oscillating common-mode compensation, making the circuit less noisy, more robust to mismatch variations, and more compatible with the digital flow. The chapter organization follows the same structure of the previous one: circuit analysis and design in section 3.1, its layout description in section 3.2, simulation in section 3.3, and measurements in section 3.4.

Figure 3.1: DIGOTA schematic

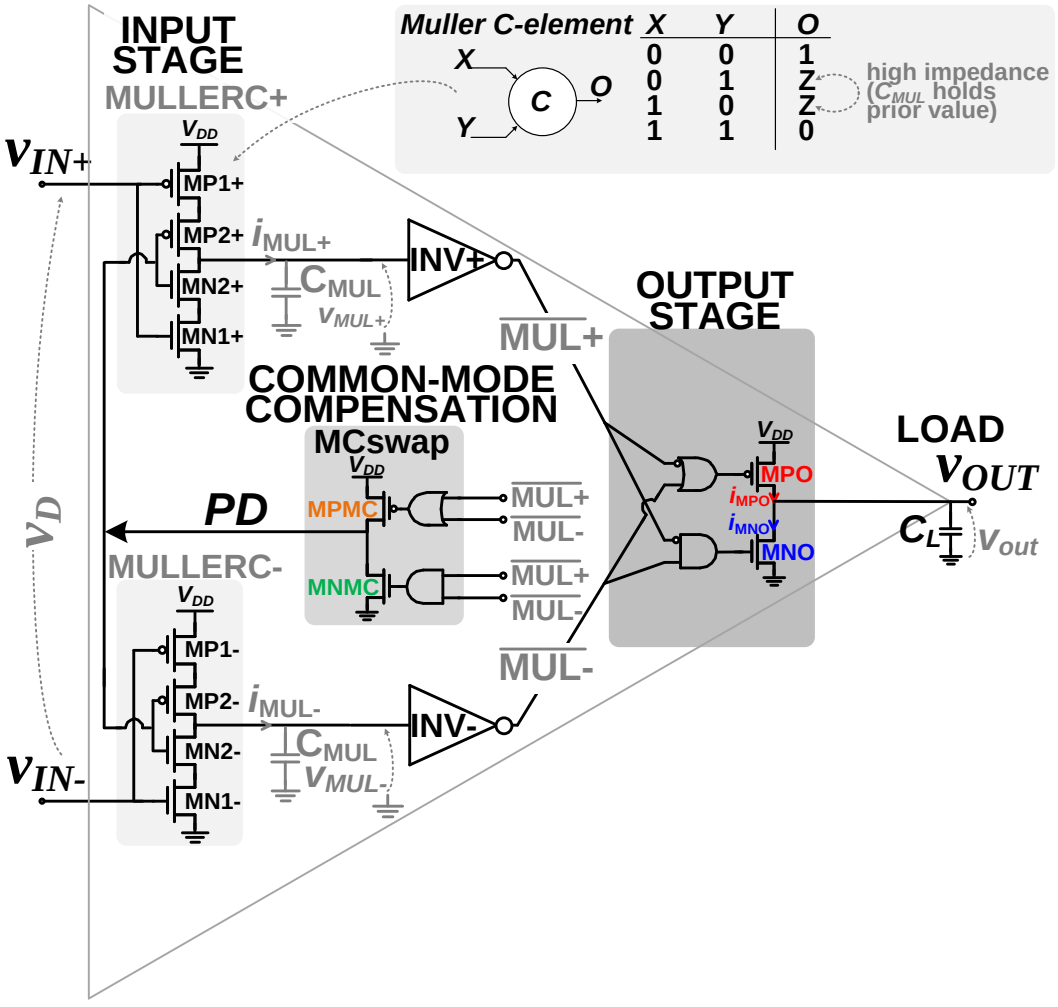

3.1 Circuit Analysis and Design

As any other OTA, DIGOTAs amplify the differential input $v_D = v_{IN+} - v_{IN-}$, while rejecting the common-mode component $v_{CM} = (v_{IN+} + v_{IN-})/2$ of the input voltages v_{IN+} and v_{IN-}. Like the DB-OTA, the DIGOTA reliance on logic gates inherently reduces the power floor imposed by bias currents and reference circuits necessary in conventional analog OTAs, enabling power savings well beyond their analog counterparts.

In the previous DB-OTAs, a common-mode compensation loop was added to the primary inputs via a passive summing network implemented by on-chip resistors, pseudo-resistors, or quasi-floating gate transistors, at the cost of substantial area overhead (e.g., 45%) and voltage gain degradation (-6dB, see Eq. (2.17)). On the other hand, in the DIGOTA, as shown in Fig. 3.1, the *summing network* is suppressed by introducing an input stage based on the *Muller C-elements* (EMMERT; VANDEWERKER, 2021). The *Muller C-element* output is 1 when its inputs are (0,0), 0 when they are (1,1) and held (high impedance mode) at the previous value when they are (0,1) or (1,0) as in Fig. 3.1 top-right.

The two *Muller-C elements* are driven by the two OTA input voltages v_{IN+} and v_{IN-}, and their remaining input is driven by the digital common-mode compensation signal PD. PD comes from the *Muller-C (MC) swap* subblock. From Fig. 3.1, PD=1 (PD=0) activates the pull-down (pull-up) network of the *Muller C-elements*, and hence leads to a monotonically decreasing (increasing) waveform in their output voltages v_{MUL+} and v_{MUL-}. In turn, these voltages respectively drive the *inverters*, $INV+$ and $INV-$, whose digital outputs ($\overline{MUL_+}$) and ($\overline{MUL_-}$) determine the output PD of the swapping circuit *MCswap* to close the common-mode compensation loop. Similar to the DB-OTA, DIGOTA has the same *output stage* in charge to detect the lag of signals caused by a $v_D \neq 0$.

In summary, while the DB-OTA is comprised by *summing network*, *DM amplifier*, *CM extractor* and *output stages*, the DIGOTA has *Muller C-elements*, *inverters*, *MCswap* and *output stages* as sub-blocks.

3.1.1 Qualitative Circuit Analysis

When a common-mode input is applied (i.e., $v_D = 0$), *MCswap* in Fig. 3.1 detects the conditions (0,0) and (1,1), as described previously for the DB-OTA in the table of Fig.

Figure 3.2: Logic states and state transition graph.

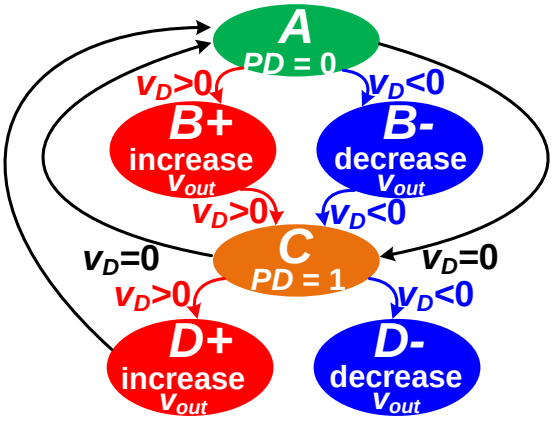

LOGIC STATES

A	$\overline{MUL_+}$=1 $\overline{MUL_-}$=1	enable MCSwap pull-up (PD = 0)
B+	$\overline{MUL_+}$=1 $\overline{MUL_-}$=0	increase v_{out}
B-	$\overline{MUL_+}$=0 $\overline{MUL_-}$=1	decrease v_{out}
C	$\overline{MUL_+}$=0 $\overline{MUL_-}$=0	enable MCSwap pull-down (PD = 1)
D+	$\overline{MUL_+}$=1 $\overline{MUL_-}$=0	increase v_{out}
D-	$\overline{MUL_+}$=0 $\overline{MUL_-}$=1	decrease v_{out}

2.5. Then, it dynamically compensates the common-mode at nodes v_{MUL+} and v_{MUL-} to maintain it around the trip point voltage V_T of the inverter gates $INV+$ and $INV-$. In detail, the conditions ($\overline{MUL_+}$, $\overline{MUL_-}$) equal to (0,0) and (1,1) alternatively enable the pull-up and the pull-down networks of the Muller C-elements via PD, based on the state transition diagram in Fig. 3.2. When v_{MUL+} and v_{MUL-} are both lower than V_T (i.e., ($\overline{MUL_+}$, $\overline{MUL_-}$)=(1,1)), DIGOTA operates in state A in Fig. 3.2, and MCswap sets $PD = 0$ to activate the pull-up networks of the *Muller C-elements* as in Fig. 3.3a. This increases v_{MUL+} and v_{MUL-}, bringing their common-mode closer to V_T as desired.

Conversely, when v_{MUL+} and v_{MUL-} are higher than V_T (i.e., ($\overline{MUL_+}$, $\overline{MUL_-}$) = (0,0)), DIGOTA operates in state C (Fig. 3.2), *MCswap* sets $PD = 1$, and the pull-down networks of the *Muller C-element*s are activated (Fig. 3.3c). This brings the common mode of v_{MUL+} and v_{MUL-} again closer to V_T, as desired. Hence, the *MCswap* circuit implements a passive-less self-oscillating loop (see Figs. 3.3a-c) dynamically tracking the effect of the common-mode input on v_{MUL+} and v_{MUL-}, as needed by $INV+$ and $INV-$ to sense the differential input (table of Fig. 2.5).

When a non-zero differential input $v_D = v_{IN+} - v_{IN-}$ is applied, the two input voltages v_{IN+} and v_{IN-} driving the *Muller C-elements* determine the currents i_{MUL+} and i_{MUL-} charging (discharging) the capacitance C_{MUL} at their output, as in Fig. 3.1. Starting from state A as discussed above, a small-signal differential input $v_D > 0$ makes $i_{MUL+} < i_{MUL-}$, generating a proportional differential voltage at their outputs v_{MUL+} and v_{MUL-} as in Fig. 3.3b, while moving to state B+ in Fig. 3.2 (all is reversed if $v_D < 0$, moving to state B-). Once the common-mode of these two voltages is brought close to V_T (i.e., within $V_T \pm v_D/2$) by the above self-oscillating loop, their difference can be discriminated by $INV+$ and $INV-$, respecting the condition $|v_{\rm d}/2| > |v_{\rm CM} - V_{\rm T}|$. In

Figure 3.3: DIGOTA circuit details vs logic state under $v_D > 0$ (reverse all directions for $v_D < 0$). The state sequence follows the transition graph in Fig. 2b: a) A, b) B+, c) C and d) D+. The subscript + (-) refers to the case $v_D > 0$ ($v_D < 0$).

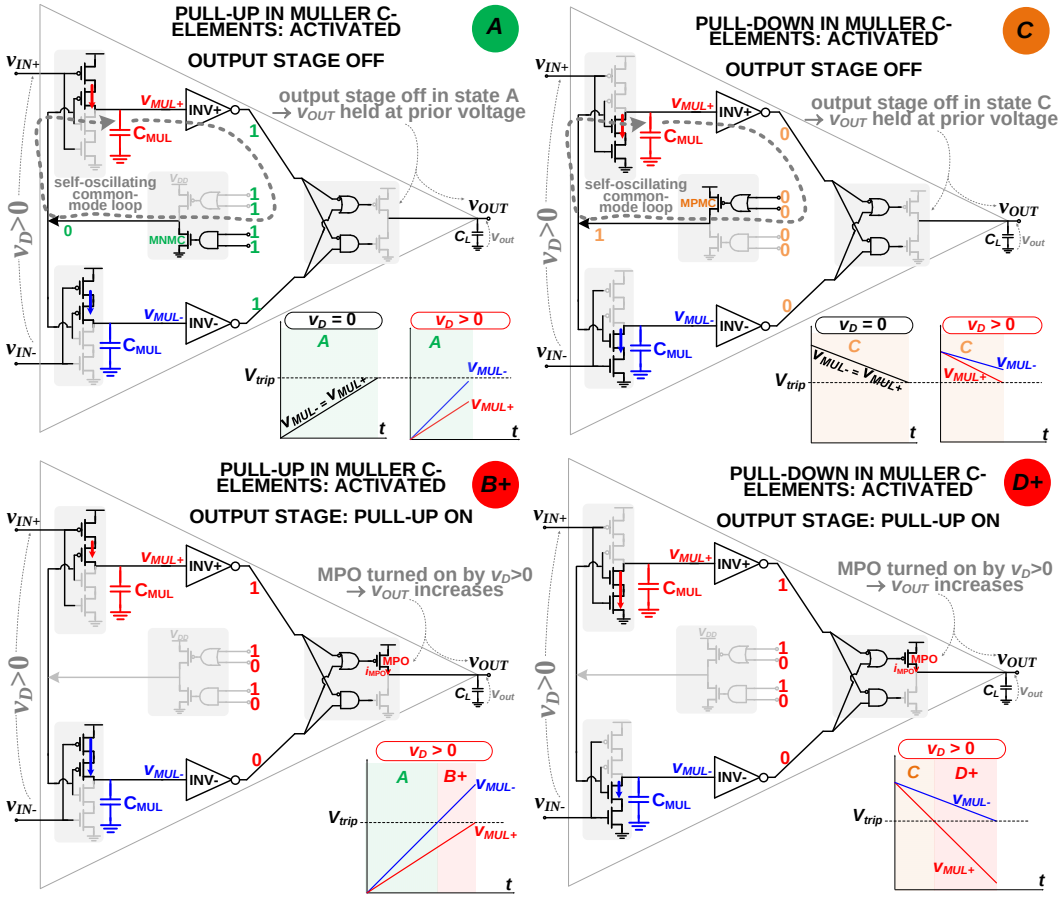

this case, the inverter digital outputs ($\overline{MUL_+}$, $\overline{MUL_-}$) become (1,0) for $v_D > 0$ ((0,1) for $v_D < 0$), triggering operation in state B+ (B-). The same considerations hold when starting from state C in Fig. 3.2, in this case, the circuit moves to state D+ for $v_D > 0$ (D- for $v_D < 0$). The overall DIGOTA state transition graph is summarized in Fig. 3.2 [23].

Finally, the inverter outputs ($\overline{MUL_+}$, $\overline{MUL_-}$) defining the DIGOTA state in Fig. 3.2 drive the output stage, and hence determine the output voltage v_{OUT}. When operating in states B+/D+ (i.e., $v_D > 0$), (($\overline{MUL_+}$, $\overline{MUL_-}$)=(1,0) turns on the pull-up transistor MPO as in Fig. 2a, and correctly raises v_{OUT} as depicted in Figs. 3.3b and 3.3d. The opposite happens in states B-/D- (i.e., $v_D < 0$), which turns on the pull-down MNO transistor to lower v_{OUT}. In practical cases where the DIGOTA is used in a negative-feedback loop configuration (e.g., voltage buffer), v_{OUT} ultimately settles to the value that makes $v_D \approx 0$ Finally, no change in v_{OUT} is observed in states A and C where common-mode compensation is solely performed, as observed in Figs. 3.3a and 3.3c.

3.1.2 Quantitative Circuit Analysis

A model of the DIGOTA circuit has been developed as done for the DB-OTA. Under a pure common-mode input $v_{IN+} = v_{IN-} = v_{CM}$, only the transitions between state A and C are allowed from Fig. 3.2.

Assuming the initial state A and the initial condition $v_{MUL+} = v_{MUL-} = V_{min}$, the output voltages of the *Muller C elements* v_{MUL+} and v_{MUL-} equally increase due to circuit symmetry (see Figs. 3.1, 3.3a and 3.4). In particular, transistors MN2+ and MN2- in Fig. 3.1 are OFF, MP2+ and MP2- are ON (or less OFF), and MP1- and MP1+ are in certain inversion level (see Figs. 3.1 and 3.3a).

The inversion level of a MOS transistor is extracted by a non-linear expression, called Unified Charge-Control Model (UCCM) (SCHNEIDER; GALUP-MONTORO, 2010; TSIVIDIS; MCANDREW, 2010), where it is linked with the transistor terminal voltages as shown in Eq. (3.1).

$$\frac{V_{GB} - V_{T0}}{n} - V_{S(D)} = \phi_t \left[\sqrt{1 + i_{f(r)}} - 2 + ln\left(\sqrt{1 + i_{f(r)}} - 1\right)\right] \tag{3.1}$$

where V_{GB},V_{SB}, and V_{DB} are gate, source and drain to bulk voltages, V_{T0} is threshold voltage, ϕ_t is the thermal voltage and $i_{f(r)}$ is the forward (reverse) inversion level. The i_f and i_r define the equivalent MOS transistor drain current (I_D) through Eq. (3.2),

$$I_D = \mu C'_{ox} n \frac{\phi_t^2}{2} \frac{W}{L} (i_f - i_r) \tag{3.2}$$

where μ is the low field mobility, C'_{ox} is the oxide capacitance per unit of area, n is defined as slope factor, W is transistor width, L is channel length. To achieve ultra-low power operation, the transistors inside of DIGOTA operate in weak inversion and saturation (p.s., for internal waverforms around middle V_{DD}) due to the low voltage supply, i.e., $0.1 > i_f >> i_r$ leading to

$$I_D = \mu C_{ox} n \phi_t^2 e \left(\frac{W}{L}\right) e^{(\frac{V_{GB} - V_{T0}}{n} - V_S)/\phi_t} (1 - e^{V_{DS}/\phi_t}) \approx \mu C_{ox} n \phi_t^2 e \left(\frac{W}{L}\right) e^{(\frac{V_{SG} - V_{T0}}{n\phi_t})} \tag{3.3}$$

Note that, for saturation, $V_{DS} > 4 \cdot \phi_t$ leads to $(1 - 1/e^4) = 0.9817 \approx 1$.

Since $v_{IN+} = v_{IN-} = v_{CM}$, the drain current i_{MUL+} (i_{MUL-}) of MP1+ (MP1-)

charging the capacitance C_{MUL} in Fig. 3.1 is given by Eq. (3.3). Assuming that the input is nearly constant during state A, from Fig. 3.4, C_{MUL} is charged at the constant current $I_{CM,A}$ given by Eq. (3.3) with $v_{SG} = V_{DD} - v_{CM}$, leading to a ramp-like increase in v_{MUL+} and v_{MUL-} from V_{min} to V_T over the period of time τ_{MUL} in (3.4)

$$\tau_{MUL} = (V_T - V_{min}) \cdot \frac{C_{\mathrm{MUL}}}{I_{CM,A}} = (V_T - V_{min}) \frac{C_{\mathrm{MUL}}}{\mu C_{ox} n \phi_t^2 e \left(\frac{W}{L}\right) e^{\frac{V_{DD} - v_{CM} - V_{T0}}{nkT/q}}} \tag{3.4}$$

Once $v_{MUL+} = v_{MUL-} = V_T$, the subsequent inverters *INV+* and *INV-* switch their output from 1 to 0 after a gate delay τ_{INV}, as in Fig. 3.4. Then, the PD signal is updated and makes a $0 \rightarrow 1$ transition after an ***MCswap*** gate delay τ_{MCswap}, thus moving from state A to C as in Fig. 3.4.

From the above considerations and Fig. 3.4, the resulting overall duration T_A of state A is hence equal to

$$T_A = (V_T - V_{min}) \cdot \frac{C_{\mathrm{MUL}}}{I_{CM,A}} + \tau_{INV} + \tau_{MCswap} \tag{3.5}$$

at the end of which v_{MUL+} and v_{MUL-} have kept increasing to their maximum value V_{max} due to the uninterrupted charge of C_{MUL} during the *inverter* and the ***MCswap*** delay. The above analysis can be repeated for state C by considering that v_{MUL+} and v_{MUL-} will now decrease from V_{max} down to V_T due to the discharge of C_{MUL} through the ***Muller C-element*** NMOS current $I_{CM,C}$ in state C (instead of PMOS, see Fig. 3.3c), trigger the transition of *INV+* and *INV-* after τ_{INV}, and the $0 \rightarrow 1$ transition of PD after τ_{MCswap} to return to state A. Hence, the overall duration T_C of state C results to

$$T_C = (V_{max} - V_T) \cdot \frac{C_{\mathrm{MUL}}}{I_{CM,C}} + \tau_{INV} + \tau_{MCswap}. \tag{3.6}$$

Therefore, the overall self-oscillation period $T_0 = T_A + T_C$ is given by

$$T_0 = (V_T - V_{min}) \cdot \frac{C_{\mathrm{MUL}}}{I_{CM,A}} (V_{max} - V_T) + \frac{C_{\mathrm{MUL}}}{I_{CM,C}} + 2 (\tau_{INV} + \tau_{MCswap}) \tag{3.7}$$

Assuming $V_{min} = 0$, $V_{max} = V_{DD}$ and $V_T = V_{DD}/2$, which are reasonable

Figure 3.4: Timing analysis of the self-oscillating loop timing under pure common-mode inputs, and evaluation of the time T_A spent in state A.

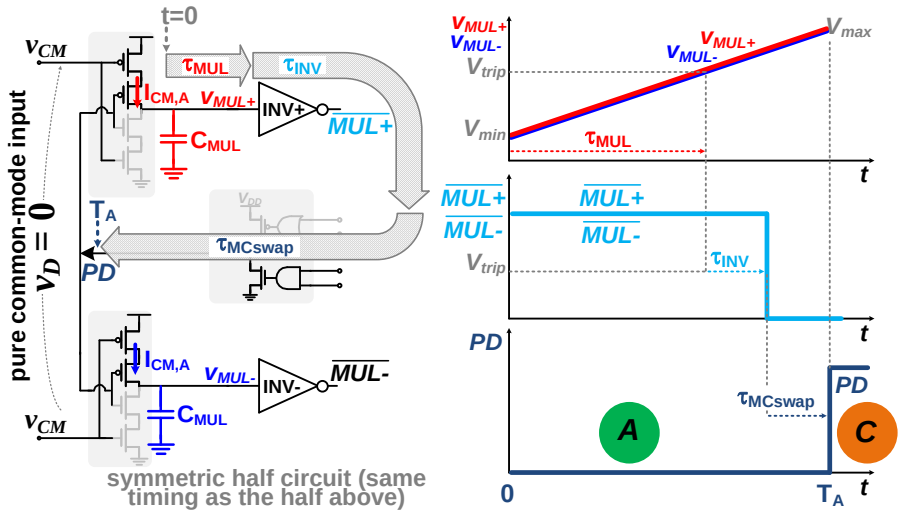

approximations for ultra low voltage, then

$$T_0 = \frac{1}{f_0} = V_{DD} \cdot \frac{C_{\mathrm{MUL}}}{I_{CM}} + 2\left(\tau_{INV} + \tau_{MCswap}\right) \tag{3.8}$$

where

$$I_{CM} = \frac{2}{\frac{1}{I_{CM,A}} + \frac{1}{I_{CM,C}}} = \frac{2}{\frac{1}{I_0 e^{\frac{V_{DD}-v_{CM}}{\frac{nkT}{q}}}} + \frac{1}{I_0 e^{\frac{v_{CM}}{\frac{nkT}{q}}}}} = \frac{I_0 e^{\frac{V_{DD}/2}{nkT/q}}}{\cosh\left(\frac{v_{CM}-\frac{V_{DD}}{2}}{nkT/q}\right)} \tag{3.9}$$

From Eq. (3.8), T_0 is set by the sum of the (typically dominant) delay associated with the Muller C-element, the inverters *INV+* and *INV-*, and the *MCswap* gate delay. In summary, T_0 is the natural the self-oscillation period of DIGOTA and has the well-understood digital logic-like dependence on voltage, temperature, and gate sizing (ALIOTO, 2017).

When a small-signal differential input voltage v_D is added to the common-mode component v_{CM}, its effect can be analyzed as a perturbation to the self-oscillatory circuit behavior (HAJIMIRI; LEE, 1998). The assumption of slow-varying input signals compared to the self-oscillation frequency allows to average out the fluctuations of small-signal parameters during each period. This makes it possible to rely on straightforward small-signal analysis, as detailed in the following.

The circuit in Fig. 3.1 can be linearized as shown in Fig. 3.5. The first stage describes the equal small- signal currents $i_+ = i_-$ with opposite directions coming

Figure 3.5: DIGOTA equivalent circuit and transfer function under differential input v_D.

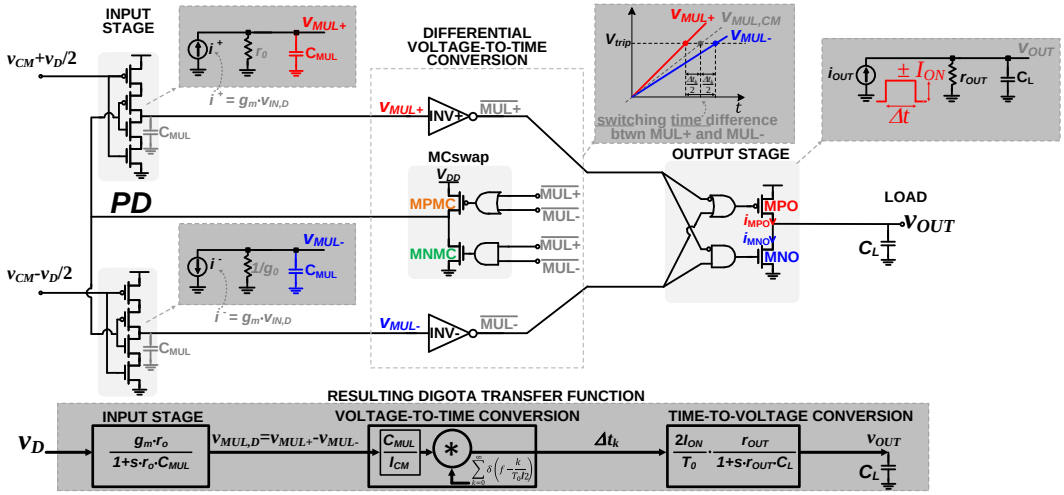

from the *Muller C-elements*, as determined by the opposite small-signal components of $v_{IN+} = v_D/2$ and $v_{IN-} = -v_D/2$. Being small-signal components, these currents are superimposed to the common-mode, Eq.(3.9), and g_m can be expressed as the weighted sum of the transconductances $g_{m,A}$ and $g_{m,C}$ of the DIGOTA circuit in state A and C. The weight is given by the fraction of the period spent in each state, thus leading to

$$g_m = g_{m,A}\frac{T_A}{T_0} + g_{m,C}\frac{T_C}{T_0} \approx \frac{I_{CM,A}}{nkT/q}\frac{I_{CM}}{2I_{CM,A}} + \frac{I_{CM,B}}{nkT/q}\frac{I_{CM}}{2I_{CM,B}} = \frac{I_{CM}}{nkT/q} \tag{3.10}$$

The same approach can be done for r_o, leading to a $r_o = \frac{nkT/q}{\lambda_{DIBL} I_{CM}}$. λ_{DIBL} is the drain induced barrier lowering (DIBL) coefficient.

Qualitatively, from Fig. 3.5 the opposite small-signal currents i_{MUL+} and i_{MUL-} at the outputs of the Muller C-elements lead to different slopes in voltages v_{MUL+} and v_{MUL-}, during state A (same for C). This leads to a small-signal difference of the time when v_{MUL+} and v_{MUL-} reach V_T, and hence to the signed difference Δt between the switching of the $INV+$ and the $INV-$ output. Under small-signal analysis, such time difference Δt is inherently proportional to v_D. As exemplified in Fig. 3.6, during states B and D the time difference Δt activates the output stage transistor MPO if $v_D > 0$ (MNO if $v_D < 0$), which charges (discharges) the capacitive load C_L. This translates into a small-signal change in v_{OUT} that is proportional to v_D, and has the same sign, as expected from an OTA (see Fig. 3.6). From the small-signal circuit in Fig. 3.5, the transfer function

Figure 3.6: Operation of DIGOTA under positive and negative input differential voltages.

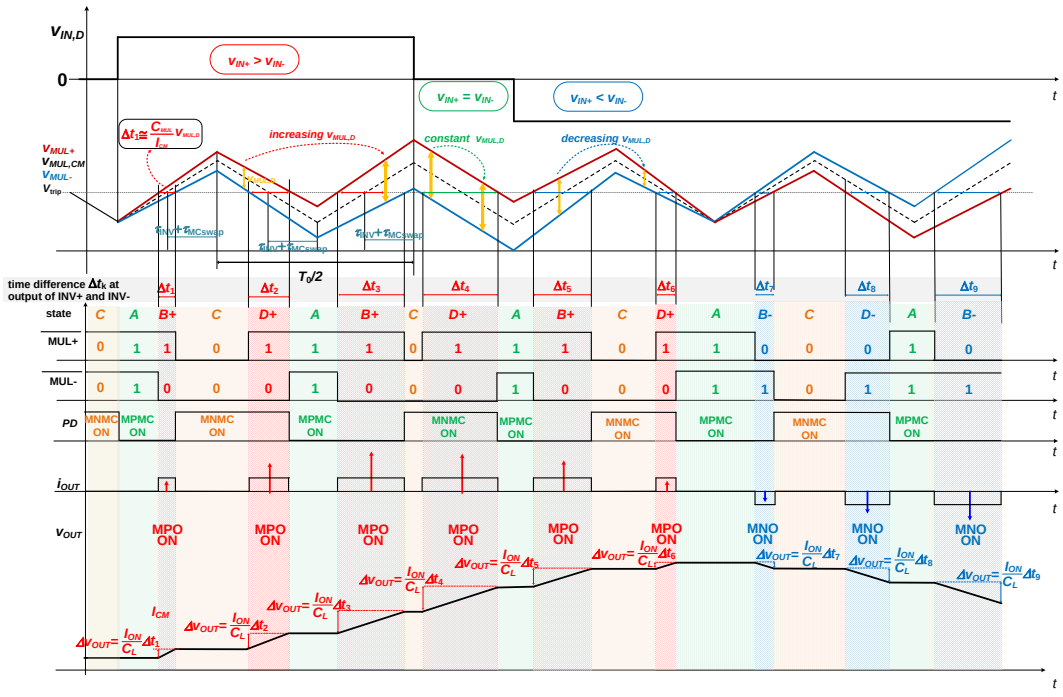

from v_D to the differential output at the Muller-C elements is

$$\frac{v_{MUL,D}\left(s\right)}{v_D\left(s\right)} = \frac{v_{MUL+}\left(s\right) - v_{MUL-}\left(s\right)}{v_D\left(s\right)} = \frac{g_m r_o}{1 + s \cdot r_o C_{MUL}}. \tag{3.11}$$

From Eq. (3.11), the input stage has a first-order transfer function whose low frequency gain is equal to the transistor intrinsic gain $g_m r_o$.

The impact of v_D on the differential output of the *Muller-C elements* determines a difference Δt in the point of time when V_T of $INV+$ and $INV-$ are crossed by v_{MUL+} and v_{MUL-}, as shown in Fig. 3.5 and exemplified in Fig. 3.6. The difference Δt_k at a given cycle k of the common-mode self-oscillation with the period $T_{CM,k}$ in Eq. (3.8) stems from the voltage-to-time conversion performed by the $INV+$ and $INV-$, and is crucial for the DIGOTA circuit operation. In detail, the DIGOTA circuit operates in state B (D) during the time interval $(T_{CM,k} - \Delta t_k/2, T_{CM,k} + \Delta t_k/2)$ right after being in state A (C), thus enabling the output stage as in Fig. 3.6. During this interval, the load capacitance C_L is charged (discharged) for a time proportional to Δt_k if $v_D > 0$ ($v_D < 0$). Assuming again that the input varies slowly and is nearly constant during T_0, v_{MUL+} and v_{MUL-} around V_T can be expressed through linear interpolation, thus yielding

$$v_{MUL+}\left(T_{CM,k} - \frac{\Delta t_k}{2}\right) = v_{MUL,CM}\left(T_{CM,k} - \frac{\Delta t_k}{2}\right) + \frac{v_{MUL,D}(T_{CM,k})}{2}$$

$$= v_{MUL,CM}\left(T_{CM,k}\right) - \left.\frac{\partial v_{MUL,CM}}{\partial t}\right|_{T_{CM,k}} \frac{\Delta t_k}{2} + \frac{v_{MUL,D}(T_{CM,k})}{2} \tag{3.12}$$

$$v_{MUL-}\left(T_{CM,k} + \frac{\Delta t_k}{2}\right) = v_{MUL,CM}\left(T_{CM,k} + \frac{\Delta t_k}{2}\right) - \frac{v_{MUL,D}(T_{CM,k})}{2}$$

$$= v_{MUL,CM}\left(T_{CM,k}\right) + \left.\frac{\partial v_{MUL,CM}}{\partial t}\right|_{T_{CM,k}} \frac{\Delta t_k}{2} - \frac{v_{MUL,D}(T_{CM,k})}{2} \tag{3.13}$$

The common-mode voltage contribution $v_{MUL+} = v_{MUL-} = v_{MUL,CM}$ in Eq. (3.12) and 3.13 is due to the discharge of capacitors through the common-mode current I_{CM} in Eq. (3.9) at the constant rate I_{CM}/C_{MUL}. This makes $\left.\frac{\partial v_{MUL,CM}}{\partial t}\right|_{T_{CM,k}}$ equal to I_{CM}/C_{MUL} in Eq. (3.12) and (3.13). Also, $v_{MUL,CM}(T_{CM,k}) = V_T$ since $T_{CM,k}$ is defined as the time at which $v_{MUL,CM}$ crosses V_T. Accordingly, Eq. (3.12) and (3.13) lead to the following $\Delta t_k/v_{MUL,D}$ transfer function

$$\frac{\Delta t_k}{v_{MUL,D}(T_{CM,k})} = \frac{C_{\mathrm{MUL}}}{I_{CM}} \tag{3.14}$$

which quantifies the small-signal voltage-to-time conversion performed by $INV+$ and $INV-$ in Fig. 3.5. Since zero crossings occur every half period, voltage-to-time conversion takes place every $T_0/2$ and leads to the generation of a signed time difference Δt_k whose sign is the same as v_D, and its width is proportional to $v_{MUL,D}$ evaluated at $kT_0/2$. In other words, the input is effectively sampled with a sampling period $T_0/2$, where T_0 is expressed in Eq. (3.8). Hence, as in the DB-OTA, the negative feedback in DIGOTA through the *MCswap* circuit acts such as a self-oscillating threshold sampler (HERNANDEZ; PREFASI, 2008) with a natural sampling frequency of $2/T_0$.

In the output stage in Fig. 3.5, the pulses Δt_k turn on the MPO (MNO) if $v_D > 0$ ($v_D < 0$) for a duration Δt_k. When the time difference Δt_k is non-zero, MPO (MNO) generates a current $I_{ON}(-I_{ON})$ driving the capacitive load, as MPO and MNO are sized to deliver the same current to C_L. Since time pulses Δt_k take place every $T_0/2$, the output stage current $i_{OUT}(t)$ driving C_L can be written as

$$i_{OUT}(t) = \sum\nolimits_{k=0}^{+\infty} I_{ON}\Delta t(t)\delta\left(t - \frac{k}{2f_0}\right) \tag{3.15}$$

where the sign of the output current was incorporated in Δt_k, from the above considera-

tions. The Laplace transform of Eq. (3.15) can be evaluated as in (Kalani; Kinget, 2020) from the z transform of Δt_k evaluated in $z = e^{(sT_0/2)}$. Assuming that the input signal frequency is much lower (10X less) than the self-oscillation frequency $2/T_0$ (e.g., by at least an order of magnitude), the output current $I_{out}(s)$ is evaluated by putting together the Eqs. (3.11), (3.14), and (3.15). Straightforward calculations reveal that $I_{out}(s)$ is related to the input differential voltage $V_D(s)$ as in a first-order continuous-time linear circuit, as demonstrated in the previous chapter for the DB-OTA.

More specifically, considering that I_{out} flows through the impedance defined by r_{OUT} in parallel with C_L from Fig. 3.5, the differential voltage gain transfer function of DIGOTA is

$$A_D(s) = \frac{V_{OUT}(s)}{V_D(s)} = \frac{2g_m r_o \cdot \frac{I_{ON}}{I_{CM}} \cdot \frac{r_{OUT} C_{\mathrm{MUL}}}{T_0}}{(1 + s \cdot r_{OUT} C_L) \cdot (1 + s \cdot r_o C_{MUL})} \tag{3.16}$$

From Eq. (3.16), DIGOTA has a second-order transfer function when a differential input is applied and the its DC gain is

$$A_{V0} = 2g_m r_o \cdot I_{ON} \cdot \frac{r_{OUT} C_{\mathrm{MUL}}}{T_0 \cdot I_{CM}} \tag{3.17}$$

and is much higher than one. Indeed, $g_m r_o > 1$ since it is the intrinsic transistor gain, whereas $I_{ON}/I_{CM} > 1$ since the output stage always sees a full-swing input and is hence fully ON, whereas I_{CM} in Eq. (3.9) is much lower than the transistor ON current.

The frequency response in Eq. (3.16) has two real negative poles:

$$s_{p1} = -\frac{1}{r_{OUT} C_{\mathrm{L}}} \quad \therefore \quad s_{p2} = -\frac{1}{r_o C_{\mathrm{MUL}}} \tag{3.18}$$

where s_{p1} is dominant, since the load capacitance C_L is orders of magnitude larger than the transistor parasitic capacitance C_{MUL}, whereas r_{OUT} and r_o are small-signal transistor output resistances and are hence much closer to each other. The resulting gain-bandwidth product f_{GBW} is

$$f_{GBW} = \frac{1}{2\pi} \cdot \frac{2}{T_0} \cdot \frac{I_{ON}}{I_{CM}} \cdot g_m r_o \cdot \frac{C_{MUL}}{C_L} \tag{3.19}$$

The expression of the power consumption of DIGOTA is similar to the DB-OTA one. It is re-written here below just as matter of the convenience.

$$P_{DIGOTA} \approx \frac{2}{T_0} C_{int} V_{DD}^2 + f_S C_L V_{OUT}^2 \tag{3.20}$$

Figure 3.7: Common-Source amplifier biased in weak inversion. During the calculation the required I_Q, the current of left side of the current mirror is neglected.

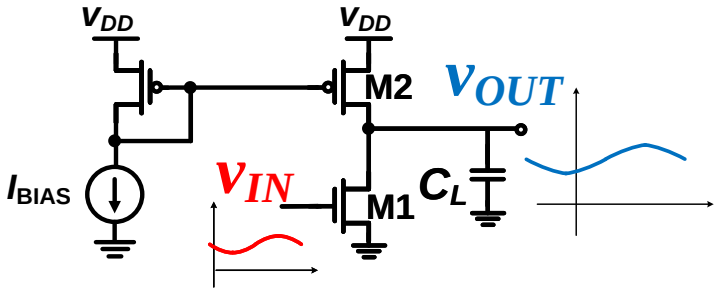

Table 3.1: Parameters From Simulations, DIGOTA Transistor Sizes

Transistor	W (μm)	L (μm)	Transistor	W (μm)	L (μm)
$MN1_{\pm}$	3.9	0.18	$MP1_{\pm}$	9	0.18
$MN2_{\pm}$	5	0.18	$MP2_{\pm}$	6.85	0.18
MNMC	1	0.18	MPMC	2.5	0.18
MNO	1	0.18		8.48	0.18
	strength			strength	
$INV_{\pm}$	5X		AND/OR	5X	
NegNOR	5X		NegAND	5X	
parameter	value	unit	parameter	value	unit
T_0	13	μs	r_{OUT}	7.8	nS
g_m	27	nS	C_{MUL}	8	fF
g_0	1.35	nS	C_{int}	170	fF
I_{CM}	930	pA	C_L	150	pF
I_{ON}	9.15	nA			

Interestingly, DIGOTA is inherently more power-efficient than a conventional common-source (CS) amplifier biased in weak inversion (Kinget, 2015) keeping the same gain-bandwidth product (see Fig. 3.7). This is shown by comparing the DIGOTA power in Eq. (3.20), and the power P_{CS} of the common-source stage in Eq. (3.21)

$$P_{CS} = V_{DD}\ I_Q|_{f_{GBW}} = 2\pi f_{GBW} C_L \frac{nkT}{q} V_{DD} \tag{3.21}$$

which was evaluated as the product of the supply voltage and the quiescent current I_Q required to match the same f_{GBW}. The resulting power ratio leads to

$$\frac{P_{DIGOTA}}{P_{CS}} \approx \frac{P_{gates}}{P_{CS}} = \frac{1}{4\pi g_m r_o} \frac{C_{int}}{C_{MUL}} \frac{I_{CM}}{I_{ON}} \frac{V_{DD}}{nkT/q} \tag{3.22}$$

when the P_{DIGOTA} is dominated by internal oscillation f_0.

Simulations in 180 nm CMOS at $V_{DD} = 0.3V$ for $f_S = 2$Hz lead to the effective small-signal parameter values (averaged over the common-mode input values) in Table 3.1, from which the ratio in Eq. (3.22) makes the DIGOTA power 23X lower than the

conventional CS stage (without counting the extra circuit needed to bias the CS). This improvement is achieved thanks to the suppression of the constant power required by a bias current, in view of the digital nature of DIGOTA.

When the DIGOTA power is dominated by the P_{out} (e.g., large C_L, signal amplitude ΔV_{OUT}, and frequency $f_S \approx f_{GBW}$), the expression of the power ratio becomes

$$\frac{P_{DIGOTA}}{P_{CS}} \approx \frac{1}{g_m r_o} \cdot \frac{1}{nkT/q} \frac{V_{OUT}^2}{V_{DD}} \tag{3.23}$$

which corresponds to a 16X power saving under full-swing output $V_{OUT} = V_{DD}/2$. DIGOTA has an intrinsic advantage in power efficiency regardless of the specific load and input signal.

3.1.3 Circuit Design

The DIGOTA architecture in Fig. 3.1 is fully digital and can hence be designed with digital standard cells and no passives, drastically reducing the design and the system integration effort. Compared to conventional analog design, DIGOTA enables digital-like area scaling across technology generations, and design and technology portability. As main limitation, the adoption of standard cells restricts the choice of transistor sizes to the discrete set of strengths available in the adopted library. Also, Muller-C cells might not be directly available in the library, although they can be easily implemented by merging an open-drain NAND and NOR gate, as shown in Fig. 3.1 top-right.

In the 180-nm testchip designed to experimentally validate DIGOTA models (see Fig. 3.8), cells were sized to pursue high power efficiency, as quantified by the small-signal and the large-signal figures of merit in Eqs. (3.24) and (3.25) (Toledo et al., 2020) :

$$FOM_S = \frac{GBW \cdot C_L}{Power} \tag{3.24}$$

$$FOM_L = \frac{SR \cdot C_L}{Power} \tag{3.25}$$

where $SR = I_{ON}/C_L$ is the slew rate averaged between the rising and falling transitions. FOM_S is used to demonstrate how efficient the OTA is, showing for a fixed load C_L how much Hz of bandwidth is achieved per unit of power. On the other hand, for the

Figure 3.8: Test bench, micrograph of the DIGOTA 180-nm testchip and layout. Use the QR code to watch the demo video of the DIGOTA working powered by light harvester (7 mm^2).

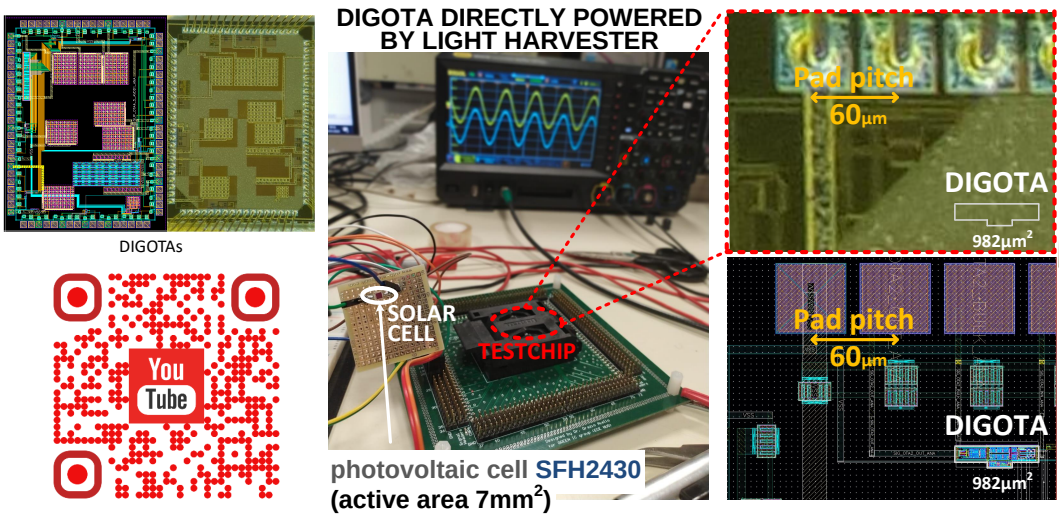

Figure 3.9: Micrograph of the DIGOTA 180 nm testchip and area breakdown.

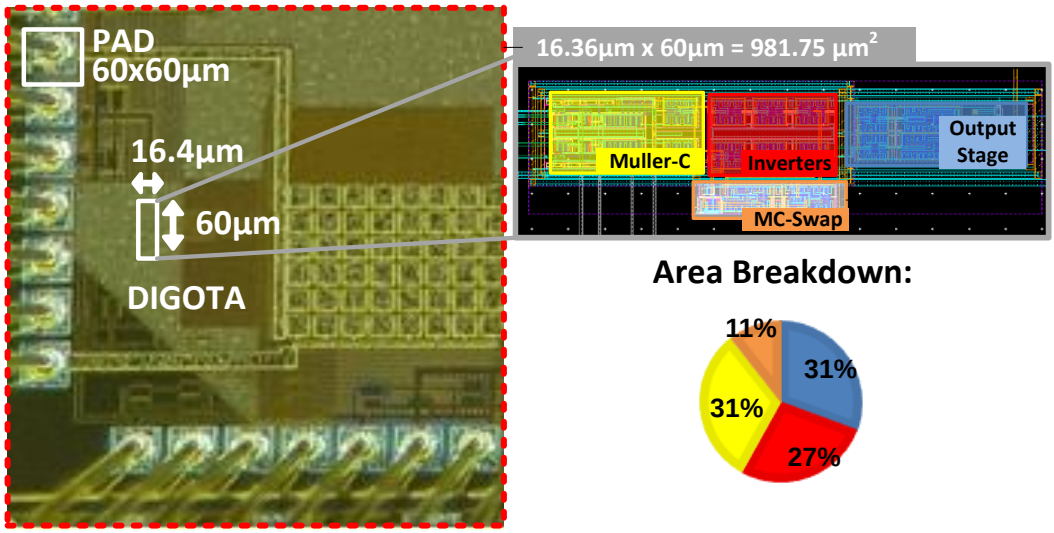

same fixed load, FOM_L expresses the ability of the OTA to vary its output voltage under large-signal operation normalized to its power consumption. Note that $SR = dv_{out}/dt$.

By substituting (3.19) and (3.20) in (3.24) and (3.25), the figures of merit can be simplified as

$$FOM_S = \left(\frac{g_m r_o}{2\pi C_{int} V_{DD}^2} \frac{C_{MUL}}{I_{CM}}\right) \cdot I_{ON} \tag{3.26}$$

$$FOM_L = \left(\frac{1}{C_{int} V_{DD}} \frac{C_{MUL}}{I_{CM}}\right) \cdot I_{ON} \tag{3.27}$$

Both FOMs are inversely proportional to C_{int} and the slope I_{CM}/C_{MUL} of the

Figure 3.10: [SIMULATIONS] a) Input and Output waveform in voltage follower configuration for a 100 samples MC analysis. b) Voltage offset c) THD d) Power histograms for a 100 samples MC analysis.

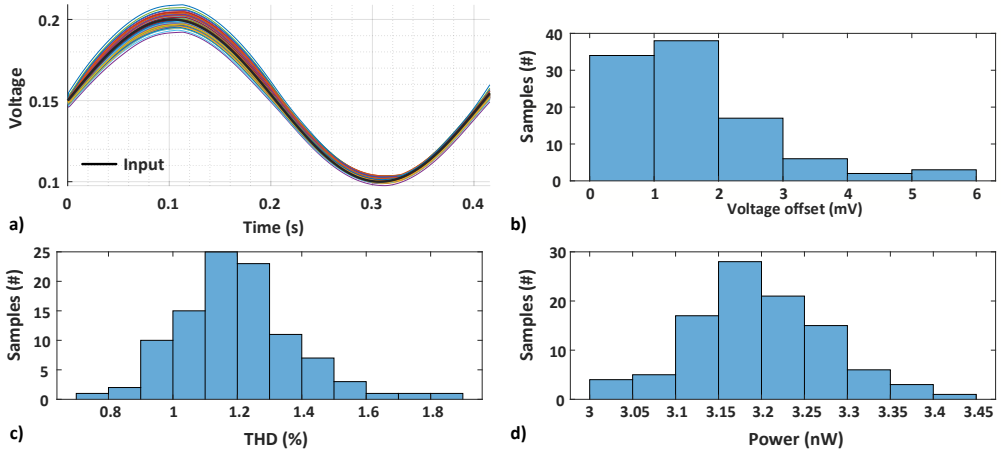

Figure 3.11: [SIMULATIONS] a) DC gain and b) f_{GBW} histograms for a 100 samples MC analysis.

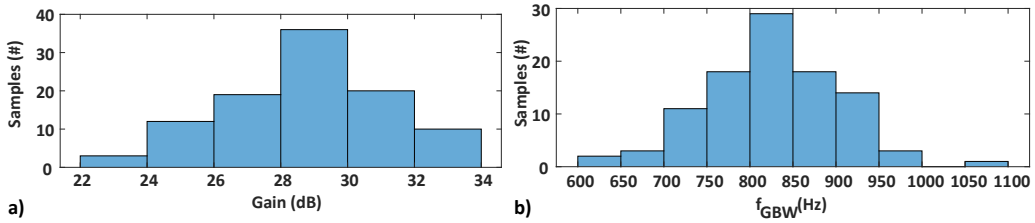

Muller-C element output voltage. Hence, the FOMs expectedly benefit from the adoption of minimum-sized logic gates and the reduction in the self-oscillation frequency in Eq. (3.8), as they both reduce the consumption associated with the logic gates in the self-oscillating loop.

Regarding the output stage, higher strength and I_{ON} in the output stage directly improve both figures of merit. The cell strengths within the self-oscillating loop were chosen as a tradeoff between the offset voltage (decided by the Muller-C area accoring to Pelgrom's law (GALUP-MONTORO et al., 2005b)), the bandwidth, and the input-referred noise (decided by the Muller-C area and power). In particular, reducing offset voltage and noise requires transistor up-sizing in the first stage, whereas improving f_{GBW} requires transistor up-sizing in the output stage so that a higher I_{ON} is delivered. The strength of the output stage cell was set to drive a load capacitance of C_L=150 pF at f_{GBW}=800 Hz, to demonstrate the power efficiency of DIGOTA even under heavy capacitive loads.

Figure 3.12: [SIMULATIONS] Temperature dependence of DC voltage gain and gain-bandwidth product vs. temperature, total harmonic distortion and power.

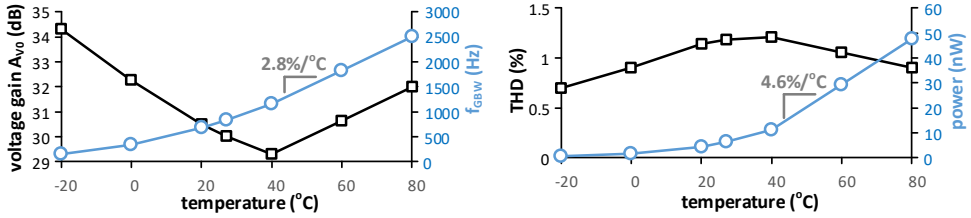

3.2 Layout

The DIGOTA core occupies an area of 982 μm^2, as shown in Fig. 3.9. The DIGOTA area breakdown is also shown in Fig. 3.9, highlighting that *Muller-C* occupies 31% of total area as well as the *output stage*. Inverters spend 27% of silicon area, while the *MCSwap* only 11%.

3.3 Simulations Results

Unlike the DB-OTA in which its voltage offset is strongly dependent on the inverter trip point mismatch (see Eqs. (2.26) - (2.28)), the *Muller-C* first stage gain given by the Eq. (3.11) is found to be less sensitive to device mismatch. Eq. (3.28) shows that the more relevant terms for the total offset voltage are the mismatch of *Muller-C element*. Moreover, the mismatch from the summing network is eliminated.

$$\sigma_{V_{\mathrm{OS}}} \approx \sqrt{\frac{\sigma^2_{\mathrm{I_N}}}{g_m^2} + \frac{\sigma^2_{\mathrm{I_P}}}{g_m^2} + \frac{\sigma^2_{C_{MUL}} \cdot I^2_{CM,TP}}{\left(g_m C_{MUL}\right)^2} + \frac{\sigma^2_{V_T}}{\left(g_m r_o\right)^2}} \approx \sqrt{\frac{\sigma^2_{\mathrm{I_N}}}{g_m^2} + \frac{\sigma^2_{\mathrm{I_P}}}{g_m^2} + \frac{\sigma^2_{C_{MUL}} \cdot I^2_{CM,TP}}{\left(g_m C_{MUL}\right)^2}} \tag{3.28}$$

where σ represents the the local variations w.r.t. each parameter already presented.

The mismatch contribution simulation in the Cadence environment reveals that less than 5% of the total offset comes from the trip point mismatch for DIGOTA, whereas in DB-OTA their contribution accounts for more than the 80%. Fig. 3.10a shows the input and output waveform in voltage follower configuration for a 100 samples MC analysis and Fig. 3.10b, the OTA offset voltage for the same study. No signal saturation is found, proving that the DIGOTA is more robust to process variations than DB-OTA, even work-

Figure 3.13: [MEASUREMENTS] a) sine and b) square wave response when directly powered by a 1-mm2 solar cell at <100 lux (dark overcast day) (2.5-Hz frequency, 75-mV amplitude).

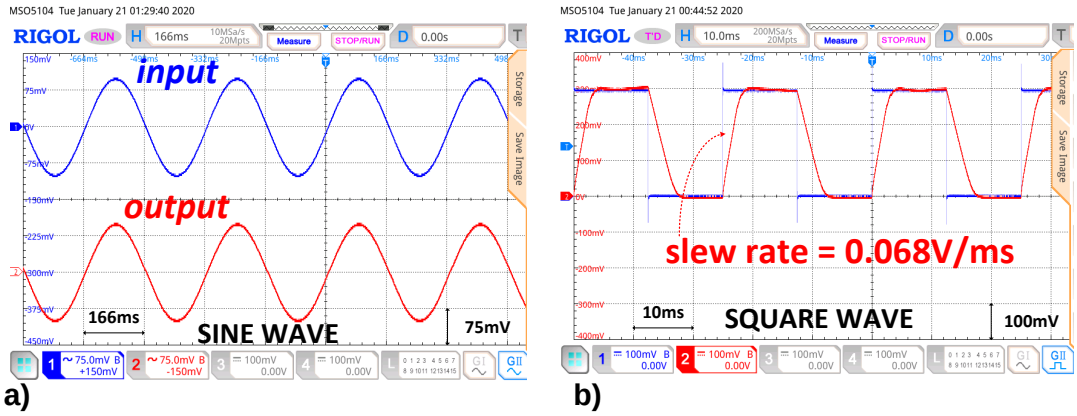

ing in weak inversion where the matching issues are more critical (GALUP-MONTORO et al., 2005a). For the same MC analysis, THD, Power, DC gain and GBW are shown in Fig. 3.10c, Fig. 3.10d, Fig. 3.11a, and Fig.3.11b, respectively.

Regarding the impact of temperature, from Fig. 3.12 the DC gain A_{V0} is relatively independent of the temperature with a maximum fluctuation of 5 dB over the highest value of 34.3 dB. From the same figure, f_{GBW} increases exponentially at a rate α of 2.8%/^{o}C, where the exponential growth rate α is defined as:

$$\alpha = \left(\frac{f_{GBW}|_{T_1}}{f_{GBW}|_{T_0}} \right)^{\frac{1^\circ C}{T_1 - T_0}} - 1 \tag{3.29}$$

in which $f_{GBW}|_{T_1}$, $f_{GBW}|_{T_0}$ are the f_{GBW} values at T_0=-20^{o}C and T_1=80^{o}C, respectively.

From the same Fig. 3.12, the total harmonic distortion (THD) is nearly independent of the temperature, due to the minor temperature effect on the static characteristics of CMOS logic gates. The power expectedly increases exponentially with the temperature at a rate of 4.6%/^{o}C defined as in Eq. (3.29), as determined by the adopted technology since leakage increases by the very same rate.

3.4 Measurements Results

The measured response of the DIGOTA circuit in the voltage follower configuration to sine and square wave inputs is shown in Fig. 3.13 under a 0.3-V supply generated directly by a mm-scale solar cell. The measurements in the following were carried out by setting the supply voltage with a source meter, to assure repeatable and well-defined

Figure 3.14: [MEASUREMENTS] Open-loop frequency response at V_{DD}=0.3 V, C_L=150 pF: a) magnitude and b) phase from testchip measurements and model in Eq. (3.16).

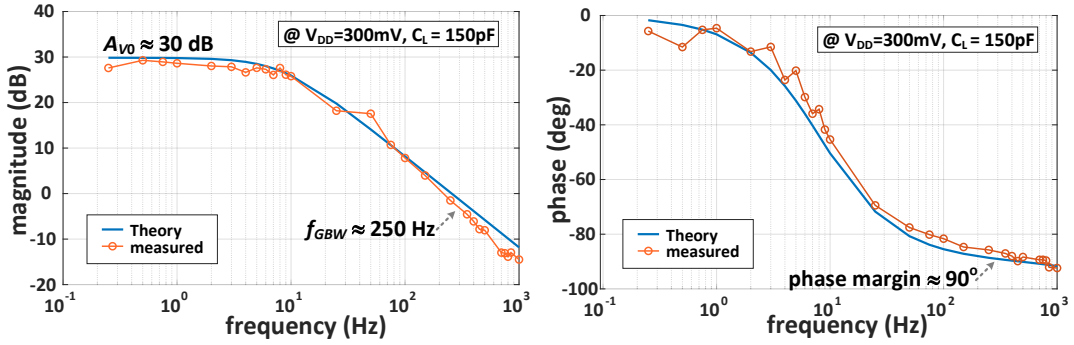

Figure 3.15: [MEASUREMENTS] a) Output spectrum under sine wave input (2.5 Hz, 75-mV), b) THD vs amplitude under sine wave input (2.5 Hz), at V_{DD}=0.3 V, C_L=150 pF.

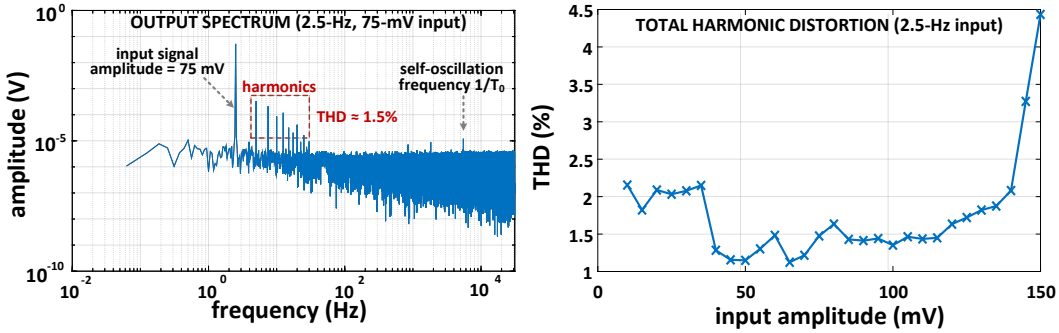

testing conditions.

The DIGOTA open-loop frequency response is plotted in Fig. 3.14, as evaluated from testchip characterization and the model in Eq. (3.16). At the low voltage of 0.3 V and a heavy capacitive load of 150 pF, this figure shows a 30-dB DC gain, a 250-Hz gain-bandwidth product, and a 90^o phase margin. Fig. 3.14 shows good agreement between model and the measurements, with an average (maximum) error of 1.13dB (3.4dB) for the magnitude, and 4.6^o (11 ^{o}) degrees for the phase. For DC inputs, the measured CMRR is 41dB, whereas the measured PSRR is 30dB at the same 0.3-V supply. The open-loop output resistance r_{OUT} is 21MΩ.

The measured spectrum of the DIGOTA output for a 2.5-Hz sine wave with 75-mV amplitude is reported in Fig. 3.15, which shows the harmonics due to distortion and the out-of-band self-oscillation frequency tone at 8kHz. The resulting total harmonic distortion THD in Fig. 3.15 is less than 2% for input amplitudes exceeding 90% of the rail-to-rail swing, corresponding to 7-bit linearity (no noise included). The THD was found to slightly increase by 0.1% at higher frequencies. Hence, linearity sets the ultimate limit to the resolution of sensor interfaces based on DIGOTA, rather than noise.

Figure 3.16: [MEASUREMENTS] a) Power (Eq. (3.20)) and gain-bandwidth product (Eq. (3.19)) vs V_{DD}, b) power (Eq. (3.20)) vs input frequency (50-mV amplitude, V_{DD}=0.3V).

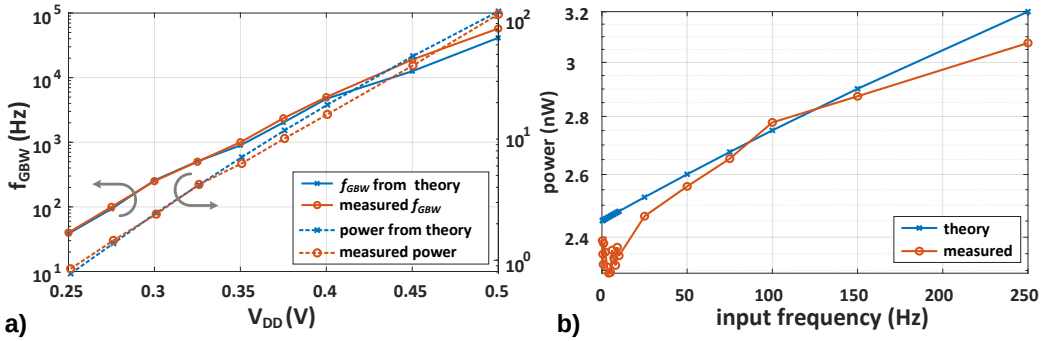

Figure 3.17: [MEASUREMENTS] a) Magnitude Open-loop frequency response across twelve DIGOTA dices b) Magnitude response of the closed-loop transfer function of twelve DIGOTA dices in the voltage follower configuration.

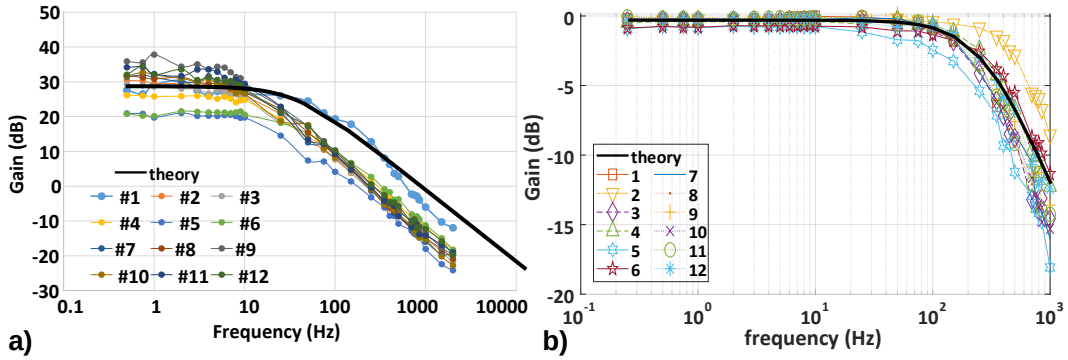

The power consumption at 0.25-0.5 V supply and 150-pF capacitive load range from 850 pW to 107 nW, as plotted in Fig. 3.16a. The power model in Eq. (3.20) agrees with measurements with an average error of 9%. From the same figure, the gain-bandwidth product ranges from 40 Hz to 57.5 kHz, which is modeled by Eq. (3.20) with an average error of 15%. The exponential increase of power and f_{GBW} with V_{DD} in Fig. 3.16a is due to the exponential increase in the transistor sub-threshold current I_{ON} in Eq. (3.19), and consequently in the frequency $1/T_0$. Also, Fig. 3.16b shows the nearly-linear dependence of the power consumption on the input frequency f_S, as expected from the power contribution of the output stage in Eq. (3.20).

The resulting figures of merit FOM_S in Eq. (3.24) and FOM_L in Eq. (3.25) are in the 7.1-80.2 $\mathrm{MHz \cdot pF/\mu W}$ and 4.2-26.5 $\mathrm{(V/\mu s)pF/\mu W}$ range. The average error of the model in Eqs. (3.26) and (3.27) with respect to the measurements is respectively 25% and 12%. Regarding the voltage dependence, Fig. 11c confirms that FOM_S is proportional to $e^{(2V_{DD}/(nkT/q))}/V_{DD}^2$ as in Eq. (3.26), and FOM_L is proportional to $e^{(2V_{DD}/(nkT/q))}/V_{DD}^2$ as in Eq. (3.27), at low voltages that keep transistors in the sub-threshold region.

Figure 3.18: [MEASUREMENTS] a) Measurement results across twelve dice and effect of process variations on gain-bandwidth product, slew rate and power consumption (V_{DD}=0.3 V).

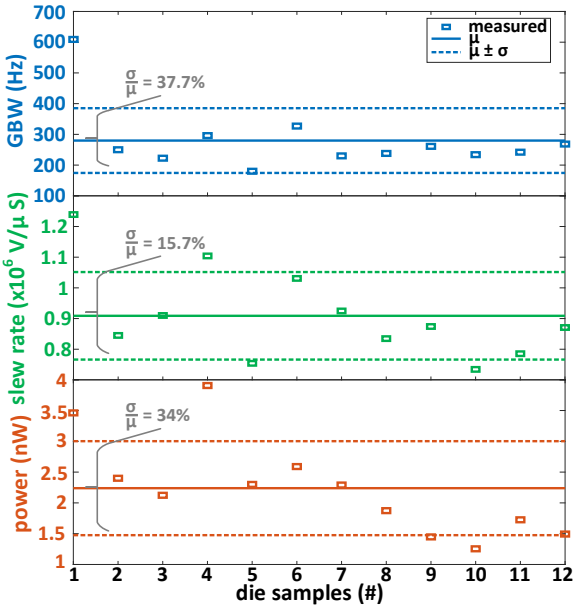

The consistency of the above results under process variations was validated through the characterization of twelve DIGOTA die samples, as plotted in Fig. 3.17 for the open and closed-loop frequency response. At the voltage of 0.3 V and without the support of any bias circuitry, the mean value and standard deviation of the DC gain are respectively -0.33 and 0.23 dB (in closed-loop). The mean value and the standard deviation for the –3dB cutoff frequency are respectively 265 Hz and 99 Hz (closed-loop), leading to variability of 37%. This confirms reasonable consistency without the need for calibration, unlike previously proposed DB-OTA.

The gain-bandwidth product, the slew rate, and the power consumption for the measured samples are reported in Fig. 3.18. This figure confirms fairly consistent performance across dice, despite operation at very low voltage and the absence of a bias current reference. From Fig. 3.18, the variability of f_{GBW}, SR, and power is respectively 37.7%, 15.7%, and 34%. As a reference, the variability of the technology is quantified by the 51% variability of the FO4 delay at V_{DD}=0.3 V. Accordingly, the variability of f_{GBW}, SR, and power is lower than the FO4 variability, confirming the resilience of the DIGOTA architecture against process variations. At 0.5 V, the variability of f_{GBW}, SR, and power become 15%, 64%, and 30%, respectively.

The input offset voltage standard deviation across the twelve dice is 4.7 mV, from the available samples in Fig. 3.19a.

Figure 3.19: [MEASUREMENTS] a) Measured input offset voltage of twelve DIGOTA dice and resulting mean value and standard deviation b) Measured total harmonic distortion (THD) of twelve DIGOTA dice, their mean value, and standard deviation vs input sinewave amplitude (2.5 Hz input, V_{DD}=0.3 V, C_L=150 pF).

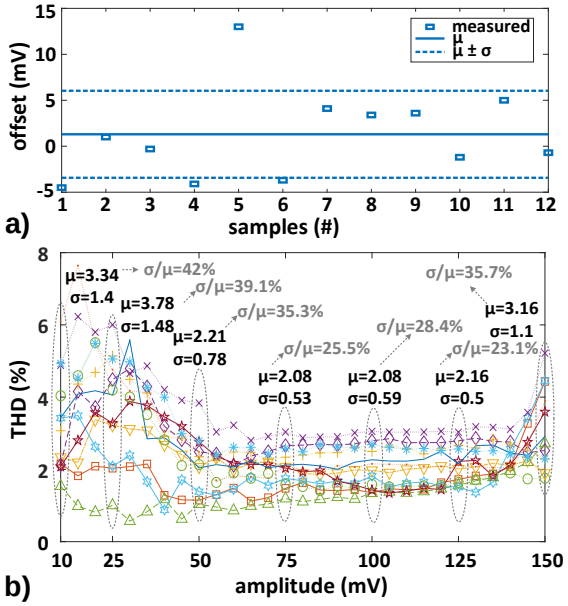

The total harmonic distortion in Fig. 3.19b has a variability of 23.1-25.5%, across the range of moderate to large amplitudes, above 50 mV and up to 125 mV.

From Fig. 3.20, the large-signal and small-signal power efficiency figure of merit has a 23.3% and 29.6% variability, indicating that nearly power efficiency is fairly consistent across process variations.

The DIGOTA performance is compared with state-of-the-art ultra-low-voltage and ultra-low power OTAs in Table 3.2 (see Fig. 3.21). At the supply voltage of 0.3 V, DIGOTA operates at the nW-range power, which is at least an order of magnitude lower than prior art (nor counting DB-OTA). Such power is also efficiently used when driving heavy capacitive loads, as indicated by the small-signal FOM_S=15.6 $MHz \cdot pF/\mu W$, which is 1.5-34X better than prior OTAs operating in the same supply voltage range. As intrinsic limitations of DIGOTA, the DC gain is 19.8-30 dB lower than prior art and the CMRR is accordingly lower by 21.5-37 dB, the PSRR is 8-46 dB lower, and the THD is 1% higher.

The digital nature of DIGOTA reduces the area by 2-85X over prior art (not counting DB-OTA). Combining power and area efficiency, the area-normalized figure of merit $FOM_{S,A}$ in Table 3.2 is improved by >6X. Similarly, the area-normalized large-signal figure of merit $FOM_{L,A}$ is improved by >9X, compared to the prior art in the same supply voltage range.

Figure 3.20: [MEASUREMENTS] Measured figures of merit FOM_S and FOM_L across DIGOTA dice. Power has been measured for sine wave (2.5 Hz input, V_{DD}=0.3 V, C_L=150 pF) .

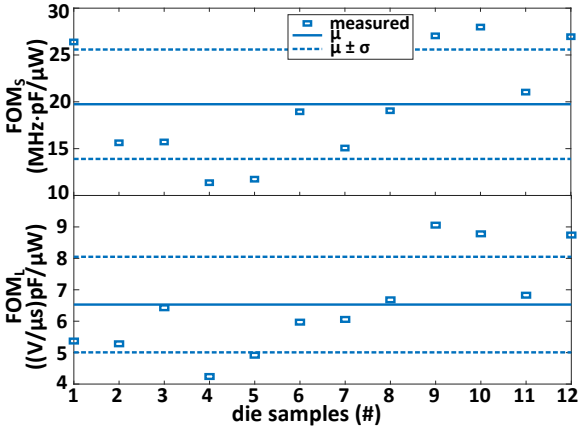

Table 3.2: PERFORMANCE COMPARISON WITH STATE-OF-THE-ART OTAS **(BEST PERFORMANCE IN BOLD)**

	$V_{DD} < 500mV$					$V_{DD} > 500mV$				
	[1]	[2]	[8]	[4]	**This work**	[5]	[6]	[7]	[8]	**This work**
V_{DD} [V]	0.5	0.3	0.25	0.25	0.3	1.1	1.2	2	0.9	0.5
$V_{DD,MIN}$ [V]	0.45	0.3	**0.25**	**0.25**	**0.25**	1.1	1.2	2	0.9	**0.25**
design	custom	custom	custom	custom	**std cell**	custom	custom	custom	custom	**std cell**
OTA architecture	bulk-driven	gate-driven	bulk-driven	bulk-driven	digital	PSS amplifiers	Miller	folded Cascode	bulk-biased	digital
ext. CR needed (Y/N)	Y	**N**	Y	Y	**N**	Y	Y	Y	Y	**N**
technology [nm]	180	130	130	65	180	180	180	500	350	180
area [mm^2]	26,000	-	83,000	2,000	**982**	2,100	13,000	30,000	14,000	**982**
normalized area (10^3F^{-2})	802.47	-	4,911	473	30.3	64.81	401.23	120	114.28	30.3
C_L [pF]	20	2	15	15	150	100	18,000	70	10	150
power [μW]	110	1.8	0.018	0.026	**0.0024**	7.4	69.6	100	18.9	0.1075
DC gain [dB]	52	49.8	60	70	30	**100**	**100**	76.8	65	73
GBW [kHz]	2,500	**9,100**	1.88	9.5	0.25	1,660	1,180	3,400	1,000	57.5
ave. slew rate SR [$V/\mu s$]	2.89	3.8	0.0007	0.002	0.000085	8.67	0.22	**19.25**	0.25	0.019
input noise [μV]	442.7	105.6	143	-	**21**	-	-	42.41	65	122
CMRR [dB]	78	-	-	62.5	41	-	-	**112**	45	65
PSRR [dB]	76	-	-	38	30	-	-	**92**	50	50
THD [%]	1	-	1	-	2	-	-	-	0.2	1
FOM_S	0.45	10	1.6	5.48	15.6	22.4	**305.2**	2.4	0.52	80.2
FOM_L	0.52	4.2	0.58	1.15	5.3	**117.2**	56.9	13.5	0.13	26.5
$FOM_{S,A}$	17.3	-	19	2,750	15,885	10,666	23,477	80	37.15	**81,724**
$FOM_{L,A}$	20.2	-	7	575	5,397	**55,792**	4,377	450	9.45	27,000
passives needed	Y	**N**	Y	Y	**N**	Y	Y	Y	Y	**N**

[1](Chatterjee; Tsividis; Kinget, 2005)+, [2](Lv et al., 2019)*, [3](Ferreira; Sonkusale, 2014)+, [4](WOO; YANG, 2020)+, [5] (HONG; CHO, 2015)+, [6] (QU et al., 2017)+
[7] (GARDE et al., 2018)+, [8] (GRASSO et al., 2017)+,+Experimental, *Simulation

At 0.5 V, the DIGOTA performance improves to 73-dB DC gain, f_{GBW}=57.5 kHz, and 19 V/ms slew rate. The PSRR is increased to 50 dB. Compared to OTAs with much higher supply in the 1.1-2 V range, Table 3.2 shows that DIGOTA still maintains the second-best FOM_S and $FOM_{L,A}$, and the best $FOM_{S,A}$.

Figure 3.21: [MEASUREMENTS] FOM_S and FOM_L energy efficiency: comparison with OTAs with V_{DD}<500mV and V_{DD}>500mV.

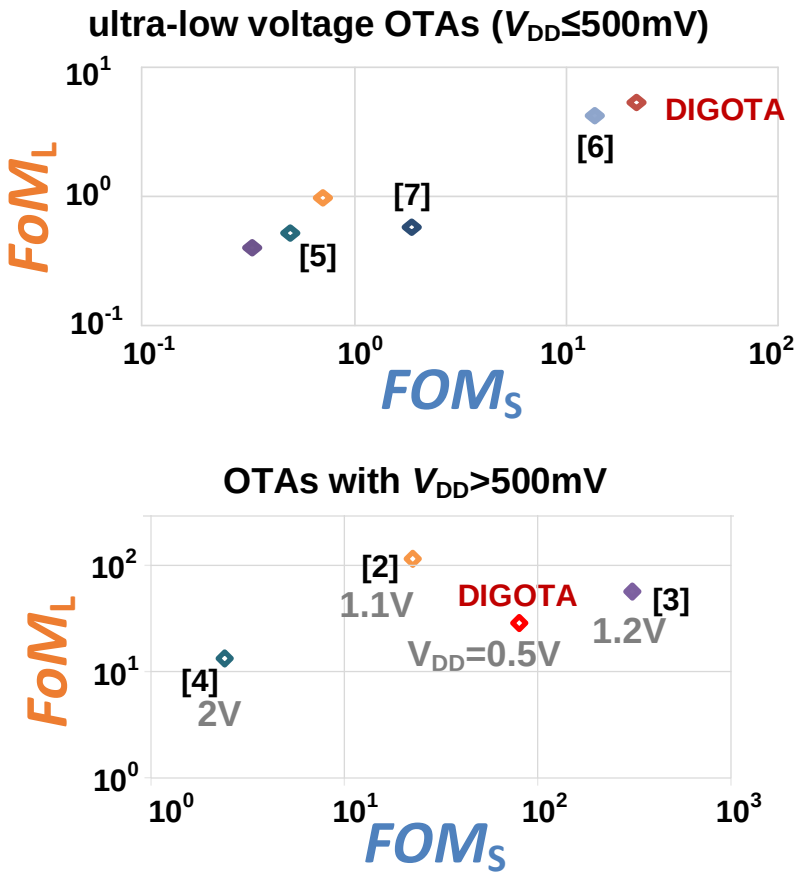

4 DIGITAL-BASED BIOSIGNAL AMPLIFIER

The OTAs presented in chapters 2 and 3 have been mainly conceived to explore the implementation of analog functions by digital blocks and the potential of such an approach. In this chapter, the new concepts are applied in a biomedical signal amplifier. Considering the advantages in terms of area and power, the digital-based design methodology can be valuable in the biomedical field to enable *Body Dust* applications (Carrara, 2020). Being *Body Dust* as one of the biomedical applications which demands the lowest area and power, the DIGOTA is then chosen as a building block to be part of a biomedical amplifier.

Body Dust, which refers to envisioned drinkable, autonomous bio-electronic circuits with dimensions suitable to be internalized into the human body to sense and transmit clinical pieces of information, is emerging as the new frontier of electronics for biomedical applications (CARRARA; GEORGIOU, 2018; Carrara, 2020) (see Fig. 4.1). The concept of Smart Dust has been proposed and investigated in deep over the last 20 years. Even though the very first paper about this subject was presented at a conference held in 1999 (KAHN; KATZ; PISTER, 1999), the first real device was just demonstrated in the body of mammalian in 2016 (SEO et al., 2016). The presented device is still reasonably large with respect to the typical sizes promised in this area of research (typically, sub-mm devices).

Concentrating on the analog signal acquisition, the stringent requirements in terms of low noise and distortion need to be met under ultra-low area, low voltage, and power consumption restrictions. In particular, these constraints are hard to be achieved by analog, and mixed signal circuit design techniques at the state of the art (Zhang; AL., 2013; Mondal; Hall, 2020; Atzeni; AL., 2020; Harpe; AL., 2016; Chen; AL, 2015; Chandrakumar; Marković, 2017; Han; AL., 2013; Yaul; Chandrakasan, 2017). For instance, *Body Dust* ICs for temperature (Shi; AL., 2020), pH (ZHANG et al., 2020) and drugs/biomarkers concentration (Ghoreishizadeh; AL., 2014) monitoring applications demand sub-$0.1\mathrm{mm}^3$ silicon volume (mainly due to its own application nature), which accordingly constrains the available harvested power (state-of-the-art human body-based thermal and vibration energy harvesters offering $7.4\mu\mathrm{W}/\mathrm{cm}^3$ power density (Wahbah; AL., 2014) translate to sub-nW power for 0.1 mm^3 silicon volume. See also Fig. 1.12 for a more general view). In (LIU et al., 2020), Fig. 4.2 illustrates the typical requirements for bio-electronic interfaces.

Figure 4.1: Body dust illustration (CARRARA; GEORGIOU, 2018; Carrara, 2020).

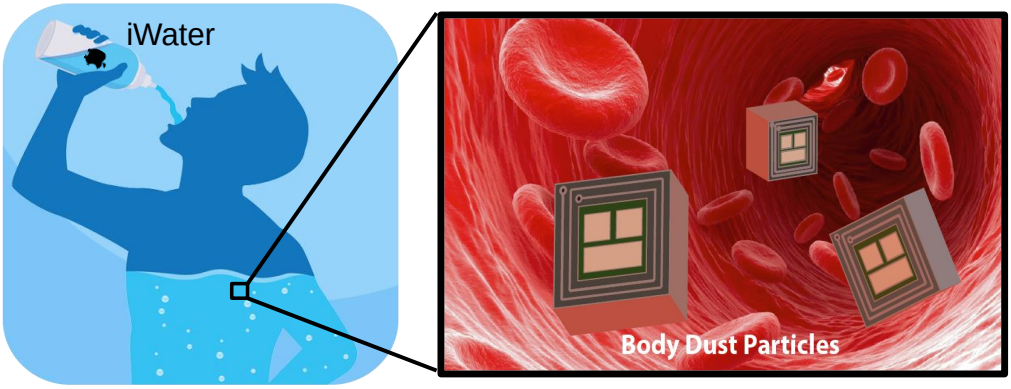

Figure 4.2: Typical requirements for Bioelectronic Interfaces (LIU et al., 2020).

SPECIFICATION		TYPICAL	COMMENT
Recording performance	Noise (μV rms)	< 5	Including both electrode and instrumentation noise
	Bandwidth (Hz)	1–3,000	Broadband to include local-field-potential (LFP) and extracullar action potential (EAP) signals
	dc rejection (mV)	> 100	Offset across different electrodes
	DR (dB)	> 50	Relating to the front-end amplifier, data converter
	CMRR (dB)	> 70	For interference/stimulation artefact suppression
	PSRR (dB)	> 70	Voltage regulation can relax this requirement
	Input impedance (Ω)	> 5M	Large compared to the electrode impedance
Resource per channel	Area (mm^2)	0.01–0.1	To allow for large channel counts
	Power (μW)	10	Limited by heat dissipation in tissue

PSRR: power supply rejection ratio; CMRR: common mode rejection ratio; DR: dynamic range.

In this chapter, a digital-based fully differential amplifier for biomedical signal processing (BioDIGOTA) circuit is proposed based on the single-ended DIGOTA topology of chapter 3. The necessary modifications to achieve fully-differential operation and meet the biosignal acquisition requirements are explored and explained. The DIGOTA concept described in chapter 3 is exploited to design a fully differential biosignal amplifier targeting the requirements of electrocardiogram (ECG) amplification (Zhang; AL., 2013; Mondal; Hall, 2020; Atzeni; AL., 2020; Harpe; AL., 2016; Chen; AL, 2015; Chandrakumar; Marković, 2017; Han; AL., 2013; Yaul; Chandrakasan, 2017), whose schematic is shown in Fig 4.3a and whose design is described next.

The chapter organization follows a similar structure as seen in the previous ones. Circuit analysis and design is shown in section 4.1.1. Its layout is depicted in section 4.2, followed by simulation results in section 4.3, and measurements in section 4.4.

Figure 4.3: a) BioDIGOTA schematic b) Fully differential DIGOTA.

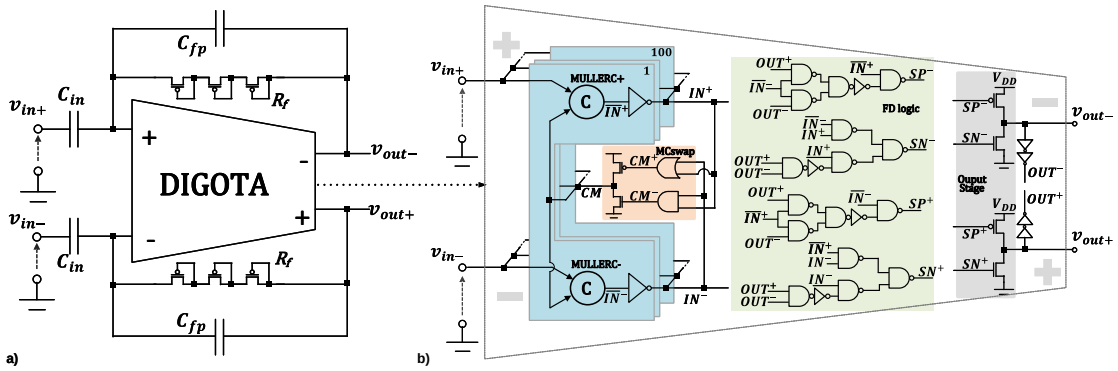

4.1 Circuit Design and Analysis

4.1.1 Circuit Analysis

The proposed fully-Differential (FD) BioDIGOTA includes a FD noise-optimized version of the DIGOTA presented in Chapter 3, as detailed in Fig. 4.3b, and an on-chip capacitive feedback network ($C_{\rm in}$,$C_{\rm fp}$,$R_{\rm f}$ shown in Fig. 4.3a) implemented by Metal-insulator-Metal (MiM) capacitors and MOSFETs as pseudo-resistors.

Aiming to allow FD operation, the proposed FD-DIGOTA includes a Muller-C-based input stage, two inverters, and an MCswap common-mode compensation stage analogous in concept to the corresponding blocks of the single-ended version. But its output stage is now comprised of two three-state inverters so that to generate the positive and negative output voltages $v_{\rm out+}, v_{\rm out-}$.

The two inverters of the BioDIGOTA output stage are digitally operated both to amplify the differential input voltage and to keep the common-mode output voltage constant. For this purpose, they are driven based on the digital signals IN^+, IN^-, equivalent in concept to $(\overline{\rm MUL+}, \overline{\rm MUL-})$ in the single-ended version presented in section 3.1, and based on the additional digital signals OUT^+ and OUT^-, obtained by two digital buffers driven by the analog outputs $v_{\rm out+}$ and $v_{\rm out-}$, respectively, so that OUT^+ (OUT^-), is high or low when the corresponding analog output voltage $v_{\rm out+}$ ($v_{\rm out-}$) is above or below the trip point $V_{\rm T} \simeq V_{\rm DD}/2$. The operation of the two output buffers and of the MCswap stage based on the IN^+, IN^-, OUT^+ and OUT^- digital signals is defined as in the truth table reported in Tab.4.1 and is described next.

Whenever $IN^+ \neq IN^-$ (highlighted in bold in Tab.4.1), the sign of the differential input signal can be detected and amplified, and the output stages are operated ac-

Table 4.1: Fully-Differential DIGOTA Combinational Logic Truth Table

DIGITAL INPUTS				DIGITAL OUTPUTS					
IN^+	IN^-	OUT^+	OUT^-	CM^+	CM^-	SP^+	SN^+	SP^-	SN^-
0	0	0	0	ON	OFF	ON	OFF	ON	OFF
0	0	0	1	ON	OFF	OFF	OFF	OFF	OFF
0	0	1	0	ON	OFF	OFF	OFF	OFF	OFF
0	0	1	1	ON	OFF	OFF	ON	OFF	ON
0	**1**	0	0	OFF	OFF	OFF	ON	ON	OFF
0	**1**	0	1	OFF	OFF	OFF	ON	ON	OFF
0	**1**	1	0	OFF	OFF	OFF	ON	ON	OFF
0	**1**	1	1	OFF	OFF	OFF	ON	ON	OFF
1	**0**	0	0	OFF	OFF	ON	OFF	OFF	ON
1	**0**	0	1	OFF	OFF	ON	OFF	OFF	ON
1	**0**	1	0	OFF	OFF	ON	OFF	OFF	ON
1	**0**	1	1	OFF	OFF	ON	OFF	OFF	ON
1	1	0	0	OFF	ON	ON	OFF	ON	OFF
1	1	0	1	OFF	ON	OFF	OFF	OFF	OFF
1	1	1	0	OFF	ON	OFF	OFF	OFF	OFF
1	1	1	1	OFF	ON	OFF	ON	OFF	ON

cordingly. In details, if $IN^+ = 1$ and $IN^- = 0$ ($IN^+ = 0$ and $IN^- = 1$), the pull-up device of the buffer driving the non-inverting (inverting) output is operated, whereas the pull-down device of the buffer driving the inverting (non-inverting) output is operated, so that to increase (decrease) the differential output component $v_{\mathrm{d,out}} = v_{\mathrm{out}+} - v_{\mathrm{out}-}$, regardless the OUT^+ and OUT^- values. In the meantime, the MCswap block is kept inactive (i.e., in a high impedance state).

On the other hand, when $IN^+ = IN^-$ and the sign of the differential input signal cannot be detected, the *MCSwap* stage is activated as in the single-ended DIGOTA circuit, and the output common mode signal is also corrected, if needed. In particular, when $OUT^+ = OUT^- = 0$ ($OUT^+ = OUT^- = 1$), the *output stages* are activated so that to increase (decrease) both the output voltages $v_{\mathrm{out}+}$ and $v_{\mathrm{out}-}$ at the same time, as needed to enforce a common-mode output voltage closer to $V_{\mathrm{DD}}/2$. By contrast, whenever $OUT^+ \neq OUT^-$, which implies that the CM output voltage differs from $V_{\mathrm{DD}}/2$ by less than one half of the output differential signal $v_{\mathrm{d,out}}$, both the output stages are kept in a high impedance state.

In essence, from the truth table 4.1 it is observed that whenever IN^+ and IN^- are logically equal, the input common-mode is always compensated as in the single-ended DIGOTA circuit, whereas the output common-mode component is either increased or

decreased if OUT^+ and OUT^- are (0,0) or (1,1), and CM output stage is kept at high impedance only when OUT^+ and OUT^- is (1,0) or (0,1). For the sake of completeness, the Boolean equations for each gate of each output stage are:

$$SP^+ = \overline{IN^+} \cdot OUT^+ + IN^- + \overline{IN^+} \cdot OUT^- = \overline{\overline{IN^+ \cdot OUT^+} \cdot \overline{IN^-} \cdot \overline{IN^+ \cdot OUT^-}} \tag{4.1}$$

$$SN^+ = \overline{IN^+} \cdot IN^- + IN^- \cdot OUT^+ \cdot OUT^- = \overline{\overline{IN^+ \cdot IN^-} \cdot \overline{IN^- \cdot OUT^+ \cdot OUT^-}} \tag{4.2}$$

$$SP^- = \overline{IN^-} \cdot OUT^+ + IN^+ + \overline{IN^-} \cdot OUT^- = \overline{\overline{IN^- \cdot OUT^+} \cdot \overline{IN^+} \cdot \overline{IN^- \cdot OUT^-}} \tag{4.3}$$

$$SN^- = \overline{IN^-} \cdot IN^+ + IN^+ \cdot OUT^+ \cdot OUT^- = \overline{\overline{IN^- \cdot IN^+} \cdot \overline{IN^+ \cdot OUT^+ \cdot OUT^-}} \tag{4.4}$$

In the case of CM^+ and CM^-, they follow the same logic as given by Eqs. (2.4) and (2.5), respectively.

4.1.2 Circuit Design

For biosignal amplification, the noise generated by the DIGOTA must be reduced. Then a noise-optimized version of DIGOTA should be designed. Based on the modeling approach adopted for the single-ended DIGOTA circuit in chapter 3 and assuming the circuit is working in weak inversion (Low $V_{\mathrm{DD}}s$), the DIGOTA noise performance is dominated by the shot noise from the input devices within the Muller-C stage, where the in-band integrated input noise is given by

$$\overline{v_{\mathrm{IN}}^2} = 2\pi \frac{2qI_{CM}}{g_m^2} f_{BW} \tag{4.5}$$

where q is the electrical charge, I_{CM} is defined in Eq. (3.9), g_m is the muller-C weighted transconductance defined in (3.10), and f_{BW} is the amplifier bandwidth.

The Noise Efficiency Factor (NEF), described in Eq. (4.6), is a well-known metric to quantify the performance of low noise amplifiers for biomedical applications (LIU et al., 2020).

$$NEF = v_{\mathrm{IN,RMS}}\sqrt{\frac{2I_{\mathrm{D}}}{\phi_{\mathrm{T}}4k_{\mathrm{B}}T\pi f_{BW}}} \tag{4.6}$$

where ϕ_{T} is the thermal voltage, k_{B} is the Boltzmann constant, T is the temperature, and I_{D} is current consumption.

Once the DIGOTA is designed to reduce the total noise, most of the power is consumed in the first stage ($I_D \approx I_{CM}$) given by Eq. (4.7) and its g_m is given by Eq. (4.8) for weak inversion regime.

$$I_D = \frac{Power}{V_{DD}} = \frac{2C_{MUL}V_{DD}}{T_0} \tag{4.7}$$

$$g_m = \frac{I_D}{n\phi_T} \tag{4.8}$$

Substituting Eqs (3.8) for $\tau_{INV} = \tau_{MCswap} = 0$, (4.7) and (4.8) in (4.5) and after in (4.6), we have

$$NEF_{DIGOTA} \approx n \tag{4.9}$$

Fig. 4.4 compares NEF and the power efficiency factor $PEF = NEF^2V_{DD}$ of current state of the art of low frequency and low noise CMOS amplifier solutions. Among them, the discrete-time low-noise amplifier made by switched-capacitors achieves the best NEF and PEF at the cost of a big silicon area (Atzeni; AL., 2020). In (Mondal; Hall, 2020), current reused is implemented to increase the equivalent transconductance by N stacked inverters and, then, the final NEF is reduced by $\sqrt{N}$. However, the later of approach limits the minimum V_{DD}. In the case of the proposed BioDIGOTA, the NEF is equivalent to the stacked inverters for $N = 1$, but no any bias circuit is needed, the circuit is compatible to digital flow, and the total silicon area is further reduced.

4.2 Layout

The proposed FD BioDIGOTA has been designed and fabricated in 180nm CMOS, and its layout is shown in Fig. 4.5 along with its micro-photo. Once most of the noise

Figure 4.4: a) NEF and PEF for differential pair, b) for stacked inverter-based (Mondal; Hall, 2020), c) Switched-capacitor (Atzeni; AL., 2020), and d) digital based amplifier of section 2.

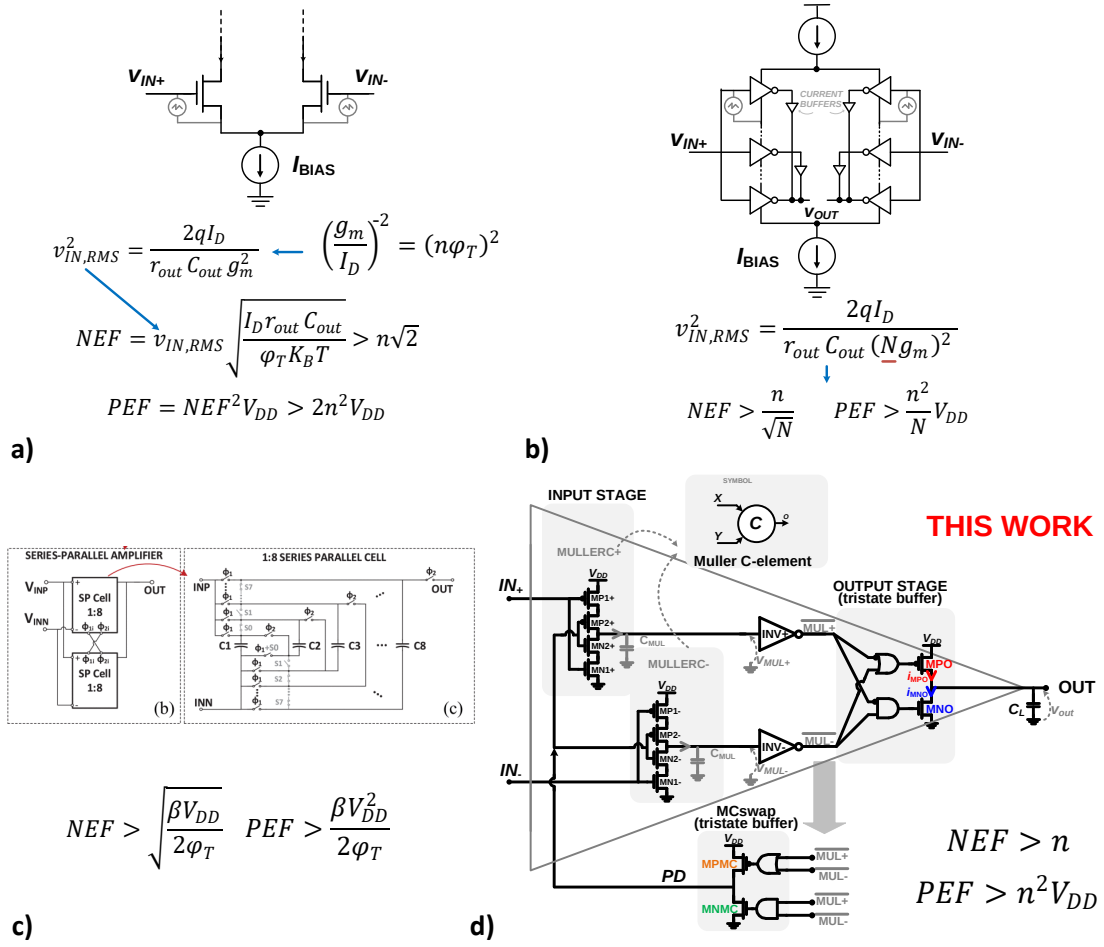

contribution is related to the input stage, its design has deserved special care to meet the requirements of biomedical signal amplification. For this purpose, the area of the Muller-C is increased one hundred times to reduce noise by connecting one hundred cells in parallel.

The delays of the non-inverting and inverting signal paths have been matched. The active components have been integrated under the MiM capacitors to reduce the layout area further. The circuit layout occupies just 0.022 mm^2, thus achieving 3.322X lower silicon area compared to the minimum size found in the current literature (Chandrakumar; Marković, 2017). In Fig. 4.5, the area breakdown shows that the MullerC logic-gates occupy more than 50% of the area. At the same time, almost 40% of the total is covered by the MiM capacitors of the feedback network. In other words, only 0.018 of 0.022 mm^2 are dedicated to the active devices, including the pseudo-resistors.

Figure 4.5: BioDIGOTA final layout in CMOS 180nm and chip picture.

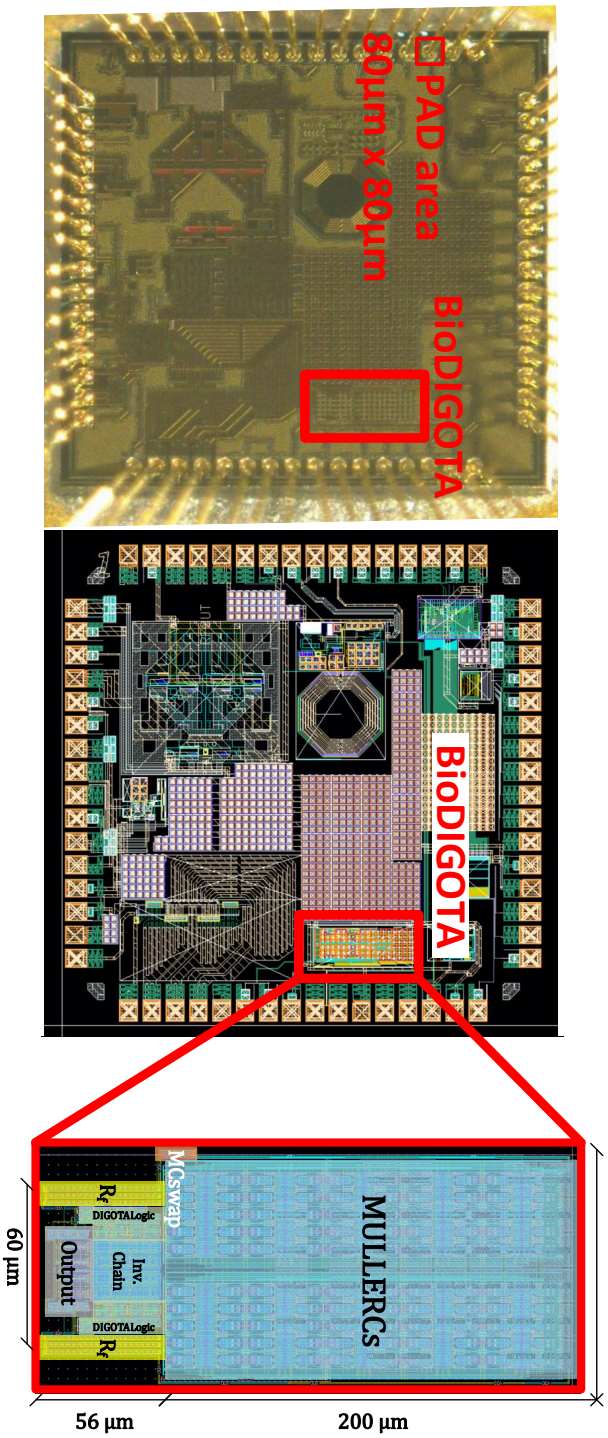

4.3 Simulations Results

The time-domain input and output waveforms of the proposed BioDIGOTA at $V_{\mathrm{DD}} = 300\mathrm{mV}$, with sine wave input at 40Hz frequency, 100 μV peak amplitude and $C_{\mathrm{out}} = 20\,\mathrm{pF}$ capacitive load are reported in Fig.4.6 and reveal the operation of the

Figure 4.6: [SIMULATIONS] a) BioDIGOTA transient response. b) Wide spectrum density for output signal from b) for input amplitude of 100 μV at 40 Hz.

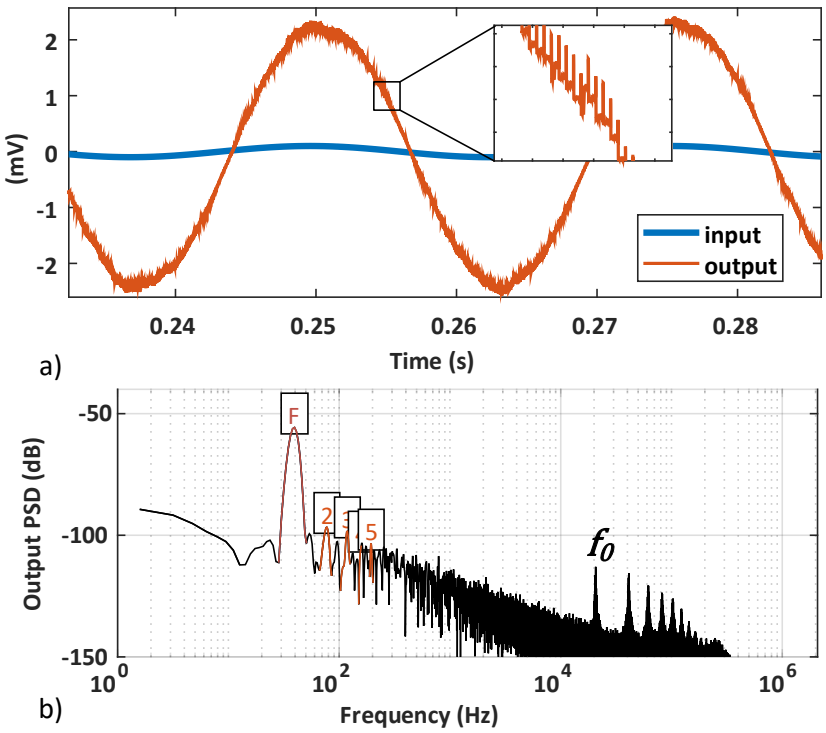

Figure 4.7: [SIMULATIONS] BioDIGOTA frequency response.

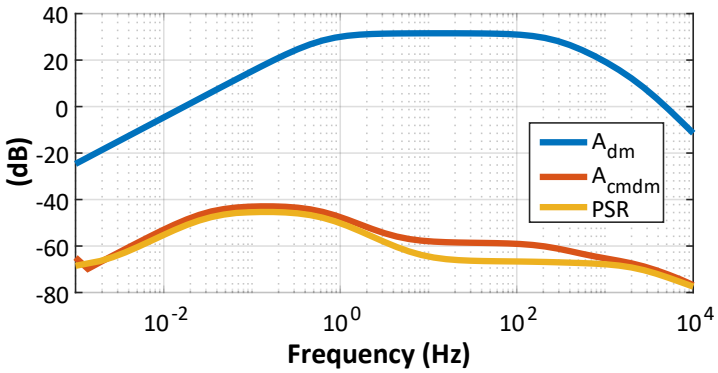

circuit as an opamp with less than 2% THD and 150nW of power consumption. A zoom in the output waveform shows the step-wise changes in v_{out} resulting from its intrinsically digital operation (Toledo et al., 2019; Crovetti, 2013; Toledo et al., 2020). The wideband output spectrum is reported in Fig.4.6b, revealing in-band harmonics (THD=1.5%) and the out-of-band self-oscillation frequency tone at $f_0 \approx 18$kHz.

The circuit frequency response and noise power spectral density (PSD) have been verified by PSS+PAC+PNoise analysis (Kundert, 1999) in view of its circuit digital operation, where its linearization is performed around its natural self-oscillation frequency

Figure 4.8: [SIMULATIONS] BioDIGOTA Noise spectrum density.

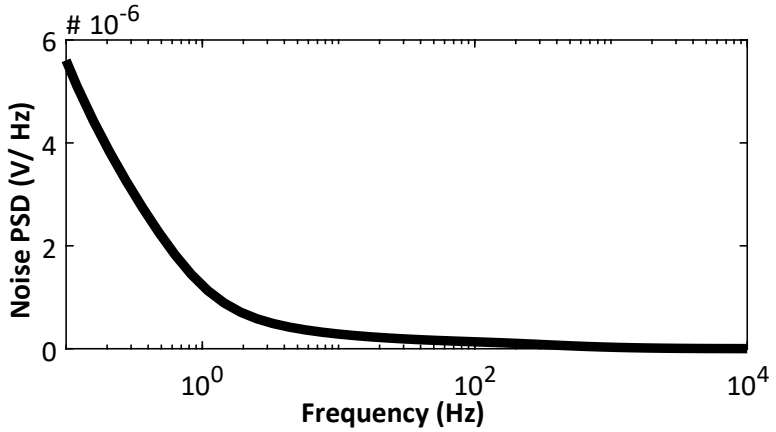

Figure 4.9: [SIMULATIONS] THD Histogram (μ=5.13% and σ=1.74%) for N=100 samples and input amplitude of 100 μV.

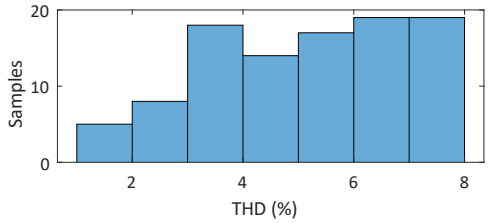

Figure 4.10: [SIMULATIONS] Integrated Noise Histogram (μ=1.97μV_{RMS} and σ=0.813μV_{RMS}) for N=100 samples and BW from 0.01Hz to 10kHz.

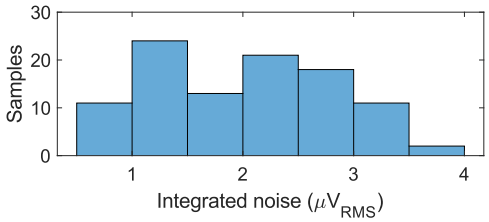

f_0. The ULV BioDIGOTA frequency response reported in Fig.4.7 exhibits 30dB in-band gain and 270 Hz bandwidth (BW) under $C_{\mathrm{out}} = 20\mathrm{pF}$ load. In the same plot, the common mode to differential mode (CM-DM) frequency response along with PSR are also depicted showing a CMRR and PSRR of 77 and 80 dB, respectively. Fig. 4.8 shows the power spectral density of the input-refereed noise, revealing an integrated noise of 3.1 μV_{RMS} over the BW from 0.01Hz to 10kHz or 31 nV/$\sqrt{Hz}$ average PSD over the same BW.

Before the tapeout, the BioDIGOTA has been verified under process variations for $V_{\mathrm{DD}} = 300mV$ by Montecarlo (MC) simulations performed on 100 samples and the output THD has been considered in order to evaluate the signal quality degradation. The output THD for an input amplitude of 100 μV histogram reported in Fig.4.9 reveals a mean value of $\mu = 5.13\%$ and standard deviation of $\sigma = 1.74\%$, i.e., $\frac{\sigma}{\mu} = 34\%$.

Figure 4.11: [SIMULATIONS] Power Histogram (μ=146nW and σ=29nW) for N=100 samples.

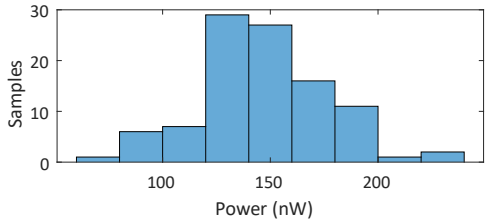

Figure 4.12: [SIMULATIONS] Gain Histogram (μ=28.2dB and σ=1.13dB) for N=100 samples.

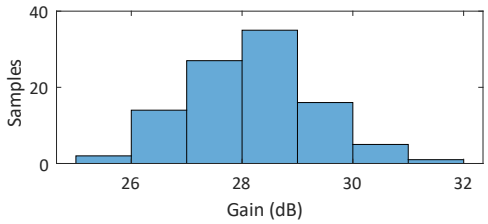

Noise is also an relevant specification for low bio-potential signals and the integrated noise histogram is plotted in Fig. 4.10, achieving $\frac{\sigma}{\mu} = 41\%$. Power and middle-band gain histograms are also reveled in Fig. 4.11 and 4.12, reaching $\frac{\sigma}{\mu} = 20.1\%$ and $\frac{\sigma}{\mu} = 4\%$, respectively.

4.4 Measurements Results

Three BioDIGOTA samples have been measured, and their performance has been compared with biosignal amplifiers presented in recent literature. The 3Hz frequency time-domain input and output measured waveforms of the proposed FD BioDIGOTA at $V_{\mathrm{DD}} = 400\mathrm{mV}$ and $C_{\mathrm{out}} = 10\,\mathrm{pF}$ capacitive load are reported in Fig.4.13b and reveal the operation of the circuit as a filter with less than 2% THD and 100nW power consumption for an input amplitude of 3.5 mV. A voltage gain of 35 dB has been estimated for this configuration. The power breakdown is also included in the Fig.4.13a. A relevant power is consumed in the first stage, as expected, to reduce the noise. The wide-band output spectrum is reported in Fig.4.13c, revealing in-band harmonics (THD=1.8%). Table 4.2 shows THD measured for all three samples.

The measured frequency response of the BioDIGOTA differential amplification is reported in Fig.4.14a and reveals 35dB in-band gain and $10\,\mathrm{Hz}$ bandwidth under $C_{\mathrm{out}} = 10\mathrm{pF}$ load. In the same plot, the common-mode rejection ratio (CMRR) and the power supply rejection ratio (PSRR) are also depicted, revealing a CMRR exceeding 62dB and

Figure 4.13: a) Area breakdown and power breakdown of BioDIGOTA b) input and output waveforms and c) Wide spectrum density for output signal for input amplitude of 3.5 mV at 3 Hz.

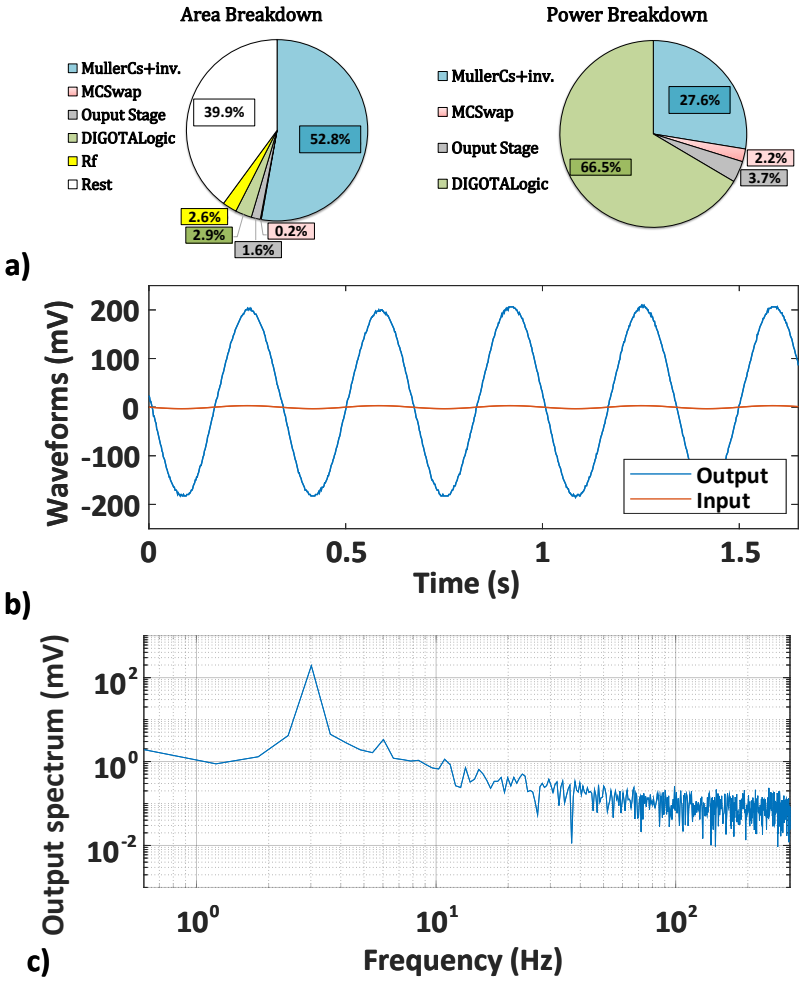

a PSRR exceeding 55 dB in the signal bandwidth for the best sample (sample #3).

Fig.4.15 shows the measured power spectral density of the input-refereed noise for the three samples. The BioDIGOTA integrated noise over the entire bioDIGOTA bandwidth (0.05 Hz - 10 Hz specify the bandwidth here) is 1.25μV_{RMS}, corresponding to a 395 nV/$\sqrt{\mathrm{Hz}}$ average PSD over the same bandwidth for sample #3. Power, NEF, and PEF are listed for all samples in Table 4.2. Amongst all samples, the lowest NEF and PEF found are 7.6 and 23, respectively, for the sample #3.

Compared to biosignal amplifiers proposed in recent literature (Zhang; AL., 2013; Mondal; Hall, 2020; Atzeni; AL., 2020; Harpe; AL., 2016; Chen; AL, 2015; Chandrakumar; Marković, 2017; Han; AL., 2013; Yaul; Chandrakasan, 2017), whose performance is summarized in Tab. 4.3, the BioDIGOTA presented here is able to work properly at the lowest V_{DD} (2X lower than (Harpe; AL., 2016; Chen; AL, 2015)), at the lowest sili-

Table 4.2: Measured performance for all three samples @ V_{DD} =400mV, 27 ^{o}C temperature, input amplitude of 3.5mV and frequency of 3 Hz.

Sample Number #	THD (%)	Power (nW)	Gain (dB)	Noise (μV_{RMS})	NEF	PEF
1	1.7	100.84	34.3	2.52	15.69	98.49
2	1.25	78.63	36.84	2.13	11.73	55
3	**1.8**	**95**	**35**	**1.25**	**7.59**	**23**

The measured results of sample #3 (bold) are also presented in the comparison table (Table 4.3).

Figure 4.14: Gain, CMRR and PSRR at $V_{\mathrm{DD}} = 400mV$.

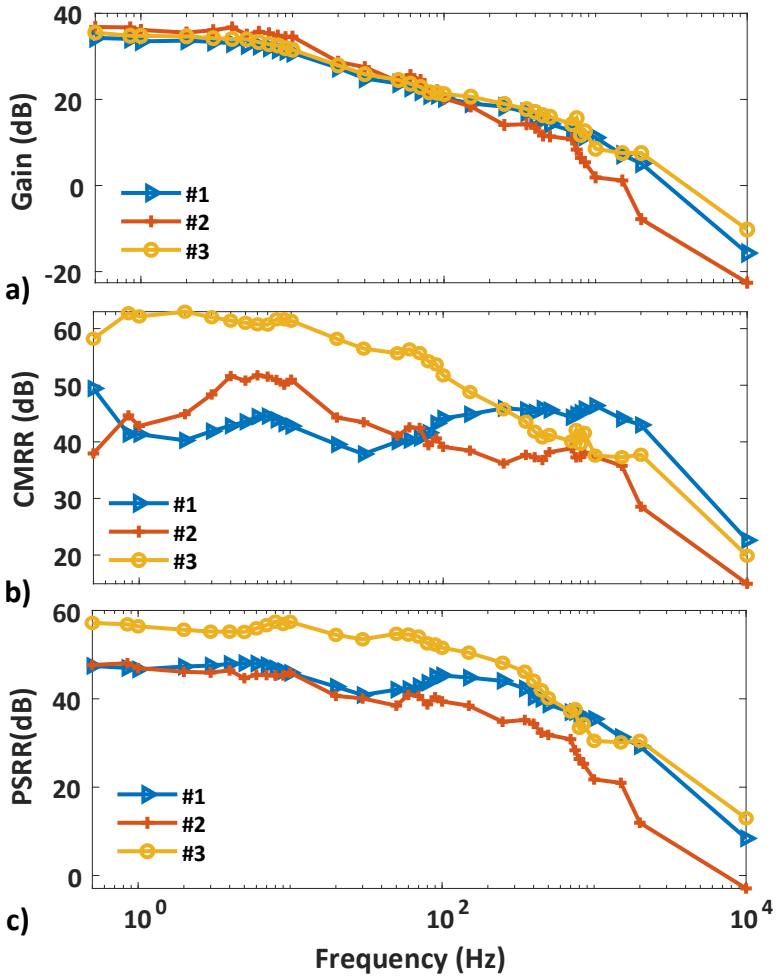

con area (3.22X lower than (Chandrakumar; Marković, 2017)), keeping acceptable noise performance. These results prove that digital-based analog design is very attractive for body dust applications. The comparison in terms of NEF and PEF versus area is also illustrated in Fig. 4.16. If the NEF and PEF are both multiplied by the total area as shown in Tab. 4.3 by NEF_{AREA} and PEF_{AREA}, the proposed BioDIGOTA achieves the lowest NEF_{AREA}. These measurements results gathered from the proposed BioDIGOTA demonstrate a relevant power-efficiency and area reduction, as previously predicted in Fig. 1.17b.

Figure 4.15: BioDIGOTA measured noise spectrum density for each sample over entire bandwidth at $V_{\mathrm{DD}} = 400mV$.

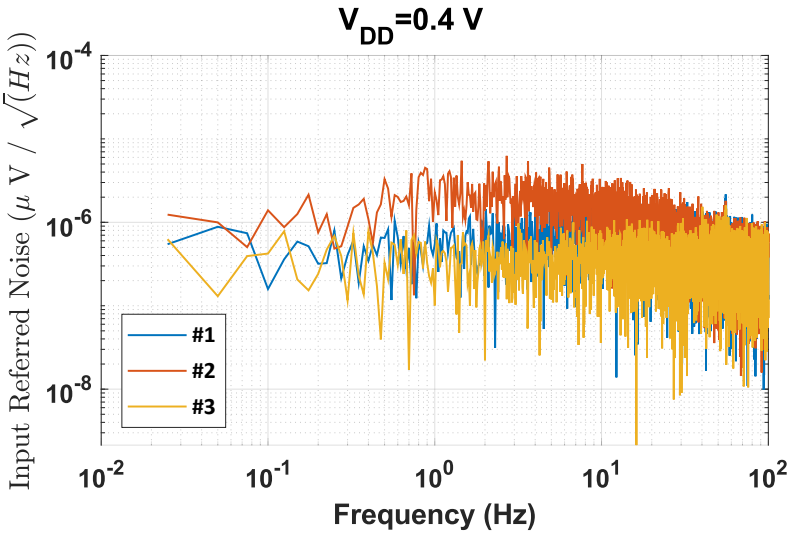

Figure 4.16: NEF and PEF versus Area.

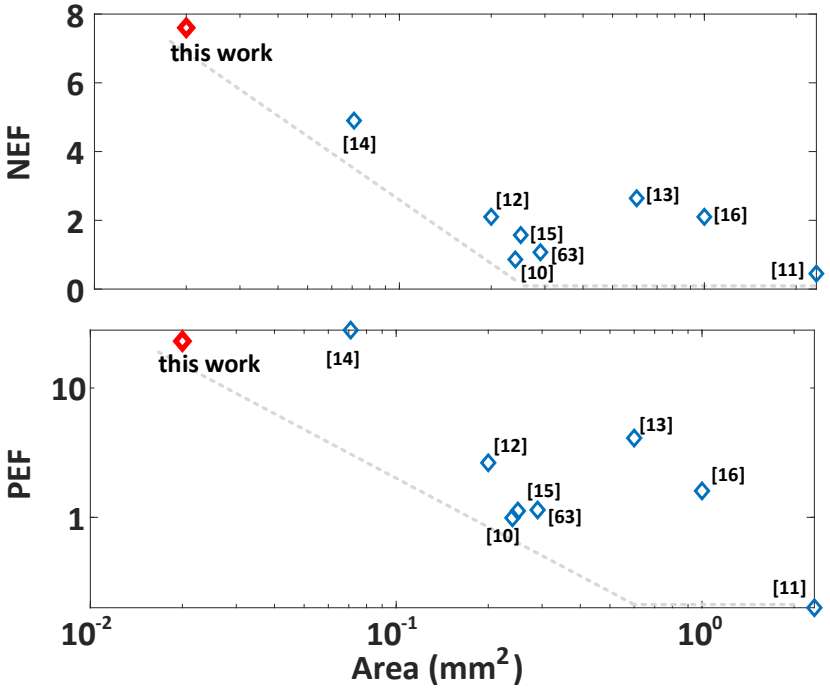

Table 4.3: Performance Summary and Comparison **(BEST PERFORMANCE IN BOLD)**

Performance	(Yaul; Chandrakasan, 2017)	(Harpe; AL., 2016)	(Chen; AL., 2015)	(Shen; Lu; Sun, 2018)	(Han; AL., 2013)	(Chandrakumar; Marković, 2017)	(Mondal; Hall, 2020)	(Atzeni; AL., 2020)	(VALTIERRA et al., 2020)	(CABRERA et al., 2021)	**This work***	Unit
Design strategy	Analog	Analog	Analog	Analog	Analog	Analog	Analog	Analog	Analog	Analog	**Digital**	-
Technology	180	65	65	180	180	40	180	180	180	130	180	nm
Supply Voltage	0.2/0.8	0.6	0.6	1	0.45	1.2	1.35	1	1	1.2	**0.4**	V
Die Area	1	0.2	0.6	0.29	0.25	0.071	0.24	2.33	0.19	0.1	**0.022**	mm^2
Power	790	**1**	16.8	250	730	2,000	18.7	620	800	35,800	95	nW
Gain	58	32	**51-96**	25	52	26	36	22.3	40.4	39.3	35	dB
BW	670	370	250	10,000	10,000	5,000	240	5,000	5,000	**100,000**	10	Hz
CMRR	85	60	80	84	73	-	**95**	91.8	58	86	62	dB
PSRR	74	63	67	76	80	-	68	**83**	54	67	55	dB
THD	0.3	-	2.8	-	0.53	**0.02**	0.16	0.025	1	1	1.8	%
Input-Referred Noise	36	1,400	253	43	29	40	158	**11.85**	59.18	13	395	$nV/\sqrt{Hz}$
NEF	2.1	2.1	2.64	1.07	1.57	4.9	0.86	**0.45**	2	2.5	7.6	-
PEF	1.6	2.64	4.1	1.14	1.12	28	0.99	**0.2**	4	7.5	23	V
$NEF_{AREA} = NEF \times Area_{mm^2}$	2.1	0.42	1.58	0.31	0.39	0.35	0.2064	1.045	0.38	0.25	**0.15**	mm^2
$PEF_{AREA} = PEF \times Area_{mm^2}$	1.6	0.528	2.46	0.33	0.28	1.98	**0.238**	0.466	0.76	0.75	0.46	$V \cdot mm^2$

5 CONCLUSION

Despite the intrinsically analog and smooth perception of our surrounding environment, the achievements of science and technology in the last two centuries have extensively shown that in-depth analysis, which appears to be continuous, proves to be discrete in various forms. The matter is composed of atoms, and all fundamental physical quantities from electric charge to electromagnetic field and angular momentum are also quantized. Not only the inanimate world proves to be discrete, but also in animals and humans. Their information is processed and transmitted as discrete pulses, as discovered and modeled by Hodgkin and Huxley (HODGKIN; HUXLEY, 1952). Then, we may conclude that our everyday life analog feeling is based on an underlying discrete structure.

C.E.Shannon, in his groundbreaking work (Shannon, 1948), shows that the *information* is discrete in itself. The maximum amount of data that can be reliably transferred in the unit time (expressed in bit/s) is finite and upper-bounded by the channel capacity $C = B \log_2 (1 + S/N)$ (Shannon, 1948), regardless of whether analog signals or digital signals are adopted. Shannon's reasoning, however, does not apply just to computers and communication networks. They also suit any kind of information, including information processed in sensors, actuators, interfaces, and analog circuits like OTAs and voltage references. This thesis suggests that even these circuits could better understand the discrete nature of information and that digital circuits can perform their functions.

The thesis claims that a "digital revolution" in analog blocks is now happening, and it can be clearly observed in recent publications appearing in analog blocks ranging from PLLs to voltage references. This shift in the analog/RF design approach is here defined as **Digital-in-Concept Design Methodologies (DCDM)** trend. Furthermore, the thesis demonstrates that the DCDM approach is significantly attractive to IoT applications, coping with two crucial challenges of the next-generation IoT ecosystem: silicon area and power consumption on the edge devices. Such challenges are deeply investigated in chapter 1, examining the entire IoT technological stack and its applications.

Taking advantage of information processing in time domain and digital automated design techniques related to DCDM, two digital OTAs and a bio-signal amplifier have been proposed and validated in silicon.

As the first contribution, silicon demonstration, measurement results, and a qualitative circuit analysis have been presented for a highly digital, ultra-low voltage, and

ultra-low power OTA (DB-OTA). By processing the analog input signal digitally via conventional standard cells, the measured power efficiency achieved at V_{DD}=300 mV is quantified by the classical FOM_S figure of merit to be 2,101 V^{-1}, which outperforms the state of the art thanks to the lowest power of 591 pW. DB-OTA measurements also show DC gain and gain-bandwidth between 29 and 31 dB and 229 and 528 Hz, respectively, for 80pF of output load, always keeping THD below 3%. Its area of 1,426 μm^2 is also close to best-in-class. To the best of this thesis author's knowledge, DB-OTA is the first and only sub-nW OTA to date.

Next, a compact and energy-efficient passive-less digital OTA has been proposed and demonstrated in 180 nm. The proposed DIGOTA exhibits a power 2.4nW power consumption (one of the lowest in the literature) and the lowest area (982 μm^2) , and operates down to 250 mV, even if its dc gain, PSRR, CMRR and bandwidth are lower compared to other ultra-low voltage OTAs. At 300 mV, the best figure of merits (such as $FOM_{S,A}$ and $FOM_{L,A}$) are achieved among sub-500-mV OTAs thanks to the improved energy and area efficiency, reaching DC gain and gain-bandwidth of 30 dB and between 200 and 350 Hz for 150pF of output load, respectively. At 500-mV supply, the energy efficiency is still competitive with the previously proposed OTAs operating at above 1-V supplies. The ability to operate at ultra-low voltage and power has been demonstrated in the context of energy-autonomous sensor nodes, as directly powered by a small energy harvester (7 mm^2 solar cell) at dim light <100 lux (dark overcast day).

The BioDIGOTA, i.e. a fully differential digital-based OTA targeting biomedical signal acquisition, is finally presented in this thesis. Such a front-end shows a lower silicon area than its analog counterpart when operating in ULV and ULP conditions. The proposed BioDIGOTA architecture can be implemented using CMOS digital standard cells, available in any fabrication process. The proposed ULV BioDIGOTA has achieved at $V_{\mathrm{DD}} = 400\,\mathrm{mV}$ a good figure of merits (such as $\mathrm{NEF} = 7.6$ and $\mathrm{PEF} = 23$), while consuming just 95 nW and 0.022 mm^2 of silicon area with 35 dB gain and 395 nV/$\sqrt{\mathrm{Hz}}$ power spectral density. Through this implementation, digital-based analog design has been proven to be a good alternative for reducing area, power, and design effort for IoT applications like body dust working in the low voltage domain.

5.1 Future work

There is undoubtedly much work to be done in DCDM or digital-based analog processing: from the architecture perspective to the building block point of view. As shown in Fig. 1.16, digital-based analog and RF processing has become an emerging area of research, and its advantage in the area and power consumption has been showing appealing in IoT applications. Based on the building blocks designed in this thesis, this thesis author lists below some further research challenges to be addressed in future work:

- both proposed digital OTAs have low DC gain as their major drawback. Multi-stage architectures and/or custom output stage, containing for instance Composite Transistors (CT) (RODOVALHO; RODRIGUES; AIELLO, 2021) structures, can be used to boost the final DC gain. Note that the later strategy does not fit into standard-cell-based flow;
- the herein proposed OTAs could be included in several analog systems (e.g., continuous-time sigma-delta ADC (Lv et al., 2019)), not only using the static CMOS family as used here but using other types like Schmitt-Trigger Logic (LOTZE; MANOLI, 2012);
- emerging semiconductor devices (flexible technologies, for instance) or ultra-scaled FinFETs or GAAFETs could be used to design digital OTAs and compare with the traditional approach. Their scaliability and reconfigurability could also be investigated;
- from the design flow and EAD perspective, even though the OTAs are digital design flow compatible, they will be used as a building block of a complete analog system, which likely would contain passive devices requiring certain symmetry constraints and requirements. To include such components and rules, the author of the thesis envisions a near future the union between the current automated analog layout synthesis (ALS) (EICK et al., 2011; FERREIRA et al., 2016; LIN et al., 2016; GRAEB, 2012; LIU et al., 2020; CHEN et al., 2021; DHAR et al., 2021; CROSSLEY et al., 2013) with the current digital design flow, at which mainly guided by digital flow the main building blocks would be standard-cell-based and ALS would be responsible for completing the rest of analog system. In other words, ALS would be included as a feature within the digital design flow backed up by several digital-based analog building blocks, like the ones presented here;

- from a simulation and verification point of view, an analog block/system will always need to be verified using an analog solver once their input and output signal must be continuously monitored to check their final performance. The author of this thesis does not see any improvements to decrease the simulation time of digital-based analog blocks compared to the pure digital ones, where a digital simulator can be used to speed up the verification and static time analysis (STA) to verify the reliability of the circuit.

REFERENCES

ADVISER, U. G. C. S. **Overview of the Internet of Things. Technical Report**. 2014. Https://www.gov.uk/government/publications/internet-of-things-blackett-review.

Aiello, O.; Crovetti, P.; Alioto, M. Fully Synthesizable, Rail-to-Rail Dynamic Voltage Comparator for Operation down to 0.3 V. In: **2018 IEEE International Symposium on Circuits and Systems (ISCAS)**. [S.l.: s.n.], 2018. p. 1–5.

Aiello, O.; Crovetti, P.; Alioto, M. Standard Cell-Based Ultra-Compact DACs in 40-nm CMOS. **IEEE Access**, v. 7, p. 126479–126488, 2019.

Aiello, O.; Crovetti, P.; Alioto, M. Ultra-Low Power and Minimal Design Effort Interfaces for the Internet of Things: Invited paper. In: **2019 IEEE International Circuits and Systems Symposium (ICSyS)**. [S.l.: s.n.], 2019. p. 1–4.

Aiello, O.; Crovetti, P.; Alioto, M. Fully Synthesizable Low-Area Analogue-to-Digital Converters With Minimal Design Effort Based on the Dyadic Digital Pulse Modulation. **IEEE Access**, v. 8, p. 70890–70899, 2020.

Aiello, O. et al. A pW-Power Hz-Range Oscillator Operating With a 0.3–1.8-V Unregulated Supply. **IEEE Journal of Solid-State Circuits**, v. 54, n. 5, p. 1487–1496, 2019.

Aiello, O.; Crovetti, P. S.; Alioto, M. Fully Synthesizable Low-Area Digital-to-Analog Converter With Graceful Degradation and Dynamic Power-Resolution Scaling. **IEEE Transactions on Circuits and Systems I: Regular Papers**, v. 66, n. 8, p. 2865–2875, 2019.

AITKEN, R. How To Build A Trillion Connected Things. In: **semiengineering.com**. [S.l.: s.n.], 2017.

AL-FUQAHA, A. et al. Internet of Things: A Survey on Enabling Technologies, Protocols, and Applications. **IEEE Communications Surveys Tutorials**, v. 17, n. 4, p. 2347–2376, 2015.

ALIOTO, M. Ultra-Low Power VLSI Circuit Design Demystified and Explained: A Tutorial. **IEEE Transactions on Circuits and Systems I: Regular Papers**, v. 59, n. 1, p. 3–29, 2012.

ALIOTO, M. **Enabling the Internet of Things – from Integrated Circuits to Integrated Systems**. First. [S.l.]: Springer, 2017.

ALIOTO, M. From Less Batteries to Battery-Less Alert Systems with Wide Power Adaptation down to nWs—Toward a Smarter, Greener World. **IEEE Design Test**, v. 38, n. 5, p. 90–133, 2021.

ALIOTO, M.; DE, V.; MARONGIU, A. Energy-Quality Scalable Integrated Circuits and Systems: Continuing Energy Scaling in the Twilight of Moore's Law. **IEEE Journal on Emerging and Selected Topics in Circuits and Systems**, v. 8, n. 4, p. 653–678, 2018.

ALIOTO, M.; SHAHGHASEMI, M. The Internet of Things on Its edge: Trends Toward Its Tipping Point. **IEEE Consumer Electronics Magazine**, v. 7, n. 1, p. 77–87, 2018.

Ansari, E.; Wentzloff, D. D. A $5\mathrm{mW}$ $250\mathrm{MS/s}$ 12-bit synthesized digital to analog converter. In: **Proceedings of the IEEE 2014 Custom Integrated Circuits Conference**. [S.l.: s.n.], 2014. p. 1–4.

Atzeni, G.; AL. et. A 0.45/0.2-NEF/PEF 12-nV/$\sqrt{Hz}$ Highly Configurable Discrete-Time Low-Noise Amplifier. **IEEE Solid-State Circuits Letters**, v. 3, p. 486–489, 2020.

ATZORI, L.; IERA, A.; MORABITO, G. The Internet of Things: A survey. **Computer Networks**, v. 54, n. 15, p. 2787–2805, 2010. ISSN 1389-1286. Disponível em: <https://www.sciencedirect.com/science/article/pii/S1389128610001568>.

Bang et al., S. 25.1 A Fully Synthesizable Distributed and Scalable All-Digital LDO in 10nm CMOS. In: **2020 IEEE International Solid- State Circuits Conference - (ISSCC)**. [S.l.: s.n.], 2020. p. 380–382.

BANOS, O. et al. The Mining Minds digital health and wellness framework. **BioMedical Engineering OnLine**, v. 15, n. 1, p. 76, Jul 2016. ISSN 1475-925X. Disponível em: <https://doi.org/10.1186/s12938-016-0179-9>.

BEAVERS, I. Intelligence at the Edge Part 1: The Edge Node. In: **Analog Devices, Technical Articles**. [S.l.: s.n.], 2018.

BINKLEY, D. Tradeoffs and Optimization in Analog CMOS Design. In: **Mixed Design of Integrated Circuits and Systems, 2007. MIXDES '07. 14th International Conference on**. [S.l.: s.n.], 2007. p. 47–60.

BOL, D. et al. Building Ultra-Low-Power Low-Frequency Digital Circuits with High-Speed Devices. In: **2007 14th IEEE International Conference on Electronics, Circuits and Systems**. [S.l.: s.n.], 2007. p. 1404–1407.

BRAGA, R. A. et al. A 0.25-V calibration-less inverter-based OTA for low-frequency Gm-C applications. **Microelectronics Journal**, v. 83, p. 62–72, 2019. ISSN 0026-2692. Disponível em: <https://www.sciencedirect.com/science/article/pii/S002626921830418X>.

Buckel et al., T. A Novel Digital-Intensive Hybrid Polar-$\mathrm{I/Q}$ RF Transmitter Architecture. **IEEE Transactions on Circuits and Systems I: Regular Papers**, v. 65, n. 12, p. 4390–4403, 2018.

CABRERA, C. et al. Low-Voltage Low-Noise High-CMRR Biopotential Integrated Preamplifier. **IEEE Transactions on Circuits and Systems I: Regular Papers**, v. 68, n. 8, p. 3232–3241, 2021.

Cai, et al., Z. A CMOS Readout Circuit for Resistive Transducers Based on Algorithmic Resistance and Power Measurement. **IEEE Sensors Journal**, v. 17, n. 23, p. 7917–7927, 2017.

Cai, G.; Zhan, C.; Lu, Y. A Fast-Transient-Response Fully-Integrated Digital LDO With Adaptive Current Step Size Control. **IEEE Transactions on Circuits and Systems I: Regular Papers**, v. 66, n. 9, p. 3610–3619, 2019.

CAPRA, M. et al. Hardware and Software Optimizations for Accelerating Deep Neural Networks: Survey of Current Trends, Challenges, and the Road Ahead. **IEEE Access**, v. 8, p. 225134–225180, 2020.

CAPRA, M. et al. Edge Computing: A Survey On the Hardware Requirements in the Internet of Things World. **Future Internet**, v. 11, n. 4, 2019. ISSN 1999-5903. Disponível em: <https://www.mdpi.com/1999-5903/11/4/100>.

Carrara, S. Body Dust: Well Beyond Wearable and Implantable Sensors. **IEEE Sensors Journal**, p. 1–1, 2020.

CARRARA, S.; GEORGIOU, P. **Body Dust: Miniaturized Highly-integrated Low Power Sensing for Remotely Powered Drinkable CMOS Bioelectronics**. 2018.

CENTURELLI, F. et al. A Biasing Approach to design Ultra-Low-Power Standard-Cell-Based Analog Building Blocks for Nanometer SoCs. **IEEE Access**, p. 1–1, 2022.

Chandrakumar, H.; Marković, D. An 80-mVpp Linear-Input Range, 1.6- Gω Input Impedance, Low-Power Chopper Amplifier for Closed-Loop Neural Recording That Is Tolerant to 650-mVpp Common-Mode Interference. **IEEE Journal of Solid-State Circuits**, v. 52, n. 11, p. 2811–2828, 2017.

CHANG, H. et al. Bringing the cloud to the edge. In: **2014 IEEE Conference on Computer Communications Workshops (INFOCOM WKSHPS)**. [S.l.: s.n.], 2014. p. 346–351.

Chatterjee, S.; Tsividis, Y.; Kinget, P. 0.5-V analog circuit techniques and their application in OTA and filter design. **IEEE Journal of Solid-State Circuits**, v. 40, n. 12, p. 2373–2387, 2005.

CHEN, H. et al. Challenges and opportunities toward fully automated analog layout design. **Journal of Semiconductors**, IOP Publishing, v. 41, n. 11, p. 111407, nov 2020. Disponível em: <https://doi.org/10.1088/1674-4926/41/11/111407>.

CHEN, H. et al. MAGICAL: An Open-Source Fully Automated Analog IC Layout System from Netlist to GDSII. **IEEE Design Test**, v. 38, n. 2, p. 19–26, 2021.

CHEN, M. et al. Smart Clothing: Connecting Human with Clouds and Big Data for Sustainable Health Monitoring. **Mobile Networks and Applications**, v. 21, n. 5, p. 825–845, Oct 2016. ISSN 1572-8153. Disponível em: <https://doi.org/10.1007/s11036-016-0745-1>.

Chen, Y.; AL et. An Injectable 64 nW ECG Mixed-Signal SoC in 65 nm for Arrhythmia Monitoring. **IEEE Journal of Solid-State Circuits**, v. 50, n. 1, p. 375–390, 2015.

CHIANESE, A. et al. An associative engines based approach supporting collaborative analytics in the internet of cultural things. **Future Generation Computer Systems**, v. 66, p. 187–198, 2017. ISSN 0167-739X. Disponível em: <https://www.sciencedirect.com/science/article/pii/S0167739X16300929>.

CHIANG, L.; LU, B.; CASTILLO, I. Big Data Analytics in Chemical Engineering. **Annual Review of Chemical and Biomolecular Engineering**, v. 8, n. 1, p. 63–85, 2017. PMID: 28301733.

CORDOVA, D.; TOLEDO, P.; FABRIS, E. A low-voltage current reference with high immunity to EMI. In: **Integrated Circuits and Systems Design (SBCCI), 2014 27th Symposium on**. [S.l.: s.n.], 2014. p. 1–6.

CROSSLEY, J. et al. BAG: A designer-oriented integrated framework for the development of AMS circuit generators. In: **2013 IEEE/ACM International Conference on Computer-Aided Design (ICCAD)**. [S.l.: s.n.], 2013. p. 74–81.

Crovetti, P. S. Acquisition front-end immune to EMI. **Electronics Letters**, v. 48, n. 18, p. 1114–1115, 2012.

Crovetti, P. S. A Digital-Based Analog Differential Circuit. **IEEE Transactions on Circuits and Systems I: Regular Papers**, v. 60, n. 12, p. 3107–3116, 2013.

Crovetti, P. S. A Digital-Based Virtual Voltage Reference. **IEEE Transactions on Circuits and Systems I: Regular Papers**, v. 62, n. 5, p. 1315–1324, 2015.

Crovetti, P. S. All-Digital High Resolution d/a Conversion by Dyadic Digital Pulse Modulation. **IEEE Transactions on Circuits and Systems I: Regular Papers**, v. 64, n. 3, p. 573–584, 2017.

Crovetti, P. S. Spectral characteristics of DDPM streams and their application to all-digital amplitude modulation. **Electronics Letters**, v. 62, n. 3, 2020.

Crovetti, P. S. et al. breaking the boundaries between analogue and digital. **Electronics Letters**, v. 55, n. 12, p. 672–673, 2019.

Crovetti, P. S.; Rubino, R.; Musolino, F. Relaxation Digital-to-Analog Converter with Foreground Digital Self-Calibration. In: **2020 IEEE International Symposium on Circuits and Systems (ISCAS)**. [S.l.: s.n.], 2020. p. 1–5.

DANNER, J. et al. Rapid Precedent-Aware Pedestrian and Car Classification on Constrained IoT Platforms. In: **Proceedings of the 14th ACM/IEEE Symposium on Embedded Systems for Real-Time Multimedia**. New York, NY, USA: Association for Computing Machinery, 2016. (ESTIMedia'16), p. 29–36. ISBN 9781450345439. Disponível em: <https://doi.org/10.1145/2993452.2993562>.

DECUIR, J. Introducing Bluetooth Smart: Part 1: A look at both classic and new technologies. **IEEE Consumer Electronics Magazine**, v. 3, n. 1, p. 12–18, 2014.

Deng et al., W. A Fully Synthesizable All-Digital PLL With Interpolative Phase Coupled Oscillator, Current-Output DAC, and Fine-Resolution Digital Varactor Using Gated Edge Injection Technique. **IEEE Journal of Solid-State Circuits**, v. 50, n. 1, p. 68–80, 2015.

DESSOUKY, M.; KAISER, A. Very low-voltage digital-audio $\Delta\Sigma$ modulator with 88-dB dynamic range using local switch bootstrapping. **IEEE Journal of Solid-State Circuits**, v. 36, n. 3, p. 349–355, 2001.

DHAR, T. et al. ALIGN: A System for Automating Analog Layout. **IEEE Design Test**, v. 38, n. 2, p. 8–18, 2021.

DIGHE, S. et al. Within-Die Variation-Aware Dynamic-Voltage-Frequency-Scaling With Optimal Core Allocation and Thread Hopping for the 80-Core TeraFLOPS Processor. **IEEE Journal of Solid-State Circuits**, v. 46, n. 1, p. 184–193, 2011.

Drost, B.; Talegaonkar, M.; Hanumolu, P. K. A $0.55\mathrm{V}$ $61\mathrm{dB}-\mathrm{SNR}$ $67\mathrm{dB}-\mathrm{SFDR}$ $7\mathrm{MHz}$ 4^{th}-order Butterworth filter using ring-oscillator-based integrators in 90nm CMOS. In: **2012 IEEE International Solid-State Circuits Conference**. [S.l.: s.n.], 2012. p. 360–362.

Eberlein, M.; Pretl, H.; Georgiev, Z. Time-Controlled and FinFET Compatible Sub-Bandgap References Using Bulk-Diodes. **IEEE Transactions on Circuits and Systems II: Express Briefs**, v. 66, n. 10, p. 1608–1612, 2019.

EICK, M. et al. Comprehensive Generation of Hierarchical Placement Rules for Analog Integrated Circuits. **IEEE Transactions on Computer-Aided Design of Integrated Circuits and Systems**, v. 30, n. 2, p. 180–193, 2011.

EL-SAYED, H. et al. Edge of things: The big picture on the integration of edge, iot and the cloud in a distributed computing environment. **IEEE Access**, IEEE, v. 6, p. 1706–1717, 2017.

EMMERT, J. M.; VANDEWERKER, S. A. EMC: Efficient Muller C-Element Implementation for High Bit-width Asynchronous Applications. In: **2021 IEEE International Midwest Symposium on Circuits and Systems (MWSCAS)**. [S.l.: s.n.], 2021. p. 816–819.

ENZ, C.; CHICCO, F.; PEZZOTTA, A. Nanoscale MOSFET Modeling: Part 1: The Simplified EKV Model for the Design of Low-Power Analog Circuits. **IEEE Solid-State Circuits Magazine**, v. 9, n. 3, p. 26–35, 2017.

ENZ, C.; CHICCO, F.; PEZZOTTA, A. Nanoscale MOSFET Modeling: Part 2: Using the Inversion Coefficient as the Primary Design Parameter. **IEEE Solid-State Circuits Magazine**, v. 9, n. 4, p. 73–81, 2017.

Fahmy, A. et al. An All-Digital Scalable and Reconfigurable Wide-Input Range Stochastic ADC Using Only Standard Cells. **IEEE Transactions on Circuits and Systems II: Express Briefs**, v. 62, n. 8, p. 731–735, 2015.

FERREIRA, A. et al. Automated analog IC design constraints generation for a layout-aware sizing approach. In: **2016 13th International Conference on Synthesis, Modeling, Analysis and Simulation Methods and Applications to Circuit Design (SMACD)**. [S.l.: s.n.], 2016. p. 1–4.

FERREIRA, L. H. C.; PIMENTA, T. C.; MORENO, R. L. An Ultra-Low-Voltage Ultra-Low-Power CMOS Miller OTA With Rail-to-Rail Input/Output Swing. **IEEE Transactions on Circuits and Systems II: Express Briefs**, v. 54, n. 10, p. 843–847, 2007.

Ferreira, L. H. C.; Sonkusale, S. R. A 60-dB Gain OTA Operating at 0.25-V Power Supply in 130-nm Digital CMOS Process. **IEEE Transactions on Circuits and Systems I: Regular Papers**, v. 61, n. 6, p. 1609–1617, 2014.

FREDRIK, D. et al. Growing opportunities in the Internet of Things. In: ____. [S.l.]: McKinsey Global Institute, 2019. cap. 1, p. 1–10.

GALUP-MONTORO, C. et al. A compact model of MOSFET mismatch for circuit design. **IEEE Journal of Solid-State Circuits**, v. 40, n. 8, p. 1649–1657, 2005.

GALUP-MONTORO, C. et al. A Compact Model of MOSFET Mismatch for Circuit Design. **IEEE J. of Solid-State Circuits**, v. 40, n. 8, p. 1649–1657, Aug 2005. ISSN 0018-9200.

GALUP-MONTORO, C.; SCHNEIDER, M. C.; MACHADO, M. B. Ultra-Low-Voltage Operation of CMOS Analog Circuits: Amplifiers, Oscillators, and Rectifiers. **IEEE Transactions on Circuits and Systems II: Express Briefs**, v. 59, n. 12, p. 932–936, 2012.

GARDE, M. P. et al. Super Class-AB Recycling Folded Cascode OTA. **IEEE Journal of Solid-State Circuits**, v. 53, n. 9, p. 2614–2623, 2018.

Gebreyohannes, F. T. et al. All-Digital Transmitter Architecture Based on Two-Path Parallel 1-bit High Pass Filtering DACs. **IEEE Transactions on Circuits and Systems I: Regular Papers**, v. 65, n. 11, p. 3956–3969, 2018.

Ghoreishizadeh, S. S.; AL. et. An Integrated Control and Readout Circuit for Implantable Multi-Target Electrochemical Biosensing. **IEEE Transactions on Biomedical Circuits and Systems**, v. 8, n. 6, p. 891–898, 2014.

GHOSH, A.; PATIL, K. A.; VUPPALA, S. K. PLEMS: Plug Load Energy Management Solution for Enterprises. In: **2013 IEEE 27th International Conference on Advanced Information Networking and Applications (AINA)**. [S.l.: s.n.], 2013. p. 25–32.

Gielen, G. G. E.; Hernandez, L.; Rombouts, P. Time-Encoding Analog-to-Digital Converters: Bridging the Analog Gap to Advanced Digital CMOS-Part 1: Basic Principles. **IEEE Solid-State Circuits Magazine**, v. 12, n. 2, p. 47–55, 2020.

Gielen, G. G. E.; Hernandez, L.; Rombouts, P. Time-Encoding Analog-to-Digital Converters: Bridging the Analog Gap to Advanced Digital CMOS-Part 2: Architectures and Circuits. **IEEE Solid-State Circuits Magazine**, v. 12, n. 3, p. 18–27, 2020.

GIMENEZ, R. et al. The Safety Transformation in the Future Internet Domain. In: ÁLVAREZ, F. et al. (Ed.). **The Future Internet**. Berlin, Heidelberg: Springer Berlin Heidelberg, 2012. p. 190–200. ISBN 978-3-642-30241-1.

GRAEB, H. ITRS 2011 Analog EDA Challenges and Approaches. In: **2012 Design, Automation Test in Europe Conference Exhibition (DATE)**. [S.l.: s.n.], 2012. p. 1150–1155.

GRASSO, A. D. et al. 0.9-V Class-AB Miller OTA in 0.35- μm CMOS With Threshold-Lowered Non-Tailed Differential Pair. **IEEE Transactions on Circuits and Systems I: Regular Papers**, v. 64, n. 7, p. 1740–1747, 2017.

Gray, P. R.; Meyer, R. G. MOS operational amplifier design-a tutorial overview. **IEEE Journal of Solid-State Circuits**, v. 17, n. 6, p. 969–982, 1982.

GUO, B.; ZHANG, D.; WANG, Z. Living with Internet of Things: The Emergence of Embedded Intelligence. In: **2011 International Conference on Internet of Things and 4th International Conference on Cyber, Physical and Social Computing**. [S.l.: s.n.], 2011. p. 297–304.

HAJIMIRI, A.; LEE, T. A general theory of phase noise in electrical oscillators. **IEEE Journal of Solid-State Circuits**, v. 33, n. 2, p. 179–194, 1998.

Han, D.; AL. et. A 0.45V 100-Channel Neural-Recording IC With Sub-μW/Channel Consumption in 0.18 μm CMOS. **IEEE Transactions on Biomedical Circuits and Systems**, v. 7, n. 6, p. 735–746, 2013.

Harpe, P.; AL. et. A 0.20 mm^2 3 nW Signal Acquisition IC for Miniature Sensor Nodes in 65 nm CMOS. **IEEE Journal of Solid-State Circuits**, v. 51, n. 1, p. 240–248, 2016.

HE, W.; YAN, G.; XU, L. D. Developing Vehicular Data Cloud Services in the IoT Environment. **IEEE Transactions on Industrial Informatics**, v. 10, n. 2, p. 1587–1595, 2014.

HERNANDEZ, L.; PREFASI, E. Analog-to-digital conversion using noise shaping and time encoding. **IEEE Transactions on Circuits and Systems I: Regular Papers**, v. 55, n. 7, p. 2026–2037, 2008.

HODGKIN, A. L.; HUXLEY, A. F. A quantitative description of membrane current and its application to conduction and excitation in nerve. **The Journal of physiology**, v. 117, n. 4, p. 500–544, Aug 1952. ISSN 0022-3751. 12991237[pmid]. Disponível em: <https://pubmed.ncbi.nlm.nih.gov/12991237>.

HONG, S.-W.; CHO, G.-H. 7.4μW Ultra-high slew-rate pseudo single-stage amplifier driving 0.1-to-15nF capacitive load with $> 69^o$ phase margin. In: **2015 Symposium on VLSI Circuits (VLSI Circuits)**. [S.l.: s.n.], 2015. p. C296–C297.

HOSSAIN, M. S.; MUHAMMAD, G. Cloud-assisted Industrial Internet of Things (IIoT) – Enabled framework for health monitoring. **Computer Networks**, v. 101, p. 192–202, 2016. ISSN 1389-1286. Industrial Technologies and Applications for the Internet of Things. Disponível em: <https://www.sciencedirect.com/science/article/pii/S1389128616300019>.

Huang et al., J. A 0.01-mm^2 Mostly Digital Capacitor-Less AFE for Distributed Autonomous Neural Sensor Nodes. **IEEE Solid-State Circuits Letters**, v. 1, n. 7, p. 162–165, 2018.

JAIN, S.; LIN, L.; ALIOTO, M. Dynamically Adaptable Pipeline for Energy-Efficient Microarchitectures Under Wide Voltage Scaling. **IEEE Journal of Solid-State Circuits**, v. 53, n. 2, p. 632–641, 2018.

JAMES, M.; MICHAEL, C.; JACQUES, B. Disruptive Technologies: Advances That Will Transform Life, Business, and the Global Economy. In: ____. [S.l.]: McKinsey Global Institute, 2013. cap. 1, p. 1–10.

JARA, A. J.; GENOUD, D.; BOCCHI, Y. Big data for smart cities with KNIME a real experience in the SmartSantander testbed. **Software: Practice and Experience**, v. 45, n. 8, p. 1145–1160, 2015. Disponível em: <https://onlinelibrary.wiley.com/doi/abs/10.1002/spe.2274>.

Jayaraj, A. et al. 76-dB-DR, 48fJ/Step Second-Order VCO-based Current-to-Digital Converter. **IEEE Transactions on Circuits and Systems I: Regular Papers**, v. 67, n. 4, p. 1149–1157, 2020.

JIN, J. et al. An Information Framework for Creating a Smart City Through Internet of Things. **IEEE Internet of Things Journal**, v. 1, n. 2, p. 112–121, 2014.

JUSTO, D.; CAVALHEIRO, D.; MOLL, F. Body bias generators for ultra low voltage circuits in FDSOI technology. In: **2017 32nd Conference on Design of Circuits and Integrated Systems (DCIS)**. [S.l.: s.n.], 2017. p. 1–6.

KAHN, J. M.; KATZ, R. H.; PISTER, K. S. J. Next Century Challenges: Mobile Networking for "Smart Dust". In: **Proceedings of the 5th Annual ACM/IEEE International Conference on Mobile Computing and Networking**. New York, NY, USA: Association for Computing Machinery, 1999. (MobiCom '99), p. 271–278. ISBN 1581131429. Disponível em: <https://doi.org/10.1145/313451.313558>.

Kalani, S. et al. A 0.2V 492nW VCO-based OTA with 60kHz UGB and 207 μVrms noise. In: **2017 IEEE International Symposium on Circuits and Systems (ISCAS)**. [S.l.: s.n.], 2017. p. 1–4.

Kalani, S.; Kinget, P. R. Zero-Crossing-Time-Difference Model for Stability Analysis of VCO-Based OTAs. **IEEE Transactions on Circuits and Systems I: Regular Papers**, v. 67, n. 3, p. 839–851, 2020.

KAMILARIS, A. et al. Agri-IoT: A semantic framework for Internet of Things-enabled smart farming applications. In: **2016 IEEE 3rd World Forum on Internet of Things (WF-IoT)**. [S.l.: s.n.], 2016. p. 442–447.

KHATEB, F.; KULEJ, T. Design and Implementation of a 0.3-V Differential Difference Amplifier. **IEEE Transactions on Circuits and Systems I: Regular Papers**, v. 66, n. 2, p. 513–523, 2019.

KHATEB, F. et al. 0.5-V High Linear and Wide Tunable OTA for Biomedical Applications. **IEEE Access**, v. 9, p. 103784–103794, 2021.

Kim, D. et al. A Second-Order $\Delta\Sigma$ Time-to-Digital Converter Using Highly Digital Time-Domain Arithmetic Circuits. **IEEE Transactions on Circuits and Systems II: Express Briefs**, v. 66, n. 10, p. 1643–1647, 2019.

Kim et al., S. J. A 4-Phase 30-70 MHz Switching Frequency Buck Converter Using a Time-Based Compensator. **IEEE Journal of Solid-State Circuits**, v. 50, n. 12, p. 2814–2824, 2015.

KINGET, P. R. Designing analog and RF circuits for ultra-low supply voltages. In: **ESSDERC 2007 - 37th European Solid State Device Research Conference**. [S.l.: s.n.], 2007. p. 58–67.

Kinget, P. R. Scaling analog circuits into deep nanoscale CMOS: Obstacles and ways to overcome them. In: **2015 IEEE Custom Integrated Circuits Conference (CICC)**. [S.l.: s.n.], 2015. p. 1–8.

KOMNINOS, N.; PHILIPPOU, E.; PITSILLIDES, A. Survey in Smart Grid and Smart Home Security: Issues, Challenges and Countermeasures. **IEEE Communications Surveys Tutorials**, v. 16, n. 4, p. 1933–1954, 2014.

KORAT, U. A.; ALIMOHAMMAD, A. A Reconfigurable Hardware Architecture for Principal Component Analysis. **Circuits, Systems, and Signal Processing**, v. 38, n. 5, p. 2097–2113, May 2019. ISSN 1531-5878. Disponível em: <https://doi.org/10.1007/s00034-018-0953-y>.

KORTUEM, G. et al. Smart objects as building blocks for the Internet of Things. **IEEE Internet Computing**, v. 14, n. 1, p. 44–51, 2010.

Krishna Chekuri et al., V. C. A Fully Synthesized Integrated Buck Regulator with Auto-generated GDS-II in 65nm CMOS Process. In: **2020 IEEE Custom Integrated Circuits Conference (CICC)**. [S.l.: s.n.], 2020. p. 1–4.

KULEJ, T.; KHATEB, F. A 0.3-V 98-dB Rail-to-Rail OTA in $0.18\ \mu$m CMOS. **IEEE Access**, v. 8, p. 27459–27467, 2020.

KULEJ, T.; KHATEB, F. A Compact 0.3-V Class AB Bulk-Driven OTA. **IEEE Transactions on Very Large Scale Integration (VLSI) Systems**, v. 28, n. 1, p. 224–232, 2020.

Kundert, K. S. Introduction to RF simulation and its application. **IEEE Journal of Solid-State Circuits**, v. 34, n. 9, p. 1298–1319, 1999.

Kuo et al., F. A Bluetooth Low-Energy Transceiver With 3.7-mW All-Digital Transmitter, 2.75-mW High-IF Discrete-Time Receiver, and TX/RX Switchable On-Chip Matching Network. **IEEE Journal of Solid-State Circuits**, v. 52, n. 4, p. 1144–1162, 2017.

LANUZZA, M.; TACO, R.; ALBANO, D. Dynamic gate-level body biasing for subthreshold digital design. In: **2014 IEEE 5th Latin American Symposium on Circuits and Systems**. [S.l.: s.n.], 2014. p. 1–4.

LEE, J. H.; HANCOCK, M. G.; HU, M.-C. Towards an effective framework for building smart cities: Lessons from Seoul and San Francisco. **Technological Forecasting and Social Change**, v. 89, p. 80–99, 2014. ISSN 0040-1625. Disponível em: <https://www.sciencedirect.com/science/article/pii/S0040162513002187>.

Li, X. et al. A 0.35V-to-1.0 V synthesizable rail-to-rail dynamic voltage comparator based OAI&AOI logic. **Analog Integrated Circuits and Signal Processing volume**, v. 104, p. 351–357, 2020.

LIM, W. et al. 8.2 Batteryless Sub-nW Cortex-M0+ processor with dynamic leakage-suppression logic. In: **2015 IEEE International Solid-State Circuits Conference - (ISSCC) Digest of Technical Papers**. [S.l.: s.n.], 2015. p. 1–3.

LIN, L.; JAIN, S.; ALIOTO, M. Integrated Power Management for Battery-Indifferent Systems With Ultra-Wide Adaptation Down to nW. **IEEE Journal of Solid-State Circuits**, v. 55, n. 4, p. 967–976, 2020.

LIN, M. P.-H. et al. DeMixGen: Deterministic Mixed-signal Layout Generation With Separated Analog and Digital Signal Paths. **IEEE Transactions on Computer-Aided Design of Integrated Circuits and Systems**, v. 35, n. 8, p. 1229–1242, 2016.

LIN, X. et al. Task Scheduling with Dynamic Voltage and Frequency Scaling for Energy Minimization in the Mobile Cloud Computing Environment. **IEEE Transactions on Services Computing**, v. 8, n. 2, p. 175–186, 2015.

Liu, J. et al. A Fully Synthesized 77-dB SFDR Reprogrammable SRMC Filter Using Digital Standard Cells. **IEEE Transactions on Very Large Scale Integration (VLSI) Systems**, v. 26, n. 6, p. 1126–1138, 2018.

LIU, M. et al. Closing the Design Loop: Bayesian Optimization Assisted Hierarchical Analog Layout Synthesis. In: **2020 57th ACM/IEEE Design Automation Conference (DAC)**. [S.l.: s.n.], 2020. p. 1–6.

LOTZE, N.; MANOLI, Y. A 62 mV 0.13 μm CMOS Standard-Cell-Based Design Technique Using Schmitt-Trigger Logic. **IEEE Journal of Solid-State Circuits**, v. 47, n. 1, p. 47–60, 2012.

Lu, Y. et al. A Distributed Power Delivery Grid Based on Analog-Assisted Digital LDOs With Cooperative Regulation and IR-Drop Reduction. **IEEE Transactions on Circuits and Systems I: Regular Papers**, v. 67, n. 8, p. 2859–2871, 2020.

Lv, L. et al. Inverter-Based Subthreshold Amplifier Techniques and Their Application in 0.3-V $\Delta\Sigma$-Modulators. **IEEE Journal of Solid-State Circuits**, v. 54, n. 5, p. 1436–1445, 2019.

MAK, C. L.; FAN, H. S. L. Heavy Flow-Based Incident Detection Algorithm Using Information From Two Adjacent Detector Stations. **Journal of Intelligent Transportation Systems**, Taylor and Francis, v. 10, n. 1, p. 23–31, 2006. Disponível em: <https://doi.org/10.1080/15472450500455229>.

MANGIA, M. et al. Adapted compressed sensing: a game worth playing. **IEEE Circuits and Systems Magazine**, IEEE, v. 20, n. 1, p. 40–60, 2020.

MARCHIONI, A. et al. Subspace Energy Monitoring for Anomaly Detection Sensor or Edge. **IEEE Internet of Things Journal**, v. 7, n. 8, p. 7575–7589, 2020.

MAROLT, D. **Layout automation in analog IC design with formalized and nonformalized expert knowledge**. Tese (Doutorado) — University of Stuttgart, Jan. 2019.

MAROLT, D.; SCHEIBLE, J.; JERKE, G. CUS01: A Practical Layout Module Pcell Concept for Analog IC Design. In: . [S.l.: s.n.], 2013. p. 1–10.

MELEK, L. A. P.; SCHNEIDER, M. C.; GALUP-MONTORO, C. Operation of the Classical CMOS Schmitt Trigger As an Ultra-Low-Voltage Amplifier. **IEEE Transactions on Circuits and Systems II: Express Briefs**, v. 65, n. 9, p. 1239–1243, 2018.

MICHEL, F.; STEYAERT, M. S. J. A 250 mV 7.5 μW 61 dB SNDR SC SD Modulator Using Near-Threshold-Voltage-Biased Inverter Amplifiers in 130 nm CMOS. **IEEE Journal of Solid-State Circuits**, v. 47, n. 3, p. 709–721, 2012.

Mondal, S.; Hall, D. A. A 13.9-nA ECG Amplifier Achieving 0.86/0.99 NEF/PEF Using AC-Coupled OTA-Stacking. **IEEE Journal of Solid-State Circuits**, v. 55, n. 2, p. 414–425, 2020.

MORGAN, L. Edge Analytics An Antidote to IoT Data Deluge. In: **Informationweek, Big Data**. [S.l.: s.n.], 2016.

MUKHERJEE, A. et al. Utilising condor for data parallel analytics in an IoT context — An experience report. In: **2013 IEEE 9th International Conference on Wireless and Mobile Computing, Networking and Communications (WiMob)**. [S.l.: s.n.], 2013. p. 325–331.

MUKHERJEE, A.; PAL, A.; MISRA, P. Data Analytics in Ubiquitous Sensor-Based Health Information Systems. In: **2012 Sixth International Conference on Next Generation Mobile Applications, Services and Technologies**. [S.l.: s.n.], 2012. p. 193–198.

MUKHERJEE, U. K.; CHATTERJEE, S. Fast algorithm for computing weighted projection quantiles and data depth for high-dimensional large data clouds. In: **2014 IEEE International Conference on Big Data (Big Data)**. [S.l.: s.n.], 2014. p. 64–71.

MURMANN, B. Digitally Assisted Analog Circuits. **IEEE Micro**, IEEE Computer Society, Los Alamitos, CA, USA, v. 26, n. 02, p. 38–47, mar 2006. ISSN 1937-4143.

Murmann, B. Digitally Assisted Analog Circuits; Fifth IEEE Dallas Circuits and Systems Workshop. In: **2006 IEEE Dallas/CAS Workshop on Design, Applications, Integration and Software**. [S.l.: s.n.], 2006. p. 23–30.

Nauta, B. A CMOS transconductance-C filter technique for very high frequencies. **IEEE Journal of Solid-State Circuits**, v. 27, n. 2, p. 142–153, 1992.

NECHIFOR, S. et al. Predictive analytics based on CEP for logistic of sensitive goods. In: **2014 International Conference on Optimization of Electrical and Electronic Equipment (OPTIM)**. [S.l.: s.n.], 2014. p. 817–822.

NGU, A. H. et al. IoT Middleware: A Survey on Issues and Enabling Technologies. **IEEE Internet of Things Journal**, v. 4, n. 1, p. 1–20, 2017.

Nguyen, V.; Schembari, F.; Staszewski, R. B. A 0.2-V 30-MS/s 11b-ENOB Open-Loop VCO-Based ADC in 28-nm CMOS. **IEEE Solid-State Circuits Letters**, v. 1, n. 9, p. 190–193, 2018.

Opteynde, F. A maximally-digital radio receiver front-end. In: **2010 IEEE International Solid-State Circuits Conference - (ISSCC)**. [S.l.: s.n.], 2010. p. 450–451.

OTIS, B.; RABAEY, J. **Ultra-low power wireless technologies for sensor networks**. [S.l.]: Springer Science & Business Media, 2007.

PADEN, B. et al. A Survey of Motion Planning and Control Techniques for Self-Driving Urban Vehicles. **IEEE Transactions on Intelligent Vehicles**, v. 1, n. 1, p. 33–55, 2016.

PAIM, G. et al. On the Resiliency of NCFET Circuits Against Voltage Over-Scaling. **IEEE Transactions on Circuits and Systems I: Regular Papers**, v. 68, n. 4, p. 1481–1492, 2021.

PALATTELLA, M. R. et al. Standardized Protocol Stack for the Internet of (Important) Things. **IEEE Communications Surveys Tutorials**, v. 15, n. 3, p. 1389–1406, 2013.

PALUMBO, G.; SCOTTI, G. A Novel Standard-Cell-Based Implementation of the Digital OTA Suitable for Automatic Place and Route. **Journal of Low Power Electronics and Applications**, v. 11, n. 4, 2021. ISSN 2079-9268. Disponível em: <https://www.mdpi.com/2079-9268/11/4/42>.

Park, J.; Hwang, Y.; Jeong, D. A 0.5V Fully Synthesizable SAR ADC for On-Chip Distributed Waveform Monitors. **IEEE Access**, v. 7, p. 63686–63697, 2019.

PARK, M.; PERROTT, M. H. A multiphase PWM RF modulator using a VCO-based opamp in 45nm CMOS. In: **2010 IEEE Radio Frequency Integrated Circuits Symposium**. [S.l.: s.n.], 2010. p. 39–42.

Park, Y.; Wentzloff, D. D. An All-Digital 12pJ/Pulse IR-UWB Transmitter Synthesized From a Standard Cell Library. **IEEE Journal of Solid-State Circuits**, v. 46, n. 5, p. 1147–1157, 2011.

Park, Y.; Wentzloff, D. D. An all-digital PLL synthesized from a digital standard cell library in 65nm CMOS. In: **2011 IEEE Custom Integrated Circuits Conference (CICC)**. [S.l.: s.n.], 2011. p. 1–4.

Pinckney, N.; Blaauw, D.; Sylvester, D. Low-Power Near-Threshold Design: Techniques to Improve Energy Efficiency. **IEEE Solid-State Circuits Magazine**, v. 7, n. 2, p. 49–57, Spring 2015. ISSN 1943-0582.

PIOVESAN, N. et al. Data Analytics for Smart Parking Applications. **Sensors**, v. 16, n. 10, 2016. ISSN 1424-8220. Disponível em: <https://www.mdpi.com/1424-8220/16/10/1575>.

PLOENNIGS, J.; SCHUMANN, A.; LÉCUÉ, F. Adapting Semantic Sensor Networks for Smart Building Diagnosis. In: MIKA, P. et al. (Ed.). **The Semantic Web – ISWC 2014**. Cham: Springer International Publishing, 2014. p. 308–323. ISBN 978-3-319-11915-1.

Qian et al., L. A Fast-Transient Response Digital Low-Dropout Regulator With Dual-Modes Tuning Technique. **IEEE Transactions on Circuits and Systems II: Express Briefs**, v. 67, n. 12, p. 2943–2947, 2020.

QU, W. et al. Design-Oriented Analysis for Miller Compensation and Its Application to Multistage Amplifier Design. **IEEE Journal of Solid-State Circuits**, v. 52, n. 2, p. 517–527, 2017.

Rahiminejad et al., E. A Low-Voltage High-Precision Time-Domain Winner-Take-All Circuit. **IEEE Transactions on Circuits and Systems II: Express Briefs**, v. 67, n. 1, p. 4–8, 2020.

RAZAVI, B. **Design of analog CMOS integrated circuits**. [S.l.]: Tata McGraw-Hill Education, 2002.

RAZIP, A. M. et al. A Mobile Visual Analytics Approach for Law Enforcement Situation Awareness. In: **2014 IEEE Pacific Visualization Symposium**. [S.l.: s.n.], 2014. p. 169–176.

Richelli, A.; Colalongo, L.; Kovács-Vajna, Z. . M. EMI Effect in Voltage-to-Time Converters. **IEEE Transactions on Circuits and Systems II: Express Briefs**, p. 1–1, 2020.

ROBAK, S.; FRANCZYK, B.; ROBAK, M. Applying big data and linked data concepts in supply chains management. In: **2013 Federated Conference on Computer Science and Information Systems**. [S.l.: s.n.], 2013. p. 1215–1221.

RODOVALHO, L. H.; AIELLO, O.; RODRIGUES, C. R. Ultra-Low-Voltage Inverter-Based Operational Transconductance Amplifiers with Voltage Gain Enhancement by Improved Composite Transistors. **Electronics**, v. 9, n. 9, 2020. ISSN 2079-9292. Disponível em: <https://www.mdpi.com/2079-9292/9/9/1410>.

RODOVALHO, L. H.; RODRIGUES, C. R.; AIELLO, O. A Two-Stage Single-Ended OTA with Improved Composite Transistors. In: **2021 IEEE Nordic Circuits and Systems Conference (NorCAS)**. [S.l.: s.n.], 2021. p. 1–7.

ROMKEY, J. Toast of the IoT: The 1990 Interop Internet Toaster. **IEEE Consumer Electronics Magazine**, v. 6, n. 1, p. 116–119, 2017.

SCHNEIDER, C.; GALUP-MONTORO, C. **CMOS Analog Design Using All-Region MOSFET Modeling**. 1st. ed. [S.l.]: Cambridge University Press, 2010.

SCHNIZLER, F. et al. Heterogeneous stream processing for disaster detection and alarming. In: **2014 IEEE International Conference on Big Data (Big Data)**. [S.l.: s.n.], 2014. p. 914–923.

SEIDEL, H. B. et al. Approximate Pruned and Truncated Haar Discrete Wavelet Transform VLSI Hardware for Energy-Efficient ECG Signal Processing. **IEEE Transactions on Circuits and Systems I: Regular Papers**, v. 68, n. 5, p. 1814–1826, 2021.

SEO, D. et al. Wireless Recording in the Peripheral Nervous System with Ultrasonic Neural Dust. **Neuron**, v. 91, n. 3, p. 529–539, 2016. ISSN 0896-6273. Disponível em: <https://www.sciencedirect.com/science/article/pii/S0896627316303440>.

Seo et al., M. A Reusable Code-Based SAR ADC Design With CDAC Compiler and Synthesizable Analog Building Blocks. **IEEE Transactions on Circuits and Systems II: Express Briefs**, v. 65, n. 12, p. 1904–1908, 2018.

SEPULVEDA, A.; SPEULMANNS, J.; VEREECKEN, P. M. Bending impact on the performance of a flexible li4ti5o12-based all-solid-state thin-film battery. **Science and Technology of Advanced Materials**, Taylor and Francis, v. 19, n. 1, p. 454–464, 2018. PMID: 29868149.

Shannon, C. E. A mathematical theory of communication. **The Bell System Technical Journal**, v. 27, n. 3, p. 379–423, 1948.

Shen, L.; Lu, N.; Sun, N. A 1-V 0.25-μW Inverter Stacking Amplifier With 1.07 Noise Efficiency Factor. **IEEE Journal of Solid-State Circuits**, v. 53, n. 3, p. 896–905, 2018.

Shi, C.; AL. et. A 0.065-mm^3 Monolithically-Integrated Ultrasonic Wireless Sensing Mote for Real-Time Physiological Temperature Monitoring. **IEEE Transactions on Biomedical Circuits and Systems**, v. 14, n. 3, p. 412–424, 2020.

SIOW, E.; TIROPANIS, T.; HALL, W. Analytics for the Internet of Things: A Survey. **ACM Comput. Surv.**, Association for Computing Machinery, New York, NY, USA, v. 51, n. 4, jul 2018. ISSN 0360-0300. Disponível em: <https://doi.org/10.1145/3204947>.

Staszewski et al., R. B. All-digital TX frequency synthesizer and discrete-time receiver for Bluetooth radio in 130-nm CMOS. **IEEE Journal of Solid-State Circuits**, v. 39, n. 12, p. 2278–2291, 2004.

Straayer, M. Z.; Perrott, M. H. A 12-Bit, 10-MHz Bandwidth, Continuous-Time $\Sigma\Delta$ ADC With a 5-Bit, $950 - \mathrm{MS/s}$ VCO-Based Quantizer. **IEEE Journal of Solid-State Circuits**, v. 43, n. 4, p. 805–814, 2008.

Tang, J. et al. A 0.7V Fully-on-Chip Pseudo-Digital LDO Regulator with 6.3μA Quiescent Current and 100mV Dropout Voltage in 180nm CMOS. In: **ESSCIRC 2018 - IEEE 44th European Solid State Circuits Conference (ESSCIRC)**. [S.l.: s.n.], 2018. p. 206–209.

Taylor, G.; Galton, I. A Mostly-Digital Variable-Rate Continuous-Time Delta-Sigma Modulator ADC. **IEEE Journal of Solid-State Circuits**, v. 45, n. 12, p. 2634–2646, 2010.

Tejasvi, A.; Makinwa k.; Hanumolu, P. A VCO Based Highly Digital Temperature Sensor With $0.034^{\circ}\mathrm{C/mV}$ Supply Sensitivity. **IEEE Solid-State Circuits Journal**, v. 11, n. 7, p. 2651 – 2663, 2016.

TIMARCHI, S.; ALIOTO, M. Ultra-low voltage standard cell libraries: Design strategies and a case study. In: **2016 IEEE International Conference on Electronics, Circuits and Systems (ICECS)**. [S.l.: s.n.], 2016. p. 520–523.

Toledo et al., P. CMOS transconductor analysis for low temperature sensitivity based on ZTC MOSFET condition. In: **2015 28th Symposium on Integrated Circuits and Systems Design (SBCCI)**. [S.l.: s.n.], 2015. p. 1–7.

Toledo, P.; Aiello, O.; Crovetti, P. S. A 300mV-Supply Standard-Cell-Based OTA with Digital PWM Offset Calibration. In: **2019 IEEE Nordic Circuits and Systems Conference (NORCAS): NORCHIP and International Symposium of System-on-Chip (SoC)**. [S.l.: s.n.], 2019. p. 1–5.

TOLEDO, P.; AIELLO, O.; CROVETTI, P. S. A 300mV-Supply Standard-Cell-Based OTA with Digital PWM Offset Calibration. In: **2019 IEEE Nordic Circuits and Systems Conference (NORCAS): NORCHIP and International Symposium of System-on-Chip (SoC)**. [S.l.: s.n.], 2019. p. 1–5.

Toledo, P. et al. Fully-Digital Rail-to-Rail OTA with Sub-1,000 μm^2 Area, 250-mV Minimum Supply and nW Power at 150-pF Load in 180nm. **IEEE Solid-State Circuits Letters**, p. 1–1, 2020.

Toledo, P. et al. A 300mV-Supply, 2nW-Power, 80pF-Load CMOS Digital-Based OTA for IoT Interfaces. In: **2019 26th IEEE International Conference on Electronics, Circuits and Systems (ICECS)**. [S.l.: s.n.], 2019. p. 170–173.

Toledo, P. et al. Dynamic and Static Calibration of Ultra-Low-Voltage, Digital-Based Operational Transconductance Amplifiers. **Electronics**, 2020.

TOLEDO, P. et al. 300mV-Supply, sub-nw-power Digital-Based Operational Transconductance Amplifier. **IEEE Transactions on Circuits and Systems II: Express Briefs**, IEEE, 2021.

TOLEDO, P. et al. CMOS Transconductor Analysis for Low Temperature Sensitivity Based on ZTC MOSFET Condition. In: **Integrated Circuits and Systems Design (SBCCI), 2015 28th Symposium on**. [S.l.: s.n.], 2015. p. 1–7.

TOLEDO, P. et al. Re-Thinking Analog Integrated Circuits in Digital Terms: A New Design Concept for the IoT Era. **IEEE Transactions on Circuits and Systems II: Express Briefs**, v. 68, n. 3, p. 816–822, 2021.

TRUESDELL, D. S. et al. A 6–140-nW 11 Hz–8.2-kHz DVFS RISC-V Microprocessor Using Scalable Dynamic Leakage-Suppression Logic. **IEEE Solid-State Circuits Letters**, v. 2, n. 8, p. 57–60, 2019.

TSIVIDIS, Y.; MCANDREW, C. **Operation and Modeling of the MOS Transistor**. 3rd. ed. [S.l.]: Oxford, 2010.

Un et al., K. Design Considerations of the Interpolative Digital Transmitter for Quantization Noise and Replicas Rejection. **IEEE Transactions on Circuits and Systems II: Express Briefs**, v. 67, n. 1, p. 37–41, 2020.

UNION, I. T. **Overview of the Internet of Things. Technical Report**. 2012. Http://www.itu.int/ITU-T/recommendations/rec.aspx?rec=11559.

Unnikrishnan, V.; Vesterbacka, M. Time-Mode Analog-to-Digital Conversion Using Standard Cells. **IEEE Transactions on Circuits and Systems I: Regular Papers**, v. 61, n. 12, p. 3348–3357, 2014.

VALTIERRA, J. L. et al. A Sub-μW Reconfigurable Front-End for Invasive Neural Recording That Exploits the Spectral Characteristics of the Wideband Neural Signal. **IEEE Transactions on Circuits and Systems I: Regular Papers**, v. 67, n. 5, p. 1426–1437, 2020.

VARGHEESE, R.; DAHIR, H. An IoT/IoE enabled architecture framework for precision on shelf availability: Enhancing proactive shopper experience. In: **2014 IEEE International Conference on Big Data (Big Data)**. [S.l.: s.n.], 2014. p. 21–26.

VERDOUW, C.; BEULENS, A.; van der Vorst, J. Virtualisation of floricultural supply chains: A review from an Internet of Things perspective. **Computers and Electronics in Agriculture**, v. 99, p. 160–175, 2013. ISSN 0168-1699. Disponível em: <https://www.sciencedirect.com/science/article/pii/S0168169913002135>.

Wahbah, M.; AL. et. Characterization of Human Body-Based Thermal and Vibration Energy Harvesting for Wearable Devices. **IEEE Journal on Emerging and Selected Topics in Circuits and Systems**, v. 4, n. 3, p. 354–363, 2014.

WANG, Y. et al. Mobile-Edge Computing: Partial Computation Offloading Using Dynamic Voltage Scaling. **IEEE Transactions on Communications**, v. 64, n. 10, p. 4268–4282, 2016.

Waters, A.; Moon, U. A fully automated verilog-to-layout synthesized ADC demonstrating 56dB- SNDR with 2MHz-BW. In: **2015 IEEE Asian Solid-State Circuits Conference (A-SSCC)**. [S.l.: s.n.], 2015. p. 1–4.

Weaver, S. et al. Domino-Logic-Based ADC for Digital Synthesis. **IEEE Transactions on Circuits and Systems II: Express Briefs**, v. 58, n. 11, p. 744–747, 2011.

Weaver, S.; Hershberg, B.; Moon, U. Digitally Synthesized Stochastic Flash ADC Using Only Standard Digital Cells. **IEEE Transactions on Circuits and Systems I: Regular Papers**, v. 61, n. 1, p. 84–91, 2014.

WOO, K.-C.; YANG, B.-D. A 0.25-V Rail-to-Rail Three-Stage OTA With an Enhanced DC Gain. **IEEE Transactions on Circuits and Systems II: Express Briefs**, v. 67, n. 7, p. 1179–1183, 2020.

WU, M. et al. Research on the architecture of Internet of Things. In: **2010 3rd International Conference on Advanced Computer Theory and Engineering(ICACTE)**. [S.l.: s.n.], 2010. v. 5, p. V5–484–V5–487.

XU, B. **Layout Automation for Analog and Mixed-Signal Integrated Circuits**. Tese (Doutorado) — University of Texas at Austin, May 2019.

Xu, B. et al. A scaling compatible, synthesis friendly VCO-based delta-sigma ADC design and synthesis methodology. In: **2017 54th ACM/EDAC/IEEE Design Automation Conference (DAC)**. [S.l.: s.n.], 2017. p. 1–6.

YAN, Y. et al. A Survey on Smart Grid Communication Infrastructures: Motivations, Requirements and Challenges. **IEEE Communications Surveys Tutorials**, v. 15, n. 1, p. 5–20, 2013.

Yasuyuki Okuma et al. 0.5-V input digital LDO with 98.7% current efficiency and 2.7-μa quiescent current in 65nm CMOS. In: **IEEE Custom Integrated Circuits Conference 2010**. [S.l.: s.n.], 2010. p. 1–4.

Yaul, F. M.; Chandrakasan, A. P. A Noise-Efficient 36 nV/ $\sqrt{}$ Hz Chopper Amplifier Using an Inverter-Based 0.2-V Supply Input Stage. **IEEE Journal of Solid-State Circuits**, v. 52, n. 11, p. 3032–3042, 2017.

YICK, J.; MUKHERJEE, B.; GHOSAL, D. Wireless sensor network survey. **Computer Networks**, v. 52, n. 12, p. 2292–2330, 2008. ISSN 1389-1286. Disponível em: <https://www.sciencedirect.com/science/article/pii/S1389128608001254>.

YOON, Y.; CHOI, D.; ROH, J. A 0.4V 63 μW 76.1 dB SNDR 20 kHz Bandwidth Delta-Sigma Modulator Using a Hybrid Switching Integrator. **IEEE Journal of Solid-State Circuits**, v. 50, n. 10, p. 2342–2352, 2015.

Yuan, F.; Parekh, P. Analysis and Design of an All-Digital $\Delta\Sigma$ TDC via Time-Mode Signal Processing. **IEEE Transactions on Circuits and Systems II: Express Briefs**, v. 67, n. 6, p. 994–998, 2020.

ZHANG, W. E. et al. The 10 Research Topics in the Internet of Things. In: **2020 IEEE 6th International Conference on Collaboration and Internet Computing (CIC)**. [S.l.: s.n.], 2020. p. 34–43.

Zhang, Y.; AL. et. A Batteryless 19 μW MICS/ISM-Band Energy Harvesting Body Sensor Node SoC for ExG Applications. **IEEE Journal of Solid-State Circuits**, v. 48, n. 1, p. 199–213, 2013.

Zou, X.; Nakatake, S. A Fully Synthesizable, $0.3\mathrm{V}$, $10\mathrm{nW}$ Rail-to-Rail Dynamic Voltage Comparator. In: **2020 IEEE 63rd International Midwest Symposium on Circuits and Systems (MWSCAS)**. [S.l.: s.n.], 2020. p. 199–202.